

Promotor: dr. ir. L. Wartena, hoogleraar in de
landbouwweerkunde en omgevingsnatuurkunde

Co-promotor: dr. ir. H. Tennekes, buitengewoon hoogleraar in de
meteorologie aan de Vrije Universiteit te Amsterdam

Flow around a line obstacle

III

CENTRALE LANDBOUWCATALOGUS

III



0000 0086 6208

NNO8201, 952

A. F. G. Jacobs

Flow around a line obstacle

Proefschrift

ter verkrijging van de graad van
doctor in de landbouwwetenschappen,
op gezag van de rector magnificus,
dr. C. C. Oosterlee,
hoogleraar in de veeteeltwetenschap,
in het openbaar te verdedigen
op woensdag 28 september 1983
des namiddags te vier uur in de aula
van de Landbouwhogeschool te Wageningen.

ISN= 192215-03

STELLINGEN

1. De impulsbalans toegepast op een controlevolume om de weerstandscoefficiënt van een obstakel op indirecte wijze te bepalen, is fysisch een correcte methode. Worden termen in deze balans verwaarloosd, dan moet zorgvuldig worden nagegaan of dit geoorloofd is. Berekeningen waarbij dit is nagelaten (b.v. Miller et al.), moeten derhalve met argwaan bekeken worden.

Miller et al., 1975: Agric. Meteor. 14, (321-333).

2. Seginer (1972) veronderstelt dat de stroming nabij het aardoppervlak rondom een obstakel altijd in lokaal evenwicht is. Deze veronderstelling is niet correct in het terugstroomgebied achter dichte obstakels.

Seginer, 1972: Bound.-Layer Meteor. 2, (87-97).

3. De weerstandscoefficiënt van een obstakel is sterk afhankelijk van de atmosferische stabiliteit. In de literatuur wordt bij buitenexperimenten de atmosferische stabiliteit vaak niet vermeld (b.v. Miller et al., 1975; Guyot, 1978). Hierdoor blijft de lezer in onzekerheid t.a.v. de reikwijdte van de conclusies.

Miller et al., 1975: Agric. Meteor. 14, (321-333).

Guyot, 1978: Bound.-Layer Meteor. 15, (57-67).

4. Voor het objectief karakteriseren van natuurlijke obstakels verdient de klassificatie in termen van weerstandscoefficiënt verre de voorkeur boven de klassificatie in termen van porositeit. Voor praktische toepassingen is deze klassificatie echter niet voldoende maar zal bovendien aangevuld moeten worden met een inventarisatie in soorten, ouderdom en toestand van de betreffende begroeiing. Bij toekomstig onderzoek aan natuurlijke obstakels zal hier aandacht aan moeten worden besteed.

5. Om de in windtunnels bepaalde weerstandscoefficienten van obstakels beter onderling te kunnen vergelijken, moet meer aandacht worden besteed aan blokkeringscorrecties.

Castro et al., 1978: J. Industr. Aerodyn. 3, (1-20).

6. Een Piche-verdampingsmeter is goed bruikbaar voor de bepaling van de potentiële verdamping indien deze binnen de aangepaste grenslaag op ca. 0,4 m hoogte boven het gewas wordt opgesteld. Metingen binnen de aangepaste grenslaag op een hoger niveau zijn ook bruikbaar mits de resultaten gecorrigeerd worden met een faktor die hoogte- en terreinruweheidsafhankelijk is.

Jacobs et al., 1983: J. Hydrol. 60, (367-380).

7. Door het nalaten van duidelijke richtlijnen vanuit het Ministerie van Justitie ten aanzien van interlandelijke adoptie, wordt wildgroei van "adoptiebemiddelaars" in de hand gewerkt.

Bia-Nieuwsbrief 1983-1.

8. De definitie van het elektrisch spanningsverschil is identiek aan die van het elektrisch potentiaalverschil. Het verschil dat Van der Laan (1979) hiertussen suggereert is misleidend. Onderscheid hiertussen maken heeft alleen zin om aan te geven of uitgegaan is van de elektrische netwerktheorie of van de elektro-magnetische veldtheorie.

Van der Laan: Inaugurele rede T.H.E., 1973-11-09.

9. Bij de T.V.-presentatie van meerdaagse temperatuurverwachtingen kunnen beter in plaats van de nu gegeven gemiddelde temperaturen voor Nederland, temperatuurverwachtingen met marges worden gegeven.
10. Het leren van een beroep of vak is in toenemende mate de verantwoordelijkheid van de hele samenleving. Derhalve dient er een Wet op het Beroepsonderwijs te komen waarin duidelijk is vastgelegd hoe de verantwoordelijkheden voor dat onderwijs maatschappelijk zijn verdeeld.

Voortgangsrapport 1983, Commissie-Wagner.

11. Het introduceren van dimensieloze getallen in leerboeken, zonder hiervan een fysische betekenis aan te geven, is didactisch onjuist.
12. De stabiliteitsklassificatie volgens Pasquill geeft enkel een schetsmatig idee omtrent de invloed van de atmosferische toestand op atmosferische processen. Deze indeling leent zich niet, en is oorspronkelijk ook niet bedoeld, voor exacte beschouwingen. Derhalve moet deze klassificatie bij exacte beschouwingen ten stelligste afgeraden worden.
13. De betekenis van het zonnetje op het veelvuldig voorkomende plakplaatje "Atoomenergie? Nee bedankt" is niet eenduidig. De bedoeling van dit plaatje is om bezorgdheid omtrent de gevaren van toepassing van kernenergie op grote schaal tot uitdrukking te brengen. Deze goede bedoeling wordt sterk ondergraven door dit plaatje te plakken op de achterraut van een auto.

A.F.G.Jacobs
Flow around a line obstacle
Wageningen, 28 september 1983

Better to do one's one duty though
void of merit than to do another's duty,
however well performed (BG, 18.47-48).

To my colleages and friends
whose collaboration has made this
work possible.

Voorwoord

Het uitvoeren van een buitenexperiment kan onmogelijk gedaan worden door één enkeling. Een hechte ondersteuning van een groep is hierbij vereist die actief meedenkt en meeleeft om meevallers mee te beleven en tegenspoed mee te helpen overwinnen. Ik mag me gelukkig prijzen in een Vakgroep te werken waarbij ik van iedereen, zonder enige uitzondering, zoveel medewerking heb gekregen. Langs deze weg wil ik graag mijn dank hiervoor uitspreken.

Promotor Bert Wartena, het enthousiasme en de doortastendheid die van jou uitstralen blijven aanstekelijk. Ik leer hier nog dagelijks van. Bovendien er-vaar ik een warme vriendschap van je.

Co-promotor Henk Tennekes, het contact tussen ons was meestal kort, bondig en to the point. De fysische gewetensvragen die je me stelde houden me nog vaak bezig. Ik hoop dat ik nog dikwijls op je kennis en inzicht mag rekenen.

Voordat een meetproject echt draait, moet er nogal wat apparatuur aangeschaft, gemaakt en getest worden. Een goed geoutilleerde mechanische en elektronische werkplaats is hierbij van onschatbare waarde.

Anton, Kees, Peter, Teun en Willy bedankt voor jullie inzet en vindingrijkheid. Tevens mag hierbij niet ontbreken de hulp in het veld die ik kreeg van Bart, Dick en Hennie en de hulp van de studenten Gerard Kempen en Ben van Moerkerk bij de ijking van diverse opstellingen.

Het voor mij onbegrijpelijke voor- en achtergrondprogramma voor de veldcomputer was samengesteld door Jon en Wim. Het resultaat was gebruikersvriendelijk maar bovendien feilloos. Hiervoor heb ik nog steeds grote bewondering.

Een stevige westenwind, zonder enige vorm van neerslag en liefst met veel bewolking waren voor ons gunstige meetomstandigheden. Deze voorwaarden waren een zeldzaamheid in de door velen als aangenaam ervaren zomer van 1982. Het hebben van een weerkamer binnen de Vakgroep is niet alleen prettig voor een zo goed mogelijke planning, maar verdiept bovendien het inzicht in het weer en wat er van weerprognoses verwacht mag worden. John en Wim bedankt voor jullie inzet.

De meest geschikte meetdagen vielen in de week-ends of op feestdagen.

Annemie bedankt om tijdens deze dagen als onbezoldigd medewerkster te assisteren en er toe bij te dragen dat de lange wachttijden zo aangenaam verliepen. De uitwerking en de interpretaties van de meetgegevens hebben me nog al eens voor vraagtekens geplaatst. Als klankbord kon ik altijd rekenen op Jacq,

Gerrit, Wim, Frits en mijn altijd even optimistische en bereidwillige kamer-
genoot Leo. Ook collega's van buiten de L.H. wil ik graag bedanken voor hun
adviezen. Met name van het K.N.M.I. Johan Wieringa en Anton Beljaars en van
de T.H.E. Hans Bessem, Cor Nieuwvelt en prof. Prasad.

Het regelen van financiële zaken is nooit mijn sterkste kant geweest. Het be-
lang hiervan wil ik niet onderschatten. Johan en Bas bedankt voor jullie be-
geleiding hierin.

Gedurende de meetcampagne waren we te gast bij de Koninklijke Luchtmacht op
de vliegbasis De Peel. De belangstelling en medewerking die we hier ondervon-
den hebben zeker mede geleid tot het succes van dit onderzoek. In het bijzon-
der moet hierbij dank uitgaan naar kapitein Verhagen en adjudant Van Renesse
van de meteodienst, majoor Ten Voorde van het meteorologisch squadron villa
Orta/De Bilt en de heren De Jong, Roelofs en Brouwer van de Babov.

Het meetterrein is opgemeten door de Vakgroep Landmeetkunde. Deze intensieve
metingen werden verricht door studentassistent V.d.Ham onder supervisie van
de heren Richardus en Masée.

Op het eind van de meetcampagne zijn van de meetopstelling foto's gemaakt.
Onder Siberisch aandoende omstandigheden is dit met vaste hand uitgevoerd
door Jo. Tevens zijn op het eind van de meetcampagne rookvisualisatie-experi-
menten uitgevoerd. Dick heeft hierbij het niet eenvoudige camerawerk verricht.
De definitieve versie van deze dissertatie is bijzonder snel en accuraat ver-
zorgd door Lenny Weldring. Het tekenwerk komt altijd op het allerlaatste mo-
ment aan bod en komt dus per definitie in tijdnood. Geen moment heb ik eraan
getwijfeld dat dit tot vertraging kon leiden omdat dit in de vertrouwde han-
den van Paul lag. Paul bedankt hiervoor alsmede voor de vele nuttige lay-out
adviezen.

De omslag is met veel geduld ontworpen door mijn broer Gerard.

Velen die direct of indirect hebben meegeholpen zijn niet persoonlijk genoemd.
Ook zij zijn hartelijk bedankt. Om dit tot uitdrukking te brengen heb ik deze
dissertatie opgedragen aan alle collega vrienden.

Wolfheze, 21 juni 1983.

List of symbols

1. Introduction and outline of the goal of this study	1
1.1 Introduction	1
1.2 Flow around a line barrier	1
1.2.1 General accepted flow picture	2
1.2.2 Description of some full-scale experiments	3
1.3 Goal of this research	6
2. Measurement project	8
2.1 Terrain conditions	8
2.2 Mean wind field	8
2.3 Fluctuations of the horizontal windspeed	10
2.4 Thermal stratification	11
2.5 Drag coefficient of the line obstacle	14
2.5.1 Direct measurement technique	14
2.5.2 Momentum integral method	16
2.6 Data processing	21
3. Results of the mean wind field	22
3.1 Results at the reference station	22
3.1.1 Reference wind profile	22
3.1.2 Upwind roughness length	24
3.1.3 Velocity and temperature deviation	25
3.2 Disturbed mean wind field	27
3.2.1 Disturbed mean wind field for perpendicular flow direction and thermally neutral stratification	27
3.2.2 Effect of thermal stratification	30
3.2.3 Oblique flow directions	35
3.2.4 Conclusions about the disturbed mean wind field	43

3.3 Turbulence properties	43
3.3.1 Near-neutral stratification	43
3.3.2 Non-neutral stratification	45
3.3.3 Conclusions about the disturbed turbulence	48
4. Results of the drag coefficient measurements	49
4.1 Introduction	49
4.2 Results obtained from direct force measurements	50
4.2.1 Dependence of the normal-force coefficient on the Reynolds number	51
4.2.2 Normal-force coefficient in oblique flow	52
4.3 Normal-force coefficients with a momentum integral method	54
4.3.1 Normal-force coefficient in oblique flow direction	58
4.3.2 Normal-force coefficient in stratified atmospheric conditions	59
4.4 Conclusions about the normal-force coefficient	61
5. Model calculations	63
5.1 Townsend's model	63
5.1.1 Description of the model	63
5.1.2 Model results	66
5.1.3 Conclusions about Townsend's model	71
5.2 Counihan, Hunt and Jackson's model	72
5.2.1 Description of the model	72
5.2.2 Model results	77
5.2.3 Conclusions about C.H.J.'s model	82
6. Conclusions and suggestions	84
Appendix A	89
Correction procedure on the speed fluctuations	
Appendix B	91
Phase shift error, caused by spatial sensor separation	

Summary	94
Samenvatting	97
References	100
Curriculum vitae	105

List of symbols

B	width of the barrier
$C_{1,2,3,4}$	constant
C_d	drag coefficient of the barrier
$C_d(x)$	contribution to the drag coefficient due to x
C_{v_1}	mean horizontal momentum coefficient $(\frac{\bar{v}_1^2}{\bar{u}_H})$
$C_{v_1 v_2}$	mean vertical transported horizontal momentum coefficient $(\frac{\bar{v}_1 \bar{v}_3}{\bar{u}_H})$
C_n	normal-force coefficient
C_p	pressure coefficient
Co	co-spectrum
c	speed of sound
c_{v_1}	horizontal turbulent momentum coefficient $(\frac{\overline{v_1'^2}}{\bar{u}_H})$
D	drag on the barrier per unit width
D'	local drag on the barrier per unit width
E	error due to spatial separation
F	force on the barrier per unit width
$F_{1,2}$	dimensionless function

F_n	perpendicular force on the barrier per unit width
${}_1F_1$	confluent hypergeometric function
f	dimensionless frequency $(\frac{n \cdot x_3}{v_1})$; dimensionless function
$f_{1,2}$	dimensionless function
G	one-sided spectrum
g	earth gravity; dimensionless function
H	height of the barrier
H^*	effective sheltered height
I	integral time scale
K_H	undisturbed exchange coefficient at height H
L	Obukhov stability length scale
l	distance behind the barrier; length scale
m	exponent
n	frequency; exponent
p	static pressure
Q	quad-spectrum
R	reduction
Ri_B	bulk Richardson number $(\frac{g}{T} \cdot \frac{\overline{\frac{dT}{dx_3}}}{2 \cdot \overline{u_H}} \cdot H^2)$

R_t	turbulent Reynolds number $(\frac{\bar{u}_H \cdot H}{2K_H})$
r	spatial sensor separation
r	correlation coefficient
T	absolute temperature
T_s	sound virtual temperature
T_v	virtual temperature
T_*	temperature scale $(\frac{\sqrt{3}T^*}{u_*})$
t	time
Δt	counter gate time
\bar{u}	mean horizontal wind speed
u	velocity perturbation ($u = \bar{u} - \bar{u}_0$)
\bar{u}_0	undisturbed mean wind speed
$u_{1,2}$	velocity scale
\bar{u}_H	mean wind speed at obstacle height
\bar{u}_∞	mean wind speed outside the boundary layer
\hat{u}	dimensionless wake strength
u_*	surface friction velocity
u_{*l}	local surface friction velocity

V_i	Fourier transform of v'_i
v_i	velocity component; $i=1$ mean wind direction; $i=3$ vertical
v_*	friction velocity perturbation ($v_* = u_{*1} - u_*$)
$\overline{v'_3 T'_v}$	vertical virtual temperature flux
$\overline{v'_i v'_i}$	turbulent flux of momentum
x_i	coordinate; $i=1$ mean wind direction; $i=3$ vertical
x_{3R}	ceiling height of the control volume
z_0	terrain roughness length

Greek symbols

α	angle
δ	delta function; boundary layer thickness
ζ	Obukkov stability parameter ($\frac{x_3}{L}$)
η	dimensionless height ($\frac{x_3}{H}$)
η_i	dimensionless coordinate ($\frac{x_i}{H}$)
κ	von Karman constant (0,41)
λ	wave length
ν	kinematic viscosity
ρ	air density; correlation function

σ	standard deviation
τ	time; perturbation of the shear stress
τ_w	surface shear stress
τ	undisturbed shear stress
ϕ	angle of attack
ϕ_M	dimensionless wind shear function
ψ	dimensionless wind function

subscripts and superscripts

a	ahead
b	behind
H	reference height (2m)
m	maximum; measured
min	minimum
t	translated
o	value in perpendicular flow direction; undisturbed
R	reference

In this thesis units and other conventions are used according to ISO/31/0.

1 Introduction and outline of the goal of this study

1.1 INTRODUCTION

A class of flows which often occurs in nature and in engineering practice, is the class of strongly perturbed shear layer flows. Examples can be given easily. In rural areas e.g., man has applied shelterbelts to protect himself, his livestock and his acreage against the effects of high winds. This is done especially in the plains regions, with the aim to protect the soil from erosion by winds. Well known are the extensive shelterbelt programs carried out in the U.S.S.R. and U.S.A. in 1931 and 1934, respectively. If a shelterbelt is erected, the wind field near the surface is not the only element that is affected: almost all other meteorological quantities will be influenced too. In textbooks (J. Grace, 1977) and papers (S. Shaw, 1962; D. Benndorf et al., 1980) a qualitative survey can be found of the advantages and disadvantages of shelterbelts for agricultural use.

In urban regions the importance of the knowledge of the atmospheric flow around man-made obstructions has also attained increasing recognition. Such flows e.g. have a major effect on turbulent diffusion from pollutants in their vicinity (Ogawa et al., 1980). In construction design, there is an increasing tendency towards greater economy in applying materials. Consequently, loads and oscillation effects on buildings and structures require a better understanding of strongly perturbed flows (Frost et al., 1977). Commercial air transportation between metropolitan areas has caused an increasing need of vertical and very short takeoff and landing services (V./S.T.O.L.). Buildings induce zones of recirculation and regions of large fluctuations which can make V./S.T.O.L. extremely hazardous (Burnham, 1967).

Despite several full-scale and wind tunnel studies, as yet little is known and understood about the class of strongly perturbed shear flows. The cause behind this is partly that these flows are surprisingly complicated (Bradshaw & Wong, 1972) and partly a lack of experimental data (Counihan et al., 1974).

The general objective of the present study is to contribute to a better understanding of this class of flows. To attain this objective, a full-scale experiment was carried out around a two-dimensional barrier attached to the earth

surface. Despite an uncontrollable atmospheric flow and high costs, an outdoor experiment was done because especially in nature this class of flows very often occurs, but it has been investigated much less thoroughly than e.g. reduced model flows in a wind tunnel. Moreover, in simulating atmospheric phenomena there still exist serious problems with scaling correctly (Raine et al. 1977 and Ogawa et al., 1980), consequently these results for outdoor applications remain of limited importance.

1.2 FLOW AROUND A LINE BARRIER

1.2.1 General accepted flow picture

To provide a better understanding of the fluid mechanics of a strongly perturbed shear layer flow, a qualitative description will be discussed in connection with a flow around a two-dimensional barrier. This description is based on the field measurements of Nägeli (1953) and Woodruff et al., (1955) and on the data of the theoretical work by Kaiser (1959). In figure 1.1, a mean streamline picture is given for permeable barriers with a porosity of 15 to 25% and 45 to 55%. Here the porosity is defined as the ratio between the open and the total area of the barrier. As can be seen from this picture, the streamlines are displaced just around the barrier. Ahead of the barrier the flow rises; it descends after having passed the barrier. Consequently, at the surface around the obstacle, the wind speed will be considerably smaller. According to the conservation of mass this means that at greater heights above the barrier the wind speed must increase. Up to a height of 3 to 4 times the barrier height, the wind field will be influenced significantly. The flow field around the obstacle is not symmetric but the ascent at the windward side is steeper than the descent at the leeward side. Therefore, the protected region at the leeward side is much larger than that at the windward side. A peak in the wind speed appears just over the barrier at the leeward side, with a very calm region beneath it near the surface. If the two barriers are compared, it can be concluded that the displacement of the streamlines is greater if the barrier is less permeable, but the vertical wind gradient is also steeper. A distorted wind field starts to recover downwardly and the distorted flow with the greatest displacement and vertical wind gradient, shows the fastest recovery. One generally takes the view that horizontally the influenced region extends from 3 to 5 times the barrier height at the

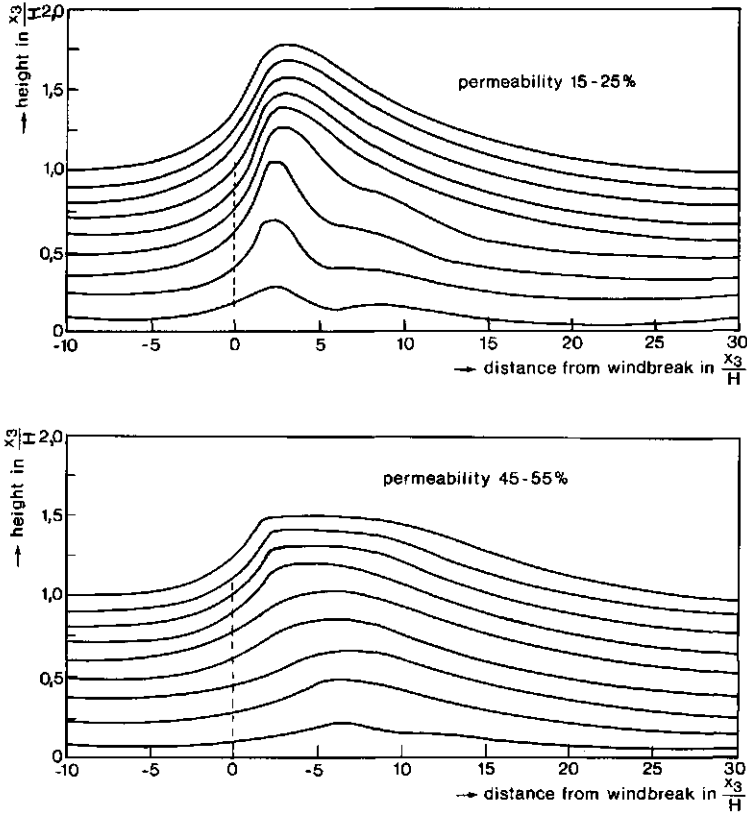


Fig. 1.1 The streamlines around a porous obstacle after Kaiser (1959).

windward side and up to 20 to 30 times at the leeward side.

1.2.2 Description of some full-scale experiments

In studying perturbed shear layer flows, several outdoor experiments and wind tunnel experiments were carried out. A brief review of the most important field studies will be given. As we intend to study an outdoor disturbed flow, this outline will be restricted to full-scale field experiments.

In 1941, Nægeli started his pioneering work with a number of experiments on natural and artificial windbreaks. In his experiment he used two masts. He measured with cup anemometers at nine levels. One mast, the one at the windward side, was invariably used as a reference, while the other was placed at

several locations around the barrier. His results are presented in averaged percentages of the undisturbed wind profile. He mainly studied winds perpendicular to the obstacle and did not determine the thermal stratification of the atmosphere. His obstacles were characterized by their height, width, thickness and optical porosity. For artificial obstacles this porosity was defined as the ratio between the open surface and total surface. The natural obstacles were described by the species of shrubs and trees the windbreak consisted of. Besides, a characterization was given in terms of very dense, dense, medium and loose. An oft-cited result of his study is given in figure 1.2. In this figure the mean disturbed wind speeds are depicted, expressed in percentages of the undisturbed wind for several kinds of natural obstacles at a height of 0,25 times the obstacle height H . All of these obstacles had different heights and to get a better comparison, he also made the distances dimensionless with the barrier height. Several properties discussed in the foregoing section, can be recognized from this figure.

In 1961, Halitsky carried out an experiment on a natural shelterbelt consisting of rows of high trees with no shrubs in between. At one leeward location only, he measured a wind profile and wind direction; at three locations further leeward, the wind speed and direction at only one height. For all measured quantities the mean value as well as the standard deviation were esti-

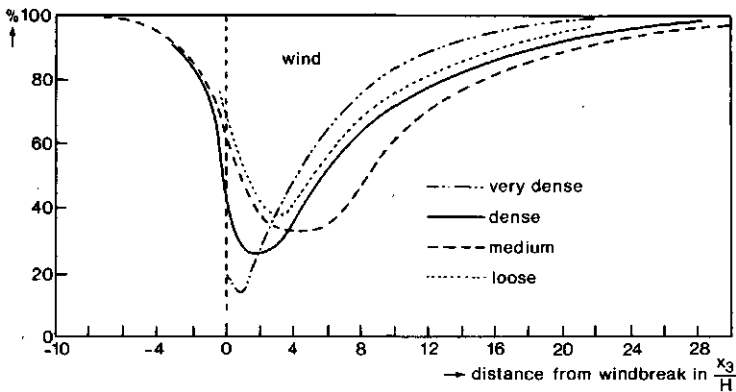


Fig. 1.2 The distorted flow at $\frac{x_3}{H} = 0,25$ in percentages of the undisturbed wind speed after Nægeli (1953).

mated. A major shortcoming of this experiment is that no data were taken on the undisturbed wind profile, wind direction and thermal stratification.

In 1971, Hagen and Skidmore performed an experiment similar to that of Nægeli, with two masts and artificial barriers with different porosity. Both masts were easily transportable and equipped with cup anemometers and thermocouples. In addition, at one-half of the obstacle height they measured the r.m.s. values of the three turbulent velocity components with two anemometer bivanes. It was the first experiment in which the atmospheric stratification was measured by estimating the bulk Richardson number.

In 1971, Seginer performed an experiment with an artificial obstacle. At the undisturbed windward reference location the wind profile and the wind direction at obstacle height were measured. Besides, at two levels at this location, the mean temperature was measured to estimate the atmospheric stratification. At several locations around the barrier, but only at one level close to the surface, the wind speed was measured. The behavior of the distorted wind field was studied for perpendicular and oblique winds. The special feature of this experiment was that Seginer did not only characterize his obstacle with porosity, but he also measured the drag coefficient directly. More or less in the center of the obstacle, Seginer replaced a section of the barrier by a measuring plate. With strain gauges he estimated the normal-force on this plate, exerted by the wind field. The drag coefficient of the barrier is this normal-force nondimensionalized with the surface of the measuring plate and an appropriate pressure. Seginer used the undisturbed dynamic pressure at obstacle height. Especially, this parameter appears to be of major importance for the behavior of a strongly disturbed flow. This can easily be understood from the aerodynamic action of a barrier in a flow field. The fluid flow exerts a drag on the barrier which is compensated by a momentum loss of the flow itself. Consequently, the flow will be reduced and the greater this drag, the greater the flow reduction will be.

Summarizing all available field experiments showed up several shortcomings. Up to now simultaneous outdoor measurements of a complete distorted wind field have not been made. The existing data are either obtained at different times (e.g. Nægeli and Hagen et al.) or very limited (e.g. Halitski and Seginer). The results of Nægeli and Hagen et al., were obtained by using only

two masts. This introduces an uncertainty about the effect of the thermal stratification and undisturbed wind direction into their measurement results. The data of Halitsky cannot be compared with other results, for nothing is known about the undisturbed reference condition. Seginer did measure the complete undisturbed wind profile and the atmospheric stratification at the reference location, but the speeds of the distorted wind field were only measured at one level close to the surface.

1.3 GOAL OF THIS RESEARCH

Experimental work on the flow around obstacles is widely dispersed in the literature over various disciplines. Field research is mostly done for very practical purposes, e.g. increasing crop yields, stabilizing of the soil, etc. However, this widespread of applications had a very important disadvantage (Baltax 1967) in that this research up to now did not follow a systematic approach so that the available results remain of limited value.

In the foregoing one goal of our study showed up already. We wanted to measure simultaneously a distorted wind field under various thermal stratifications. To achieve this, we measured the mean wind profiles around a barrier and the atmospheric stratification at an undisturbed reference location. In the distorted flow, not only the mean wind speeds will be influenced but the turbulence as well. To gain insight into the behavior of the disturbed velocity fluctuations, we also measured the r.m.s. values for all wind speeds.

Various researchers have tried to develop a theoretical treatment of the flow around a two-dimensional barrier. The models known best are those of Kaiser (1959) for the near wake region and of Townsend (1965) for the far wake region. Both models and a model developed more recently for the far wake region (Counihan et al., 1974) will be discussed in more detail in Ch 5 and checked with our data.

In this study, special attention will be given to the aerodynamic characterization of the barrier. Usually, an artificial barrier is characterized by its porosity. As we have already seen, it is a more attractive way, physically, to express the effect of a barrier in terms of its resistance to the fluid flow, or, in a dimensionless form, in terms of a drag coefficient. In addi-

tion, as will be pointed out in Ch 5, this coefficient will be an important parameter in the verification of the model approaches of Kaiser and Townsend. If there existed a unique relation between porosity and drag coefficient, both characterizations would be of equal value. The characterization in terms of porosity in practice is favourable because of its simplicity. However, there exists no unique relation between both characterizations. The drag on a barrier not only depends on the porosity but also on the shape and the arrangements of the openings. For natural barriers there is an additional difficulty if the porosity characterization is used. Optically a natural barrier can be dense but for the fluid flow it is permeable. That is why for natural windbreaks the porosity is mostly defined as the ratio between the open volume and total volume of the barrier. Also this porosity is not uniquely related to the drag coefficient. E.g. trees with or without foliage do not differ much as to porosity but they do as to their resistance to the flow. In this study an artificial barrier was used, characterized by its drag coefficient. In this barrier a measuring plate was mounted in a way comparable to Seginer's (1971). At this plate the drag was measured with force sensors.

It is hardly possible to simulate a section of a natural barrier in such a way that the drag on this section can be measured directly. In this study we will investigate a method to estimate the drag on natural barriers by using the momentum conservation for a control volume just around the barrier. As will be pointed out in Ch 2, to apply this method, we have to know the static pressure at the front and rear borders of this control volume. That is why in this study too the focus of our attention will be on measuring the static pressure profiles just around the barrier.

2 Measurement project

2.1 TERRAIN CONDITIONS

In order to carry out an extensive measurement program, a suitable terrain was found in the south east of the Netherlands. This terrain bordered an aircraft runway and is located at about $51^{\circ}33'N$ and $5^{\circ}56'E$. In figure 2.1 a survey of the measuring site is given in which moreover the mean surface isohypses are depicted. The isohypses are given as relative to the location "mast 1", which by definition is the 5,0 m point.

As a barrier, a thin solid plate was used with a height of 2 m, a width of 60 m and a thickness of 0,02 m. The barrier was orientated in the exact NS direction.

The observations were carried out in westerly wind conditions. As can be seen from figure 2.1, the near windward terrain consisted of heather and the far windward terrain of grass. The heather has been mowed and during the measurement campaign it nearly had the same aerodynamic roughness as the grass. The vegetation height was about 0,25 m and the surface roughness length, z_0 , of the windward terrain had a mean value of 35 mm (see CH 3) for all westerly wind directions.

2.2. MEAN WIND FIELD

The mean wind profiles around the barrier were measured at 9 stations, located from the barrier at distances: $-10H$, $-3H$, $-H$, H , $3H$, $5H$, $10H$, $15H$, and $30H$. Here H stands for obstacle height, negative ahead and positive behind the obstacle. Just around the barrier the largest disturbances take place and here the most stations were concentrated. The most windward station at $-10H$ was used as the undisturbed reference location. At all stations, except at $-H$ and H , the wind speed was measured at seven levels: $\frac{H}{3}$, $\frac{H}{2}$, H , $2H$, $3H$, $4H$ and $5H$. For reasons of economy at $-H$ and H , the wind speeds were measured at four levels: $\frac{H}{3}$, $\frac{3}{4}H$, $\frac{5}{4}H$ and $2H$.



Fig. 3.1 A survey of the measuring site in which the relative surface isohypses have been plotted. Mast 1 is the 5 m point by definition.

The wind speeds were measured by means of small cup anemometers, designed at the laboratory of Physics and Meteorology. The mean starting speed was $0,20 \text{ m.s}^{-1}$ and the first-order response length $0,9 \text{ m}$.

The cup rotation speed was measured with a photo-chopper system. To avoid pulse distortion due to the long transmitting lines, we applied current pulses of 20 mA .

The cup anemometers were mounted on rectangular booms, fitted to a triangular mast with sides of $0,18 \text{ m}$. The booms had a length of 1 m so as to avoid mast interferences (Smedman et al., 1973).

2.3 FLUCTUATIONS OF THE HORIZONTAL WIND SPEED

In order to gain insight into the turbulence of the disturbed flow field, the r.m.s. values of the measured speeds were estimated. These r.m.s. values, as measured by the cup anemometers, suffered from errors due to the first-order response length of $0,9 \text{ m}$ and due to the counter gate time of the pulse counting system.

We aimed at measuring all speeds, within the range $(1-15) \text{ m.s}^{-1}$, with an accuracy of at least 3% . This means that for the applied pulse counting system, the counter gate time is 10s . Dependent on the mean wind speed, this time corresponds to a response length of $(10-150)\text{m}$. Consequently, the instrumental high-frequency cut-off was determined by the counter gate time.

In order to measure the r.m.s. value of the speed correctly, the spectral distribution must lie within the spectral band width of the measuring system. From analysis of McBean (1972) we may conclude that for an undisturbed flow, the maximum cut-off frequency of the cup anemometer system in dimensionless form,

$$f = \frac{n \times x_3}{u} \quad (n \text{ is frequency and } x_3 \text{ is height}), \text{ must be at least } 5. \text{ Which means}$$

that, especially near the surface, a great deal of the contributions made by the higher frequencies will be discarded. The measured r.m.s. values, dependent on the mean wind speed and measuring height, will be seriously underes-

timated.

If from the horizontal speed fluctuation, u' , the auto-correlation function $\rho_u(\tau)$ is known, the underestimated r.m.s. values of the speed can be corrected. This correction procedure is pointed out in Appendix A and from this it appears that the real speed variance, $\overline{u'^2}$, is related to the measured speed variance, $\overline{u_m'^2}$, according to:

$$\overline{u'^2} = \frac{\overline{u_m'^2}}{\frac{2}{\Delta t} \int_0^{\Delta t} (1 - \frac{\tau}{\Delta t}) \rho_u(\tau) d\tau} \quad (2.1)$$

where Δt is the counter gate time.

For an undisturbed flow, the auto-correlation function is easy to be deduced from spectra data (Bessem, 1976; Tennekes, 1979; see Appendix A). For outdoor disturbed shear flows, only a few incidental normal stress spectra are known (Gandemer, 1981; Ogawa, 1980). These spectra are only measured at one-half of the obstacle height. The general feature of these spectra is that the shape more or less equals the undisturbed spectrum but that the peak has a slight shift to a higher frequency. At a distance of about $5H$ the maximum shift appears, with a peak frequency of about two times the undisturbed frequency. Further down stream, the peak gradually recovers to the original peak frequency. In addition, wind tunnel studies show a similar picture for heights from $\frac{H}{4}$ to H (Raine, 1977).

All measured r.m.s. speed values up to the obstacle height were corrected according to equation (2.1) and with the auto-correlation functions obtained from the disturbed spectra data. Beyond the obstacle height, no auto-correlation functions are known. That is why these r.m.s. data have not been worked out any further.

2.4 THERMAL STRATIFICATION

In a thermally stratified shear flow, the turbulence characteristics at a height x_3 will depend only on the five quantities:

x_3 , ρ , $\frac{g}{T}$, u_* and $\overline{v_3' T_V'}$ (Monin and Yaglom, 1973). Here ρ stands for the air

density, g for the earth gravity, \overline{T} for the absolute temperature, u_* for the friction velocity defined as $u_* = \sqrt{\frac{\tau_w}{\rho}}$ in which $\tau_w = -\rho \overline{v_1' v_3'}$ is the surface shear stress and $\overline{v_3' T_V'}$ for the mean vertical virtual temperature flux i.e. the temperature flux in which the moisture effect is included. The mean values are denoted by overbars and the fluctuating values by primes. Since there are four independent dimensions (length, time, mass and temperature), only one dimensionless parameter can be combined from these quantities. Following the original analysis of Obukhov (1946), the dimensionless combination

$$\zeta = \frac{x_3}{L}, \quad (2.2)$$

will be chosen where L , called the Obukhov length, is defined as

$$L = \frac{-u_*^3}{\kappa \frac{g}{T} \overline{v_3' T_V'}} \quad (2.3)$$

Here κ stands for the von Karman constant, which is traditionally included in this length scale.

In order to estimate this parameter of the undisturbed flow, u_* , $\overline{v_3' T_V'}$ and \overline{T} were measured at the reference station. A three-dimensional sonic anemometer/thermometer from Kayo Denki type DAT 310 with sensor type TR-61C was used. To avoid tilt errors (Raymont et al., 1971), we provided the sensor with a leveling device with an accuracy of $0,5^\circ$.

The temperature output of the sonic thermometer, called the sound virtual temperature T_S' , differs from the real virtual temperature T_V' according to (Kaimal et al., 1963):

$$T_S' = T_V' - \frac{2\overline{T}}{c^2} v_1', \quad (2.4)$$

where c stands for the sound speed. As by the sonic anemometer v_1' was estimated also, T_S' was corrected according to equation (2.4).

The turbulence fluxes as measured, suffer from errors due to line averaging caused by the sound paths and due to a phase shift caused by spatial separation of the sensors (see figure 2.2). The line averaging error will be eliminated if the minimum measuring height is at least $x_{3min} = 5\lambda$, with λ the

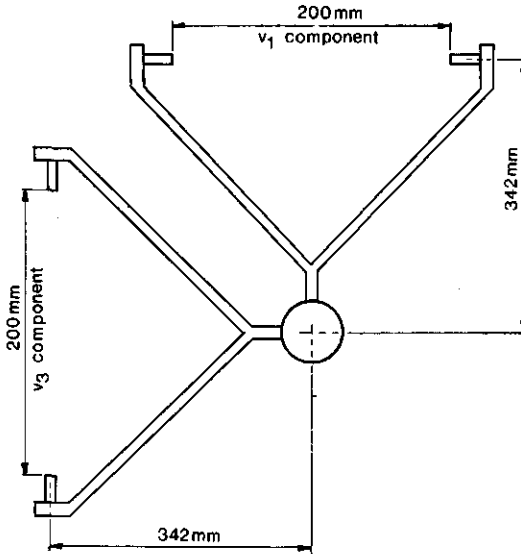


Fig. 2.2 The design of the wind sensor type TR-61C of the sonic anemometer.

smallest wave length reliably measured by the sensor. As the sound paths were about 0,20 m, this means that $x_{3min} > 1$ m. The phase shift error can only occur in a cross-correlation, in which two different sensors do not coincide, which was the case in measuring the momentum flux $-\overline{v_1 v_3}$. Here the two velocity sensors had a spatial separation of about 0,35 m. As pointed out in Appendix B, this error also depends on the measuring level and decreases with increasing height. If a maximum error of 4% in the measured momentum flux is accepted this means that this height must be at least 6 m. During the campaign this level was chosen as observation height.

2.5 DRAG COEFFICIENT OF THE LINE OBSTACLE

If a body is placed in a flow field, a force called the drag, will be exerted on this body by the fluid flow. This force is commonly expressed in terms of a dimensionless coefficient, obtained by dividing this drag by the dynamic pressure and the area of the body projected on a plane perpendicular to the flow direction. If a two-dimensional line obstacle is attached to the surface and is immersed in its boundary layer, this coefficient is mostly defined as (Plate, 1971):

$$C_d = \frac{D}{\frac{1}{2} \rho \bar{u}_H^2 H}, \quad (2.5)$$

where D is the drag per unit width of the obstacle and \bar{u}_H the undisturbed wind speed at the obstacle height.

2.5.1 Direct measurement technique

More or less in the center of the barrier, a section of height H and a width of 0,9 m was removed and replaced by a drag measurement plate. This measurement plate was mounted in a stiff frame and was fixed with three bars (figure 2.3). From one bar the plate was hanging in order to carry the plate's weight. We fixed the two horizontal bars in order to prevent horizontal movements in the plane of the barrier. The bars were necked near the fastenings to permit slight "free" movements in the perpendicular direction of the plate.

Between the frame and the measurement plate, three force sensors were fixed, two near the top and one near the bottom. The force sensors were arranged in such a way that a wind load was equally spread among the sensors.

The forces were estimated with force sensors from Brosa, type EBM-6200-5. The loading capacity per sensor ranged from -50N to 50N, with a maximum displacement of 20 μ m. The displacement is very small, so that load errors caused by the weight of the measurement plate could be ignored.

In the laboratory, the whole set-up was checked and calibrated for perpendicular as well as for oblique loadings (Kempen, 1982).

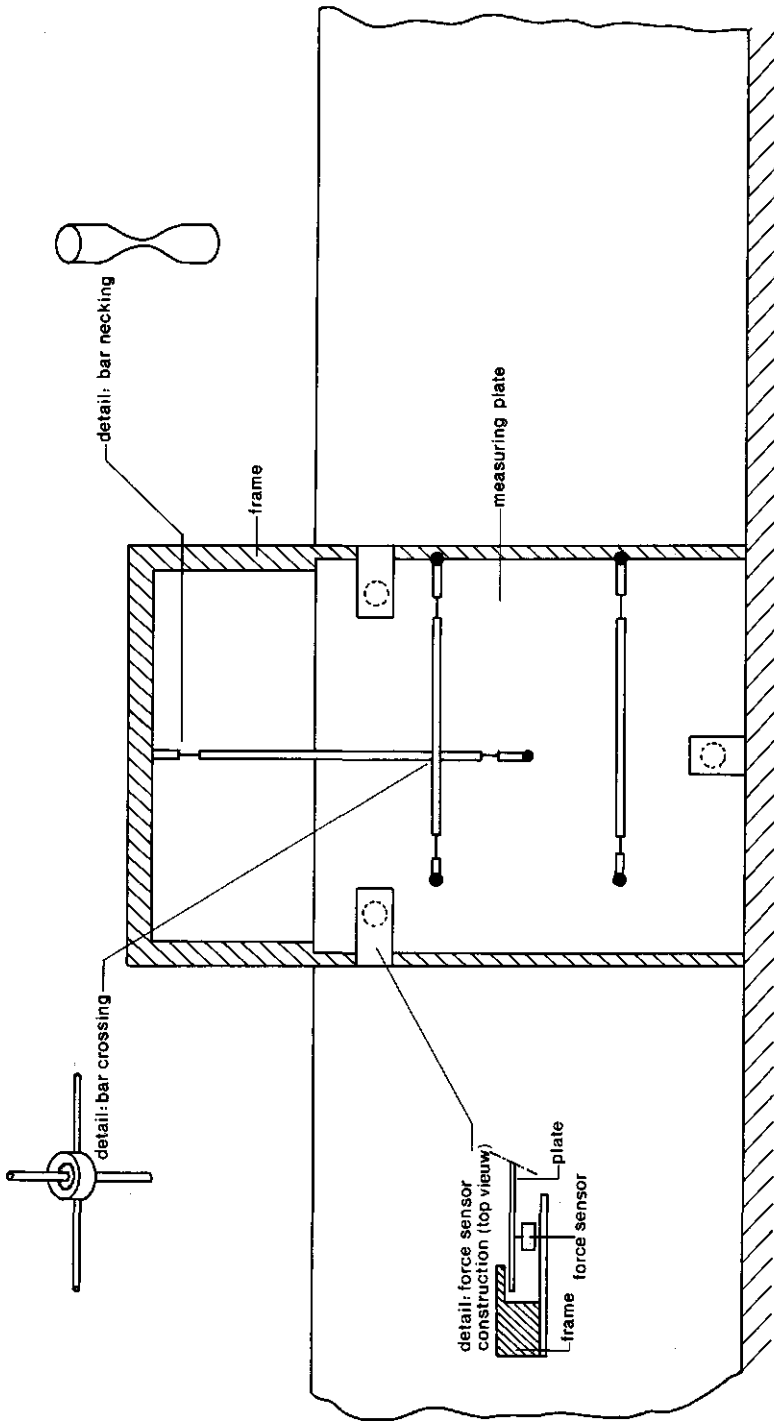


Fig. 2.3 Measurement plate construction (back view)

2.5.2 Momentum integral method

If the mean horizontal momentum equation is integrated in a control volume in which the barrier is included, the drag on the barrier can be estimated as a remaining term. Starting from a flow direction perpendicular to the barrier, the two-dimensional horizontal momentum equation for a turbulent flow, in which a momentum sink is included, is (Tennekes and Lumley, 1972):

$$\rho(\bar{v}_1 \frac{\partial \bar{v}_1}{\partial x_1} + \bar{v}_3 \frac{\partial \bar{v}_1}{\partial x_3} + \frac{\partial}{\partial x_1} \overline{v_1'v_1'} + \frac{\partial}{\partial x_3} \overline{v_1'v_3'}) + \frac{\partial \bar{p}}{\partial x_1} = -\delta(x_1)F(x_3) \quad (2.6)$$

Here p stands for the pressure, $\delta(x_1)$ for the delta function and $F(x_3)$ for the vertical momentum sink distribution at the obstacle per unit width. Integration of this equation in a control volume with the boundaries as depicted in figure 2.4, results in:

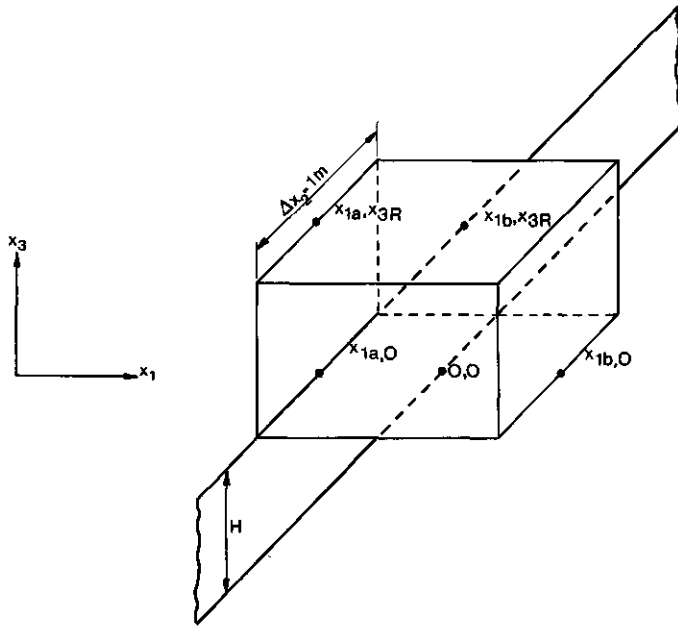


Fig. 2.4 The coordinates of the control volume in (x_1, x_3) .

$$\int_{z_0}^{x_{3R}} dx_3 \{ \rho (\overline{v_1^2}(x_{1a}, x_3) - \overline{v_1^2}(x_{1b}, x_3)) + \rho (\overline{v_1'^2}(x_{1a}, x_3) - \overline{v_1'^2}(x_{1b}, x_3)) + (\overline{p}(x_{1a}, x_3) - \overline{p}(x_{1b}, x_3)) \} - \quad (2.7)$$

$$\int_{x_{1a}}^{x_{1b}} dx_1 \{ \rho \overline{v_1}(x_1, x_{3R}) \overline{v_3}(x_1, x_{3R}) + \rho (\overline{v_1'v_3'}(x_1, x_{3R}) - \overline{v_1'v_3'}(x_1, x_{3R})) \} = D,$$

where D is the perpendicular drag on the barrier per unit width.

In our study a very small and narrow control volume was chosen for which this result can be simplified. It may be expected that the contribution to the drag of the turbulent stress term is small, according to the small horizontal integration interval. In doing so, (2.7) will reduce to:

$$\int_{z_0}^{x_{3R}} dx_3 \{ \rho (\overline{v_1^2}(x_{1a}, x_3) - \overline{v_1^2}(x_{1b}, x_3)) + \rho (\overline{v_1'^2}(x_{1a}, x_3) - \overline{v_1'^2}(x_{1b}, x_3)) + (\overline{p}(x_{1a}, x_3) - \overline{p}(x_{1b}, x_3)) \} - \quad (2.8)$$

$$\int_{x_{1a}}^{x_{1b}} dx_1 \{ \rho \overline{v_1}(x_1, x_{3R}) \cdot \overline{v_3}(x_1, x_{3R}) \} = D,$$

or, in dimensionless form with $C_{v_1} = \frac{\overline{v_1^2}}{u_H^2}$, $c_{v_1'} = \frac{\overline{v_1'^2}}{u_H^2}$,

$$C_p = \frac{\overline{p}}{\frac{1}{2} \rho u_H^2}, C_{v_1 v_3} = \frac{\overline{v_1 v_3}}{u_H^2} \text{ and } \eta_i = \frac{x_i}{H} :$$

$$\int_{\eta_0}^{\eta_{3R}} d\eta_3 \{ 2(C_{v_1}(\eta_{1a}, \eta_3) - C_{v_1}(\eta_{1b}, \eta_3)) + 2(c_{v_1'}(\eta_{1a}, \eta_3) - c_{v_1'}(\eta_{1b}, \eta_3)) + (C_p(\eta_{1a}, \eta_3) - C_p(\eta_{1b}, \eta_3)) \} - \quad (2.9)$$

$$\int_{\eta_{1a}}^{\eta_{1b}} d\eta_1 \cdot 2C_{v_1 v_3}(\eta_1, \eta_{3R}) = C_d.$$

Or, in the very simplified form:

$$C_d(\bar{V}_1) + C_d(\sigma_v) + C_d(\bar{p}) + C_d(\bar{V}_3) = C_d, \quad (2.10)$$

where, in the chosen control volume, $C_d(\bar{V}_1)$ is the contribution to the drag coefficient due to the horizontal flux change etc. If equation (2.9) is accepted, it will mean that just around the obstacle the horizontal wind velocity and its variance and the mean pressure profiles have to be measured in order to calculate the drag. The vertical flux of horizontal momentum can be estimated by using the mean two-dimensional continuity equation:

$$\bar{v}_3 = - \int_{z_0}^{x_3} \frac{\partial \bar{v}_1}{\partial x_1} dx_3. \quad (2.11)$$

During the measurement campaign, the mean pressure profiles were estimated at the locations $-H$ and H and were relatively measured with regard to the undisturbed pressure at the reference station. At five levels at each location the mean pressure was determined at $x_3 = 0, \frac{H}{3}, \frac{3}{4}H, H$ and $\frac{5}{4}H$. Most measuring levels were chosen near the top of the barrier, because here the major changes in the pressure profiles may be expected.

The pressure profiles were measured with sensors as described in the literature by Elliott (1972). Such a sensor consists of a thin circular disc with a diameter of 40 mm, mean thickness of 2 mm and with ports in the center of the disc which lead to a micro barometer (figure 2.5). In order to minimize the dynamic pressure noise, generated by the interference between the flow field and the sensor body, this disc must be accurately streamlined. The sensors were checked and calibrated in a wind tunnel (Jacobs, 1983^a).

To convert the pressure into a corresponding electrical signal, a differential micro barometer was used from Datametrix type 590D with an operation range of $-10 \text{ mmH}_2\text{O}$ to $10 \text{ mmH}_2\text{O}$ and an accuracy of 0,05 % of the reading. One side of the barometer was permanently connected to the reference sensor.

During the campaign only one barometer was available. The pressure sensors around the barrier were scanned by a pneumatic multiplexer. The multiplexer as used was from Scanivalve, type W0601/1P-12T, which scanned every sensor with a sampling interval of 12 s (figure 2.6). Between the sensors and the

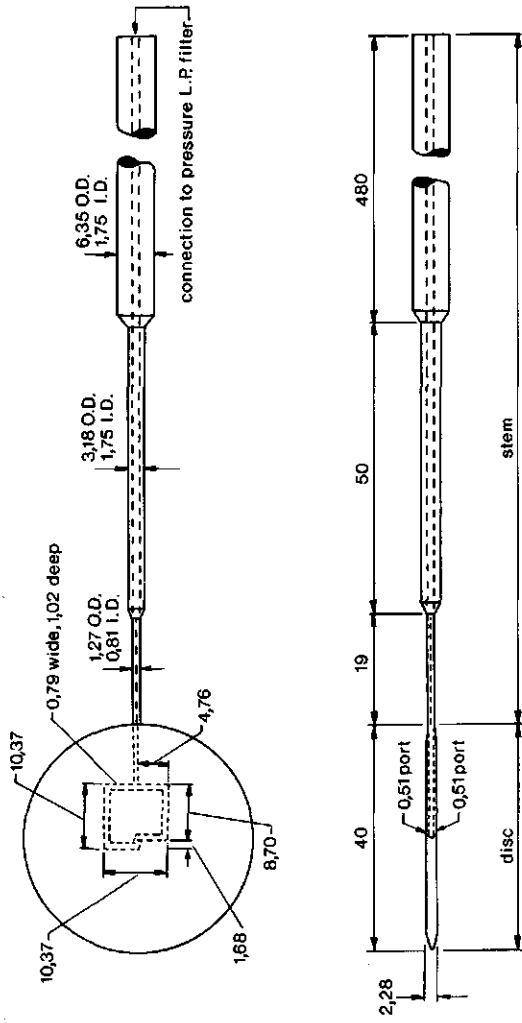


Fig. 2.5 Probe developed to sample the fluctuations in the static pressure.
Dimensions are in mm.

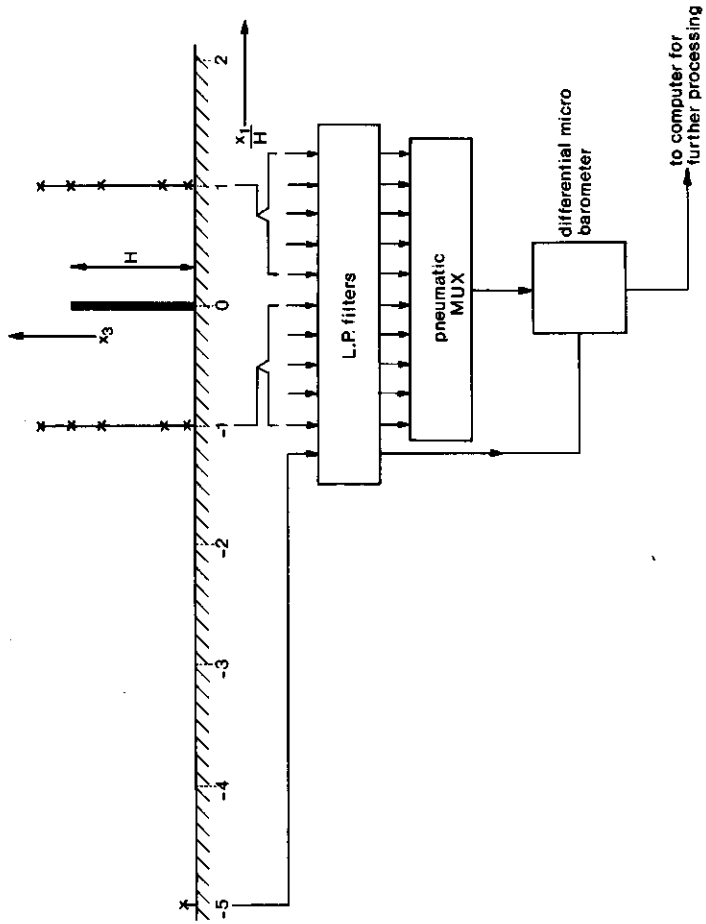


Fig. 2.6 Block diagram of the static pressure data processing. x is pressure sensor.

multiplexer a pneumatic low pass filter was placed with a first-order time constant of 70 s. The whole set-up was tested in the laboratory (Jacobs, 1983^b).

2.6 DATA PROCESSING

All the measured signals were transported to a van at a distance of 300 m downwind from the barrier, in which a mini-computer (PDP-11/03) was installed. Here the pulses from the cup anemometers were counted and the continuous signals were digitized. On-line the data were reduced to 30 min. averages and the results were stored on cassette tape (TU-58).

At the laboratory further processing was carried out with another mini-computer (PDP-11/34) or with a big DEC computer (DECSYS-10), depending on the kind of analysis.

3 Results of the mean wind field

During the measurement campaign about 300 runs of 30 minutes each were collected, from which 120 runs were selected for further analysis. Runs with precipitation were discarded because of instrumental uncertainties and runs in very unstable weather ($\frac{H}{L} < -0,4$) were discarded because the wind direction could not be determined accurately at the low wind speeds in these conditions.

Before analyzing the disturbed wind field, the measured profiles and turbulence data at the reference station were analyzed. Special attention was paid to these results, for all other results were to be compared with these data. Moreover, the data at this station were used to determine the roughness condition of the windward terrain.

3.1 RESULTS AT THE REFERENCE STATION

3.1.1 Reference wind profile

On the basis of dimensional analysis, Obukhov (1946, 1971) showed that in stationary conditions, the vertical flux of momentum over a horizontal, homogeneous surface is related to the wind speed profile by:

$$\frac{d\bar{u}}{dx_3} = \frac{u_*}{\kappa \cdot x_3} \cdot \phi_M\left(\frac{x_3}{L}\right). \quad (3.1)$$

Here ϕ_M is the nondimensional wind shear, which is a universal function of the stability parameter $\frac{x_3}{L}$. The shape of the function ϕ_M can be determined experimentally. Interpolation formulas have been given by Monin & Yaglom (1971), Businger et al. (1971), Dyer (1974) and many others. In this study the results of Wieringa (1980) have been adopted. These are based on the revised 1968 Kansas data. Wieringa uses:

$$\phi_M = \left(1 - 22\frac{x_3}{L}\right)^{-\frac{1}{4}} \quad \text{for } \frac{x_3}{L} < 0 \text{ (unstable case),} \quad (3.2)$$

and $\phi_M = \left(1 + 6,9\frac{x_3}{L}\right) > 0$ (stable case).

After integrating (3.1), the following explicit expression is obtained for the undisturbed profile:

$$\bar{u} = \frac{u_*}{\kappa} \left(\ln \frac{x_3}{z_0} - \psi \right) \text{ for } \frac{x_3}{L} < 0,$$

with $\psi = 2 \ln\{(1+x)/2\} + \ln\{(1+x^2)/2\} - 2 \tan^{-1}x + \frac{\pi}{2}$,

$$x = \phi_M^{-1} \tag{3.3}$$

$$\text{and } \bar{u} = \frac{u_*}{\kappa} \left(\ln \frac{x_3}{z_0} + 6,9 \frac{x_3}{L} \right) \text{ for } \frac{x_3}{L} > 0.$$

For all runs, this profile was fitted with a least-squares method (Robinson, 1962, and Covey, 1963). This curve-fit was used to determine the friction velocity, u_{*p} , (the subscript p refers to the profile method) and the roughness length, z_0 , of the windward terrain. The friction velocity, u_{*p} , was compared with the friction velocity, u_{*s} , measured with the sonic anemometer. The comparison is shown in figure 3.1. A linear regression without zero bias

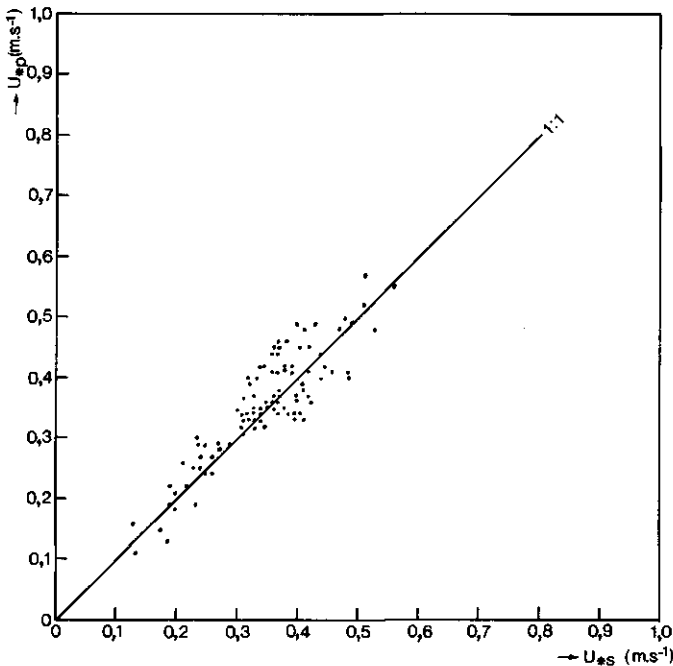


Fig.3.1 The friction velocity u_{*p} , determined by means of the speed profile, compared with the friction velocity u_{*s} , measured by the sonic anemom.

yields:

$$u_{*p} = 1,025 u_{*s},$$

with a standard deviation of 0,045 and a correlation coefficient of 0,98. From this result we conclude that they agree well.

3.1.2 Upwind roughness length

To analyze the terrain ahead of the obstacle, the windward terrain was divided into sectors of 10 degrees. For every sector the mean z_0 value and its standard deviation for the entire measurement campaign were calculated. The results are plotted in figure 3.2. This figure shows a more or less constant

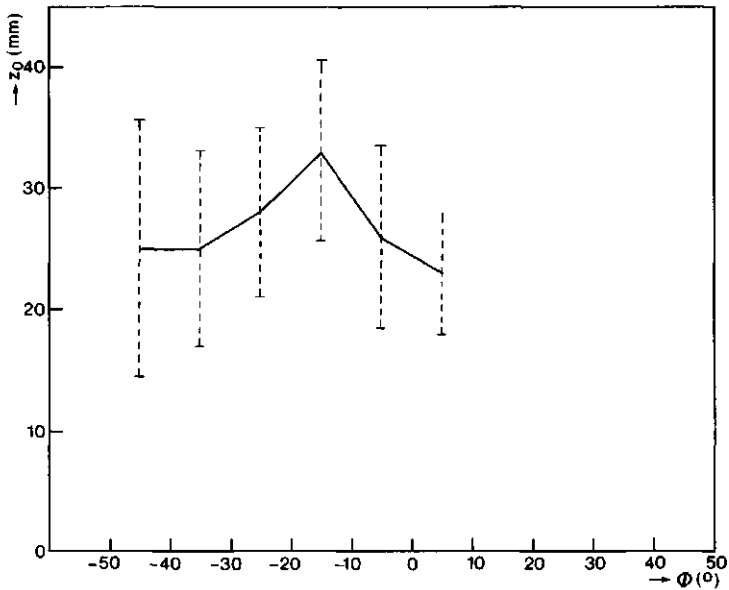


Fig. 3.2 The roughness length z_0 and its standard deviation as a function of the incidence angle ϕ . Values pertain to the whole measurement campaign.

roughness length for all sectors, but a rather large standard deviation. The main reason for this is that the terrain roughness elements consist of natu-

ral material that changes particularly during the growing season. In figure 3.3 the evolution of the roughness length and its standard deviation with time are given for 2 sectors: $|\phi| < 10^0$ and $-30^0 < \phi < -10^0$. This result

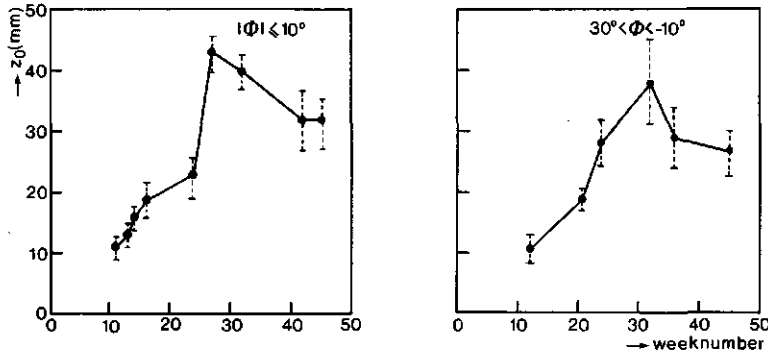


Fig. 3.3 The evolution of the roughness length z_0 and its standard deviation for 2 sectors.

demonstrates that the roughness length of the windward terrain increases from 10 mm to about 40 mm and also that the standard deviation of the individual values is much smaller. After mid-summer the roughness length decreases again, but at a slower rate. In week 25 the high grass between the heather was mowed.

Almost all runs that were accepted, were carried out after week 25. During this period the roughness length did not change much for any sector and had a weighed mean value $z_0 = 35$ mm. In the further analysis, this value was adopted as an overall mean value.

3.1.3 Velocity and temperature deviation

Obukhov (1941, 1971) showed that the dimensionless velocity deviations

$\frac{\sigma_{v1}}{u_*}$, $\frac{\sigma_{v2}}{u_*}$ and $\frac{\sigma_{v3}}{u_*}$ are universal functions of the atmospheric stability parameter, $\frac{x_3}{L}$, only. He obtained the same result for the dimensionless tempera-

ture deviation $\frac{\sigma_T}{T_*}$, defining the temperature scale, T_* , as $T_* = \frac{-\sqrt{3}T}{u_*}$.

Experimental evidence supports these results (Monin & Obukhov, 1954; Wyngaard & Coté, 1971 and Panofsky et al., 1977). During our measurement campaign these deviations were determined by means of the sonic anemometer-thermometer data. The results for $\frac{\sigma_{v3}}{u_*}$ and $|\frac{\sigma_T}{T_*}|$ are given in figures 3.4 and 3.5 respectively. Also plotted in figure 3.4* there are the curves proposed by Panofsky et al. (1977):

$$\frac{\sigma_{v3}}{u_*} = 1,3(1 - \frac{x_3}{L})^{1/3} \quad \text{for } \frac{x_3}{L} < 0 \quad (3.4)$$

and

$$\frac{\sigma_{v3}}{u_*} = 1,3 \quad \text{for } \frac{x_3}{L} > 0.$$

Also given in figure 3.5 is the curve proposed by Wyngaard & Coté (1971):

$$|\frac{\sigma_T}{T_*}| = 0,95(-\frac{x_3}{L})^{1/3} \quad \text{for } \frac{x_3}{L} < 0. \quad (3.5)$$

Taking into account that the scatter in our data is comparable to that given

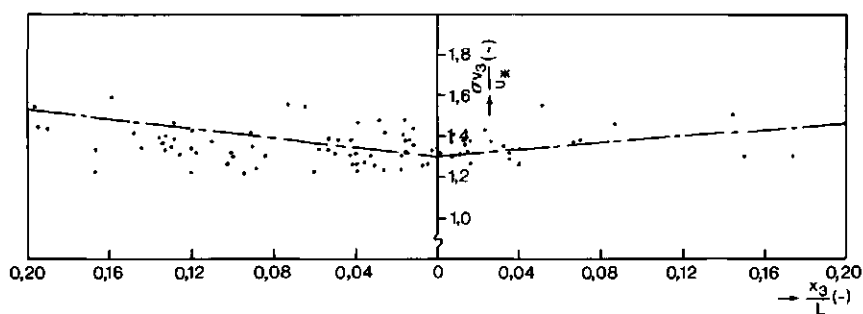


Fig.3.4 $\frac{\sigma_{v3}}{u_*}$ as a function of the thermal stability parameter $\frac{x_3}{L}$.

— mean curve from Kansas data (Panofsky et al., 1977).

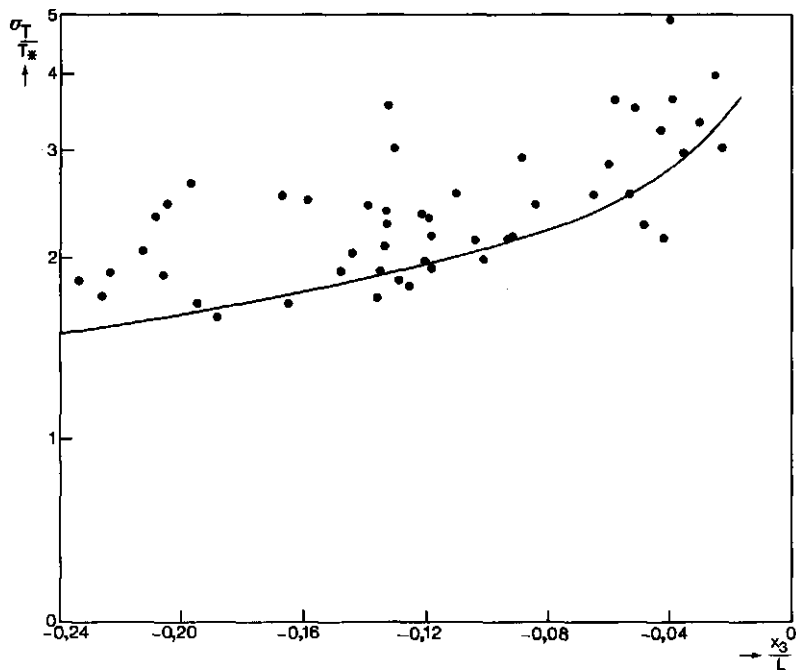


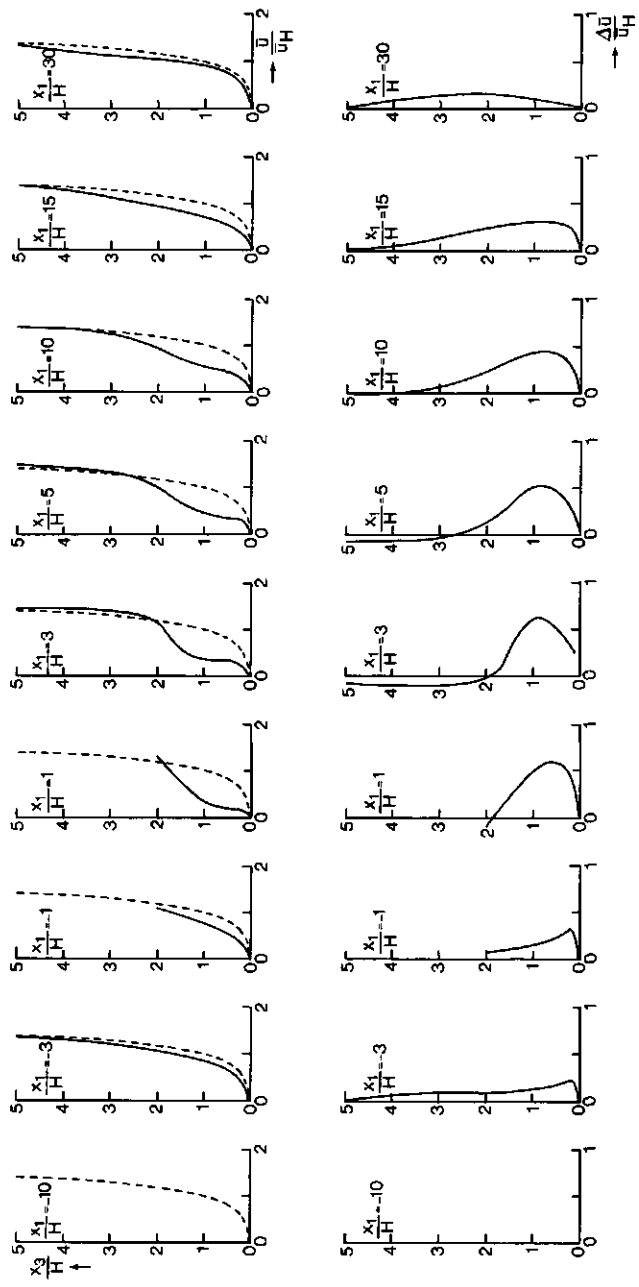
Fig. 3.5 $\frac{\sigma_T}{T_*}$ as a function of the thermal stability parameter, $\frac{x_3}{L}$, for the unstable case. — mean data Kansas experiments (Wyngaard & Coté, 1971).

by Panofsky et al. (1977) and Wyngaard & Coté (1971), we conclude that our results are somewhat higher but are compatible with theirs.

3.2 DISTURBED MEAN WIND FIELD

3.2.1 Disturbed wind field for perpendicular flow direction and thermally neutral stratification

In figure 3.6, the dimensionless mean speed profiles, $\frac{u}{u_H}$ and speed deficits,



88 Fig. 3.6 The mean wind speed and deficit profiles around the barrier for near-neutral stratification ($\beta^* = -0.002$) and perpendicular flow direction ($\phi = +1^\circ$). ---- undisturbed wind speed profile.

$\frac{\Delta \bar{u}}{\bar{u}_H} = \frac{\bar{u}_H - \bar{u}}{\bar{u}_H}$, are plotted for a run in near-neutral atmospheric stratification

($|\frac{H}{L}| = 0,002$) and a nearly perpendicular angle of attack ($\phi = 1^0$). All barrier properties mentioned in Ch 1 can be easily recognized in this picture. At every measuring level, a speed reduction is observed ahead of the barrier. Just behind the barrier, there is a calm region extending roughly from the surface to the barrier height. The maximum height just behind a barrier up to where a perceptible reduction takes place, is known in the literature (Plate, 1971) as the sheltered height H^* . Generally, for a closed obstacle, this height is accepted as being about 1,7 times the height of the obstacle. Our data show a sheltered height $H^* = 1,8$ at $x_1 = H$. Just over the barrier at the leeward side, the vertical speed gradient is very steep. This gradient gradually decreases as the distance from the barrier increases. The greatest speed deficit occurs just behind the obstacle below the barrier height. With increasing distance from the barrier, the maximum deficit gradually decreases and in addition shifts to a higher level. At the farthest location ($x_1 = 30 H$), the measured profile and the original one still differ, which means that for a closed obstacle the region influenced appreciably is larger than $30 H$.

With the results of figure 3.6, a picture of the reduction was constructed and depicted in figure 3.7. Here the reduction is defined as,

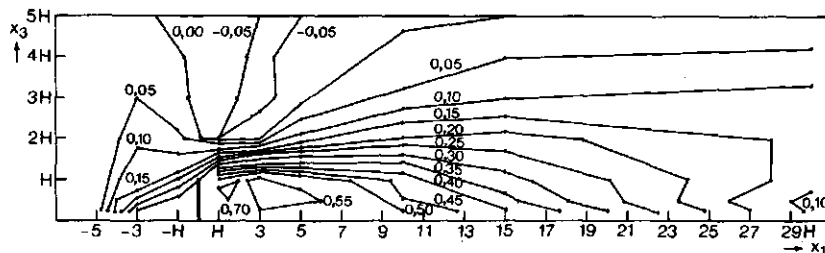


Fig. 3.7 The mean relative wind speed reduction, $R = \frac{\bar{u}(-10H, x_3) - \bar{u}(x_1, x_3)}{\bar{u}(-10H, x_3)}$, around the barrier in a near-neutral atmosphere ($\frac{H}{L} = - 0,002$) and perpendicular flow direction.

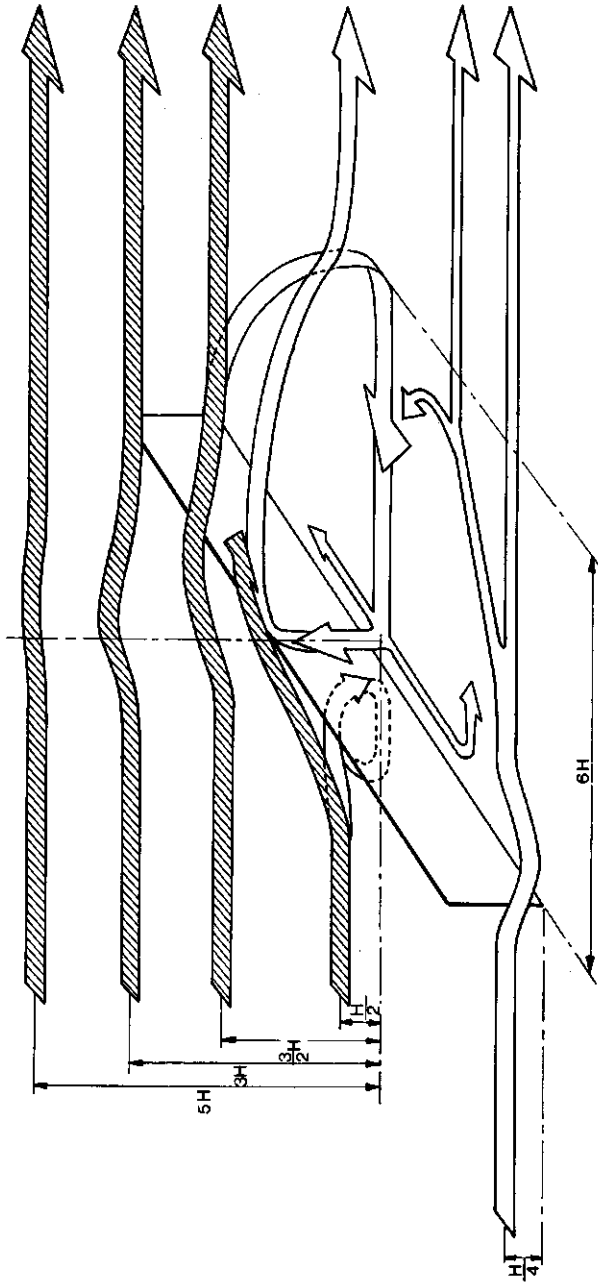
$$R = \frac{\bar{u}(-10H, x_3) - \bar{u}(x_1, x_3)}{\bar{u}(-10H, x_3)} \quad \text{and in figure 3.7 the iso-reduction lines are}$$

plotted between the calculated interpolated points. This picture indicates clearly that the reduction starts just ahead of the barrier, especially near the surface. Just behind the barrier, near the surface, the greatest reduction occurs. Furthermore, behind the barrier, the reduction decreases very gradually and at the farthest station there is still a mean reduction of about 0,1. In the literature (Jensen, 1958) often a sheltered area is given, defined as the area near the surface ($x_3 = \frac{H}{3}$), at which the reduction is at least 0,2. From figure 3.7 it can be deduced that in our experiment this area extends to about $x_1 = 24 H$.

The wind profiles were measured with cup anemometers, which only give a limited picture of the disturbed flow field, especially just around the barrier. That is why additional observations were carried out with a large number of simple wind vanes and smoke visualizations. An artist impression of these observations is depicted in figure 3.8. These visualizations showed that in front of the barrier a recirculation bubble occurs. This front bubble starts near the surface at about $-0,5 H$ and reattaches on the obstacle at a height between $0,5 H$ and H . Wind tunnel experiments confirm this and show that the dividing streamline starts on the surface at $-0,5 H$ and ends on the barrier at a height $0,6 H$ (Good & Joubert, 1968). Behind the barrier a rear recirculation bubble occurs starting at the top of the barrier and ending on the surface at a distance between $5 H$ and $10H$. Field visualization experiments, performed by Ogawa & Diosey (1980), confirm this and show that the reattachment point is at $6H$ for a closed barrier. Moreover, our visualizations showed the influence of the finite width of the barrier on the disturbed flow. At perpendicular incidence angle, a weak recirculation bubble occurs near the surface at the edges of the barrier. This indicates that the recovery of the wind profiles not only takes place from above but also from the sides.

3.2.2 Effect of thermal stratification

In the analysis of the thermal stratification effect, we selected an unstable ($\frac{H}{L} = -0,09$) and a stable run ($\frac{H}{L} = +0,09$) in which the wind was nearly per-



31 Fig. 3.8 An artist impression of the flow around a barrier of finite width.

pendicular ($|\phi| < 1^0$) to the barrier. The dimensionless undisturbed profiles, $\frac{\bar{u}}{u_H}$, and the dimensionless speed deficits, $\frac{\Delta\bar{u}}{u_H} = \frac{\bar{u}(-10H, x_3) - \bar{u}(x_1, x_3)}{u_H}$, of these runs have been plotted in figure 3.9. Besides, in figure 3.10 the relative wind speed of these runs, $\frac{\bar{u}}{u_R} = \frac{\bar{u}(x_1, x_3)}{\bar{u}(-10H, x_3)}$, and the results of the near-neutral run ($\frac{H}{L} = -0,002$) have been plotted for 3 levels, thus enhancing the discernibility of the stratification effect on the speed recovery.

From the results of figure 3.9 we can easily see the stability effect on the undisturbed wind profiles: with increasing instability, the wind shear decreases at the higher levels. In addition, with increasing instability the undisturbed wind profile has more horizontal momentum near the surface. This means that with increasing instability, just in front of the barrier, more mass has to deflect in upward direction in order to pass the barrier. It is fair to expect that with increasing instability the normalized wind speeds will increase just behind the barrier at the higher levels, and, in addition, the normalized speed deficits will increase at the lower levels. These effects are in fact shown quite clearly in the results in the figures 3.9 and 3.10. With increasing distance from the barrier, which is clear from these results, the speed deficits gradually decrease and the fastest speed profile recovery takes place in the unstable atmospheric condition. In the stable case, however, we see that below about $x_3 = 2 H$ the recovery of the wind speed profile is faster than in the near-neutral case.

In a disturbed flow, the exchange process for momentum is dependent on the turbulence of the original undisturbed flow and on the turbulence generated by the barrier. The turbulence of the original flow, however, is highly dependent on the thermal stratification: an increasing instability is coupled with an increasing turbulence level. Consequently, we suppose that a faster recovery of the speed profile occurs with increasing instability. On the other hand, the speed deficits just behind the barrier are smaller with increasing thermal stability. That is probably the reason why in the stable case the speed profile recovery near the surface is faster than in the near-neutral case.

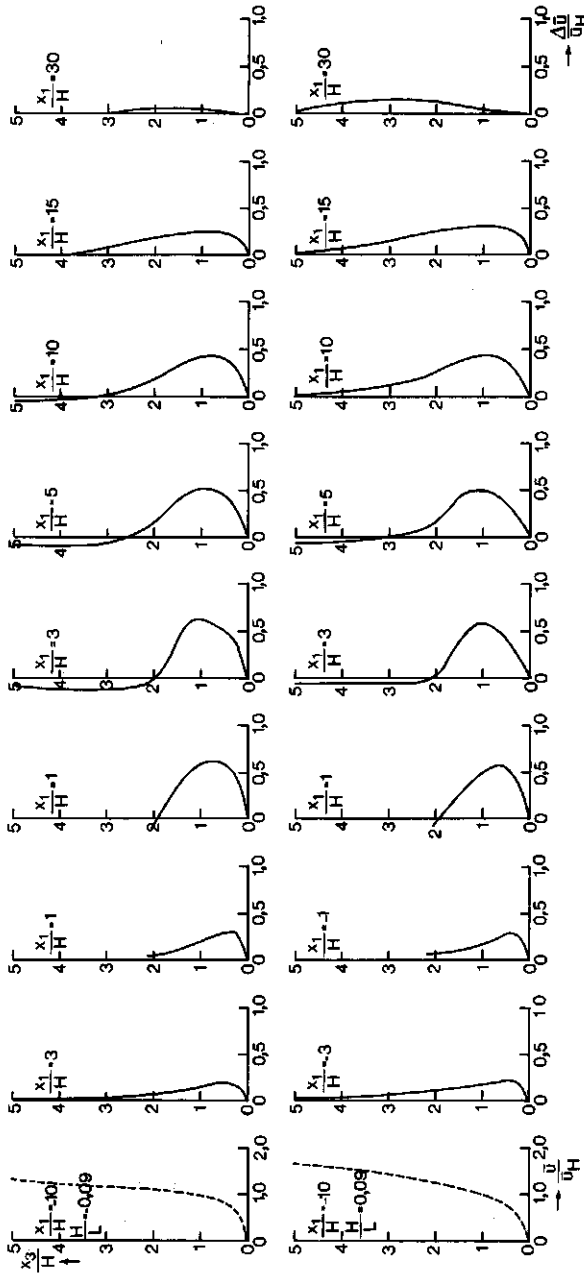


Fig. 3.9 The relative undisturbed wind profile, $\frac{\bar{u}}{u_H} = \frac{\bar{u}}{\bar{u}(-10H, H)}$, and the relative speed deficits,

$$\frac{\Delta \bar{u}}{\bar{u}_H} = \frac{\bar{u}(-10H, x_3) - \bar{u}(x, x_3)}{\bar{u}_H}$$

in unstable ($\frac{H}{L} = -0,09$) and stable ($\frac{H}{L} = +0,09$) stratification and perpendicular flow direction.

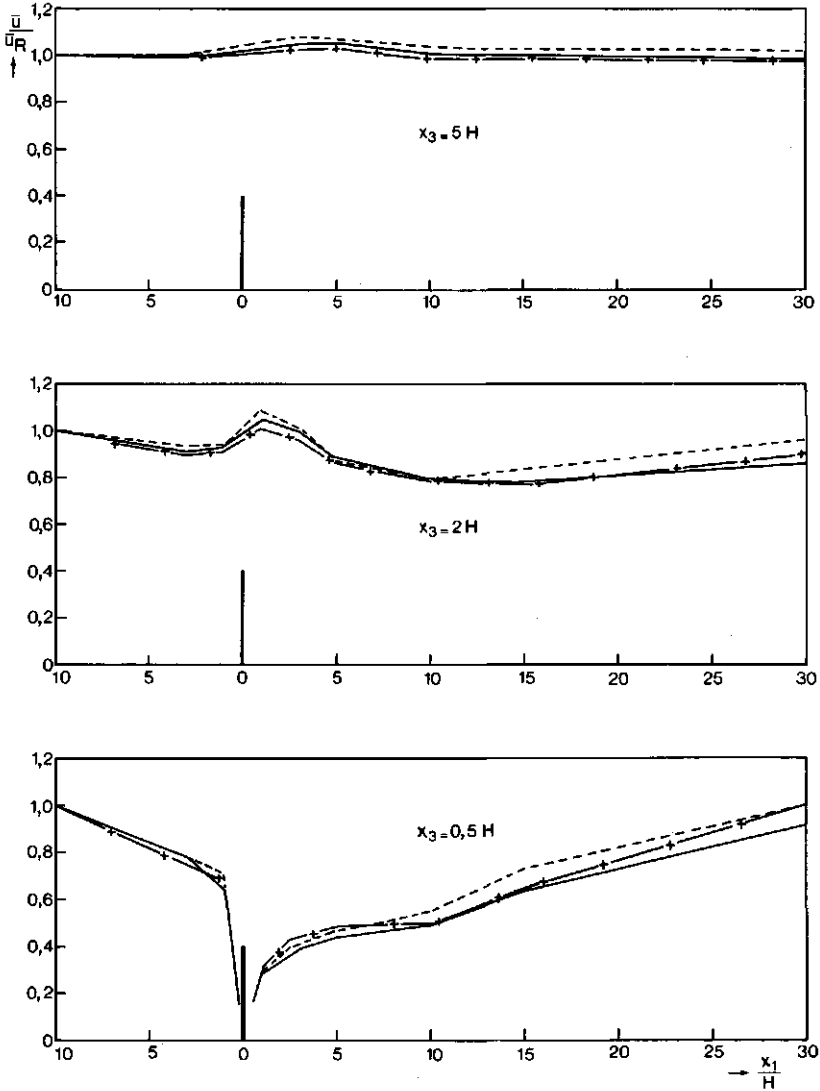


Fig. 3.10 The relative mean wind speed $\frac{\bar{u}}{\bar{u}_R} = \frac{\bar{u}}{\bar{u}(-10H, x_3)}$ for 3 levels and 3

different thermal stratifications, for perpendicular incidence angle ($\phi < 2^\circ$). — $\frac{H}{L} = -0,002$; --- $\frac{H}{L} = -0,09$; -·-·- $\frac{H}{L} = +0,09$.

For all runs with an incidence angle $|\phi| < 3^\circ$, the sheltered distance was determined in order to investigate if there exists a relation between this distance and the stability parameter $\frac{H}{L}$. From these results, plotted in figure 3.11, it can be concluded that this distance changes significantly with $\frac{H}{L}$ in unstable stratifications. Here the sheltered distance decreases from

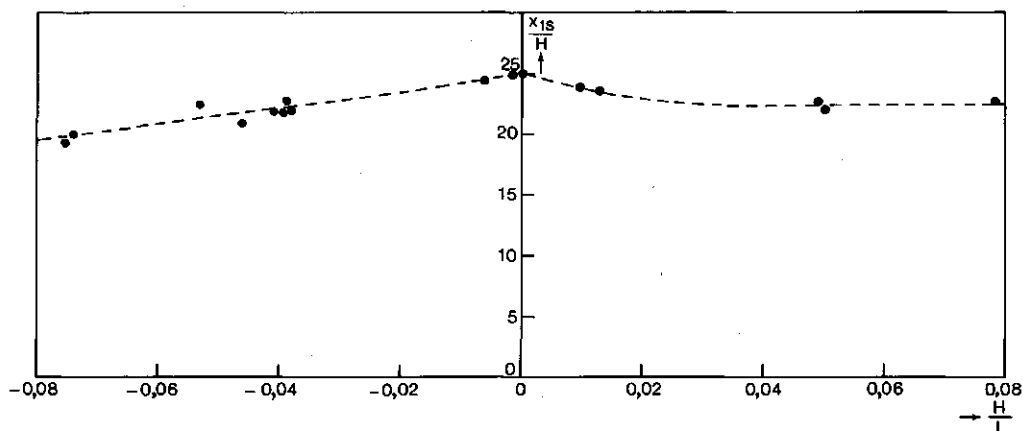


Fig. 3.11 The dependence of the sheltered distance on the thermal stratification for perpendicular flow direction.

$x_{1s} = 24 H$ for neutral conditions to about $x_{1s} = 17,5 H$ at $\frac{H}{L} = -0,1$. For stable stratifications, however, this distance remains almost constant up to $\frac{H}{L} = +0,1$ with a mean value of $x_{1s} = 23 H$.

3.2.3 Oblique flow conditions

The disturbed wind profiles in oblique flow are analyzed first for two near-neutral runs ($\frac{H}{L} = -0,01$). We selected angles of attack of $\phi = 22^\circ$ and $\phi = 40^\circ$. The measured relative wind speed profiles and deficits are presented in figure 3.12 and figure 3.13, respectively.

It can be seen from these results that after apparent recovery has taken place, the next measuring location shows a little overshoot in the wind speed near the surface (in figure 3.12 and figure 3.13, the wind speed overshoot regions have been hatched). To analyze this effect in more detail, we plotted in

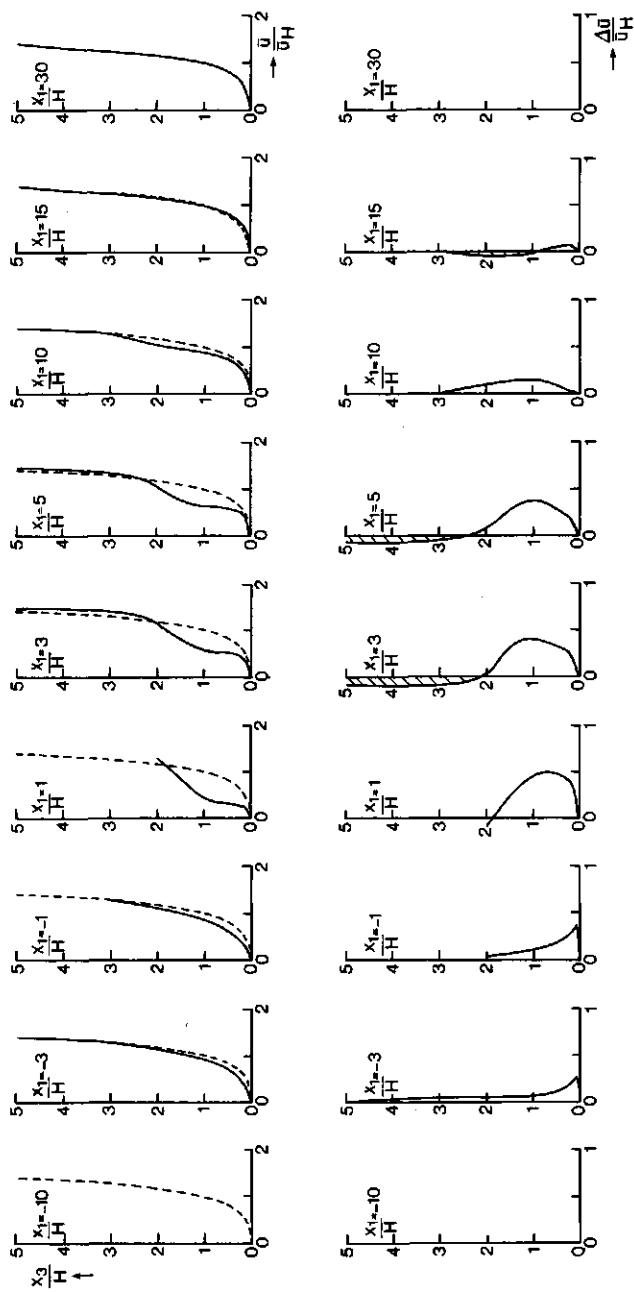


Fig. 3.12 The relative disturbed wind speed and deficit profiles in near-neutral stratification and an incidence angle $\phi = -22^\circ$, --- undisturbed wind profile.

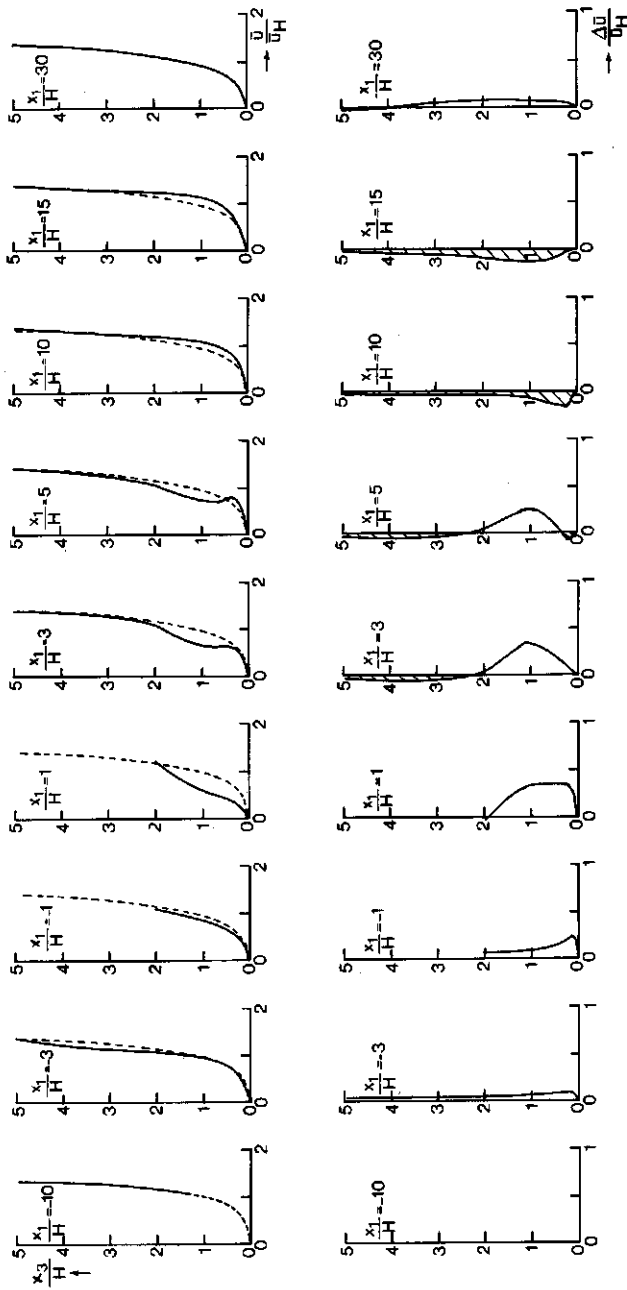


Fig. 3.13 The relative disturbed wind speed and deficit profiles in near-neutral stratification and an incidence angle $\phi = -40^\circ$. --- undisturbed wind profile.

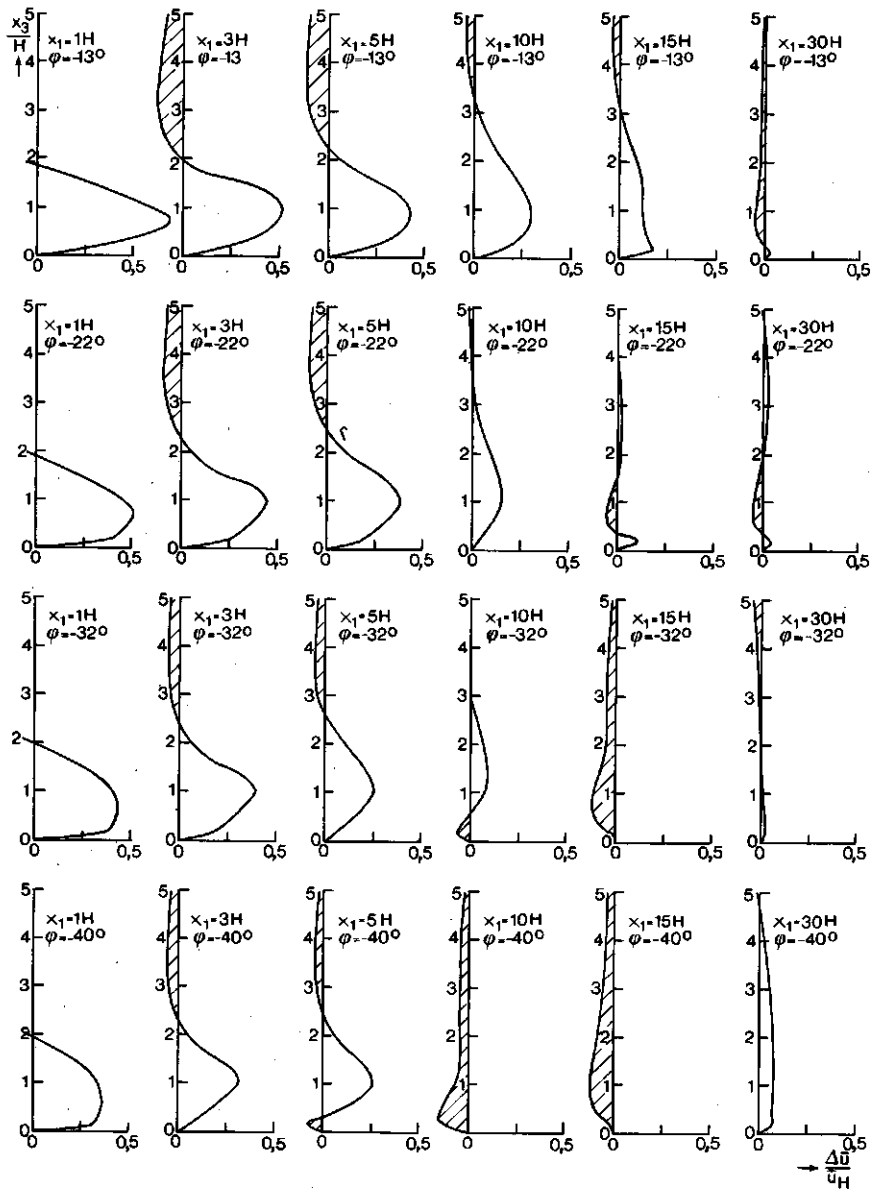


Fig. 3.14 The mean relative wind speed deficits in near-neutral stratification for several incidence angles ϕ .

figure 3.14 the speed deficit profiles behind the barrier for incidence angles $\phi = 13^\circ, 22^\circ, 32^\circ$ and 40° . From this result we can deduce an overshoot region followed by an undershoot region and, moreover, these regions can be observed to shift to the barrier with increasing incidence angle.

Physically, an overshoot in the wind speed near the surface, followed by an undershoot can be explained by means of a line vortex that is deflected by the finite width of the barrier (see figure 3.15). The undisturbed fluid

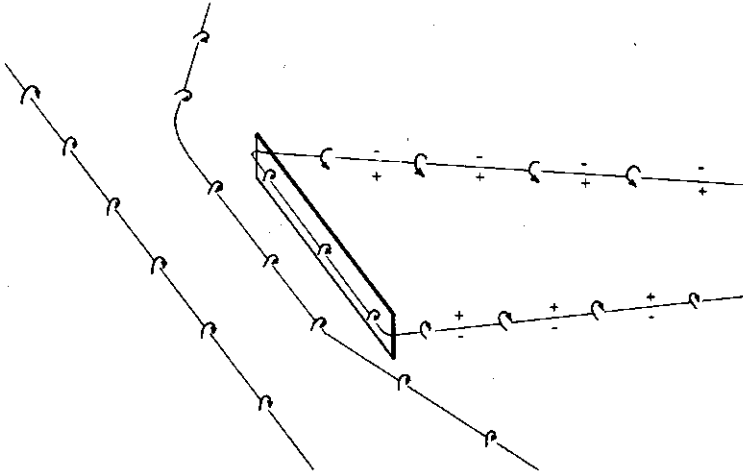


Fig. 3.15 The deflection of the line vortex near the surface, due to the finite width of the barrier.

+ region of increasing speed; - region of decreasing speed.

flow has a line vortex, determined by the speed gradient near the surface. Near the barrier this line vortex is deflected due to the finite width of the barrier. As a result, high momentum from above is transported downward at one side of the deflected line vortex and low momentum is transported upward at the other side of the vortex line behind the barrier.

With the data of figure 3.14, we tried to locate the regions where an overshoot of the wind speed near the surface occurs. As a rough estimate we found a sector of 30° around the incidence angle, which originates at the windward barrier edge (figure 3.16). The left part of this sector indicates an overshoot and the right part an undershoot of the wind speed.

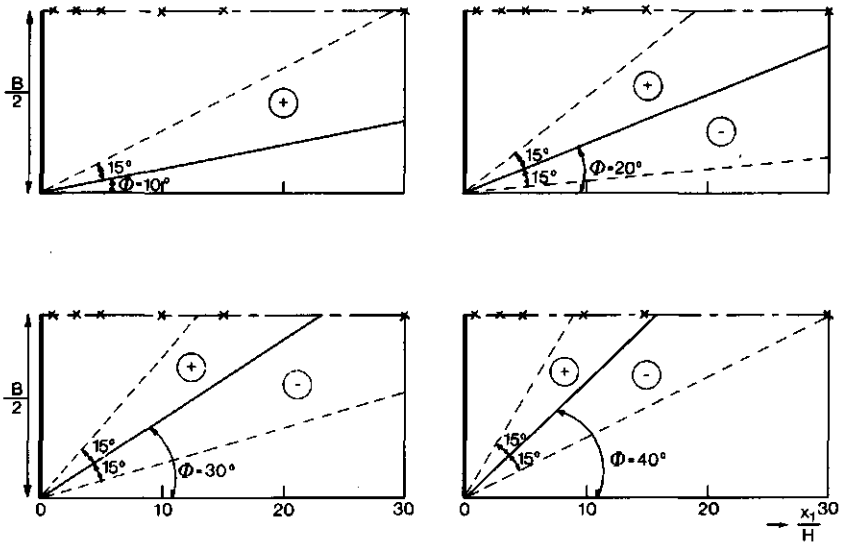


Fig. 3.16 The overshoot \oplus and undershoot \ominus areas for different incidence angles ϕ ; x is mast location.

If we have a barrier of infinite width, the sheltered distance equals the simple cosine relation $x_{1s}(\phi=0) \cdot \cos \phi$. In the case of a barrier of finite width, however, the sheltered distance is dependent on the width as well. If the width of the barrier is not too small, the sheltered distance follows also the simple cosine relation for incidence angles if not too wide. For wide incidence angles, however, the disturbed flow flows within the location $x_{1s}(\phi) = x_{1s}(\phi=0) \cdot \cos \phi$ (figure 3.17). In a first order approximation the apparent sheltered distance, x_{1s}^* , is now determined by the width of the barrier and by the overshoot area and equals:

$$x_{1s}^* = \frac{B}{2} \cdot \cot(\phi + \alpha) \cdot \cos \phi. \quad (3.4)$$

Here B stands for the width of the barrier and α for the sum total of the angles constituted by the overshoot sector of 15° and the angle of the sector between 100% apparent recovery and 80% apparent recovery of the speed profile. From the data of figure 3.14 we can deduce that the latter angle is approximately 10° so $\alpha = 25^\circ$.

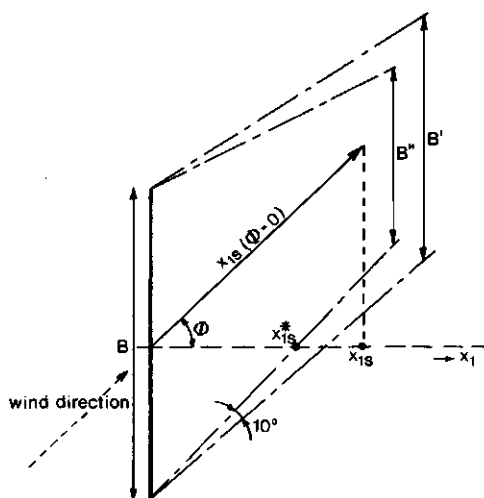


Fig. 3.17 The apparent sheltered distance x_{1s}^* near the surface ($x_3 = \frac{H}{3}$) for wide incidence angles. B is the width of the barrier; B' the width of the wake for 100% recovery for a finite barrier; B'' the width of the wake for 80% recovery; x_{1s} the sheltered distance for an infinite barrier.

To analyze the sheltered distance in more detail, we have given x_{1s} for all runs in figure 3.18 as a function of the incidence angle $|\phi|$. Moreover, in this figure we have plotted the cosine relation for a barrier of infinite width and the relation (3.4) for a barrier of width $B = 32 H$. From these results the very strong dependence of the incidence angle on the sheltered distance is obvious, being due mainly to the width of the barrier. Besides, from figure 3.18 it can be seen that all observed sheltered distances lie below the theoretical curve (3.4). If this curve is translated 8° to the left, the agreement is much better.

For porous obstacles several studies have been carried out in order to determine the incidence angle dependence on the sheltered distance. The results for barriers of 50% porosity from the work of various authors are plotted in figure 3.19. In addition, in this figure we have given the cosine relation for an infinite barrier and the relation (3.4) for a barrier with a width

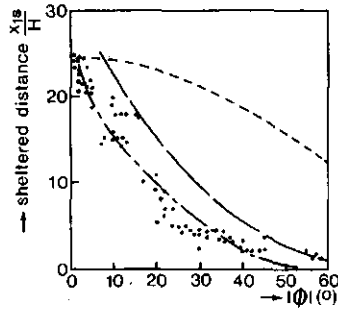


Fig. 3.18 The relative sheltered distance, $\frac{x_{1s}}{H}$, as a function of the incidence angles ϕ . ---- $\frac{x_{1s}(\phi=0)}{H} \cdot \cos\phi$ for infinite barriers; ——— $\frac{B}{2} \cot(\phi+25^\circ)\cos\phi$ for finite barriers; —·—· $\frac{B}{2} \cot(\phi+25^\circ)\cos\phi$ translated 8° to the left.

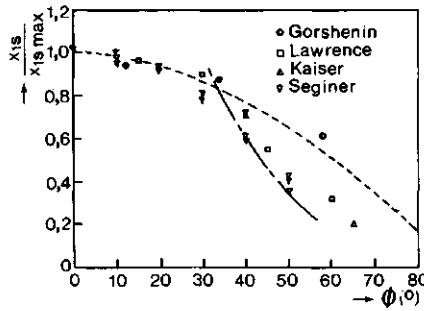


Fig. 3.19 The relative sheltered distance, $\frac{x_{1s}}{x_{1s \max}}$, for porous obstacles (50% porosity) as a function of the incidence angle ϕ . --- $\cos\phi$ for infinite barrier; —·—· $2 \cot(\phi+25^\circ)\cos\phi$ for the finite barrier of Seginer.

$B = 40 H$ (Seginer, 1975). It is evident from this figure that the results follow the cosine relation up to an incidence angle of about 30° . Beyond this angle, the results follow the relation (3.4).

3.2.4 Conclusions about the disturbed mean wind field

The mean wind profile at the farthest location ($x_1 = 30 H$) still deviates significantly from the reference wind profile. At this station, the maximum difference is 15% with respect to the reference wind profile and occurs at a level of about $2 H$ in a thermally neutral atmosphere and a perpendicular flow direction. Atmospheric instability enhances the velocity disturbances; it also leads to a faster recovery of the wind speed profiles. The sheltered distance follows the cosine dependence for barriers of infinite width for not too wide incidence angles. The apparent sheltered distance for wide incidence angles is determined by the width of the barrier and follows in a first order approximation the relation:

$$x_{1s}^* = \frac{B}{2} \cot(\phi + \alpha) \cdot \cos \phi.$$

3.3 TURBULENCE PROPERTIES

3.3.1 Near-neutral stratification

In order to gain more insight into the turbulence properties of the disturbed flow, the r.m.s. values of the speed fluctuations around the barrier were determined. In figure 3.20 the normalized speed fluctuations have been plotted for nearly perpendicular flow direction ($\phi = 1^\circ$) and near-neutral stratification ($\frac{H}{L} = -0,002$). The r.m.s. values, σ_u , are nondimensionized with the r.m.s. values, σ_{uR} , of the same height at the reference location. In figure 3.20 only the data for $x_3 < H$ have been plotted, because these data only could be corrected for instrumental cut-offs (see Ch2).

Ahead of the obstacle, at all levels below the barrier height, the r.m.s. values gradually decrease. A decrease is expected, because the mean streamline curvature causes a reduction of the turbulence intensity if the streamline deflection is upward (Wyngaard et al., 1968). Just behind the obstacle

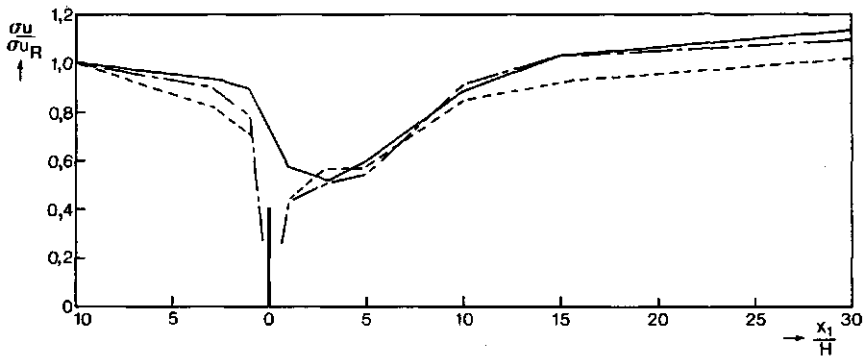


Fig. 3.20 The normalized r.m.s. values of the speed fluctuations,

$$\frac{\sigma_u}{\sigma_{uR}} = \frac{\sigma_u(x_1, x_3)}{\sigma_u(-10H, x_3)}, \text{ for perpendicular flow direction } (\phi=1^0) \text{ and near-neutral stratification } \left(\frac{H}{L} = 0,002\right).$$

$$\text{— } x_3=H; \text{ —•— } x_3 = 0,5H; \text{ --- } x_3 = 0,3H; \frac{\sigma_{uR}}{u_H} = 0,24.$$

and below the barrier height a minimum in the speed fluctuations is observed, whereas at the obstacle height the minimum is shifted downstream. Further downstream the speed fluctuations increase and, at the levels $x_3 = 0,5 H$ and $x_3 = H$, even exceed the undisturbed values near the station $x_1 = 15 H$. At the level $x_3 = 0,3 H$, beyond $x_1 = 10 H$, the speed fluctuations increase somewhat slower. Nevertheless, near the location $x_1 = 30 H$ the undisturbed value, too, is exceeded. If we define a second sheltered distance, x_{1S}' , as the distance at which the reduction of the r.m.s. values of the speed fluctuations, $\frac{\sigma_{uR} - \sigma_u}{\sigma_{uR}}$, near the surface ($x_3 = \frac{H}{3}$) is at least 0,2, we find for this distance $x_{1S}' = 9 H$ in the near-neutral case. This distance is much shorter than the sheltered distance for the mean wind speed ($x_{1S} = 24 H$), which signifies that the sheltering for the speed fluctuations is restricted to a region close to the barrier.

However, our results deviate from those obtained by Hagen & Skidmore (1971).

Hagen & Skidmore measured the r.m.s. velocity components at $x_3 = 0,5 H$ with two anemometer bivanes simultaneously, one of which was permanently placed at their reference location ($x_1 = -12 H$) and the other one at their location $x_1 = 2 H, 6 H, 12 H$ or $20 H$. Their results and ours at the level $x_3 = 0,5 H$ have been plotted in figure 3.21. The thermal stratification was estimated at

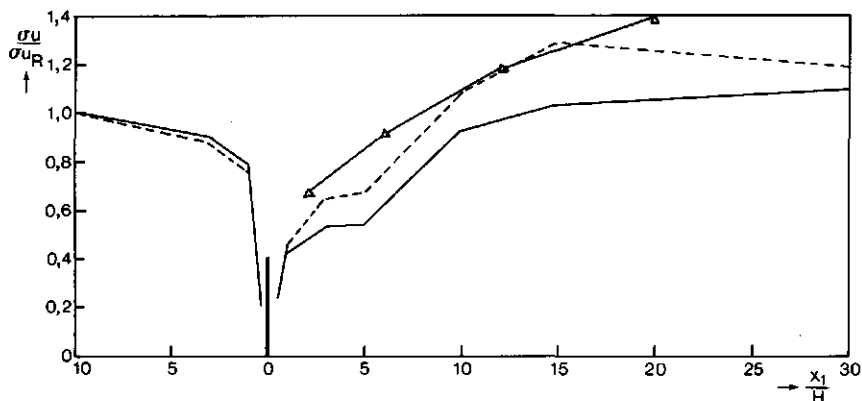


Fig. 3.21 The normalized r.m.s. values of the speed fluctuations,

$$\frac{\sigma_u}{\sigma_{uR}} = \frac{\sigma_u(x_1, x_3)}{\sigma_u(-10H, x_3)}, \text{ at a height of } x_3 = \frac{H}{2} \text{ and perpendicular flow direction. } \text{---} \frac{H}{L} = -0,002; \text{---} \frac{H}{L} = -0,09; \triangle-\triangle \text{ data of Hagen \& Skidmore (1971).}$$

their reference location by measuring the bulk Richardson number, but they do not report a numerical value. In the next section, though, we will see that our results in unstable stratification reflect the results of Hagen & Skidmore much better.

3.3.2 Non-neutral stratification

The effects of thermal stratification were studied by selecting an unstable run ($\frac{H}{L} = -0,09$) and a stable run ($\frac{H}{L} = +0,09$). The normalized r.m.s. values of the speed fluctuations have been plotted in figure 3.22.

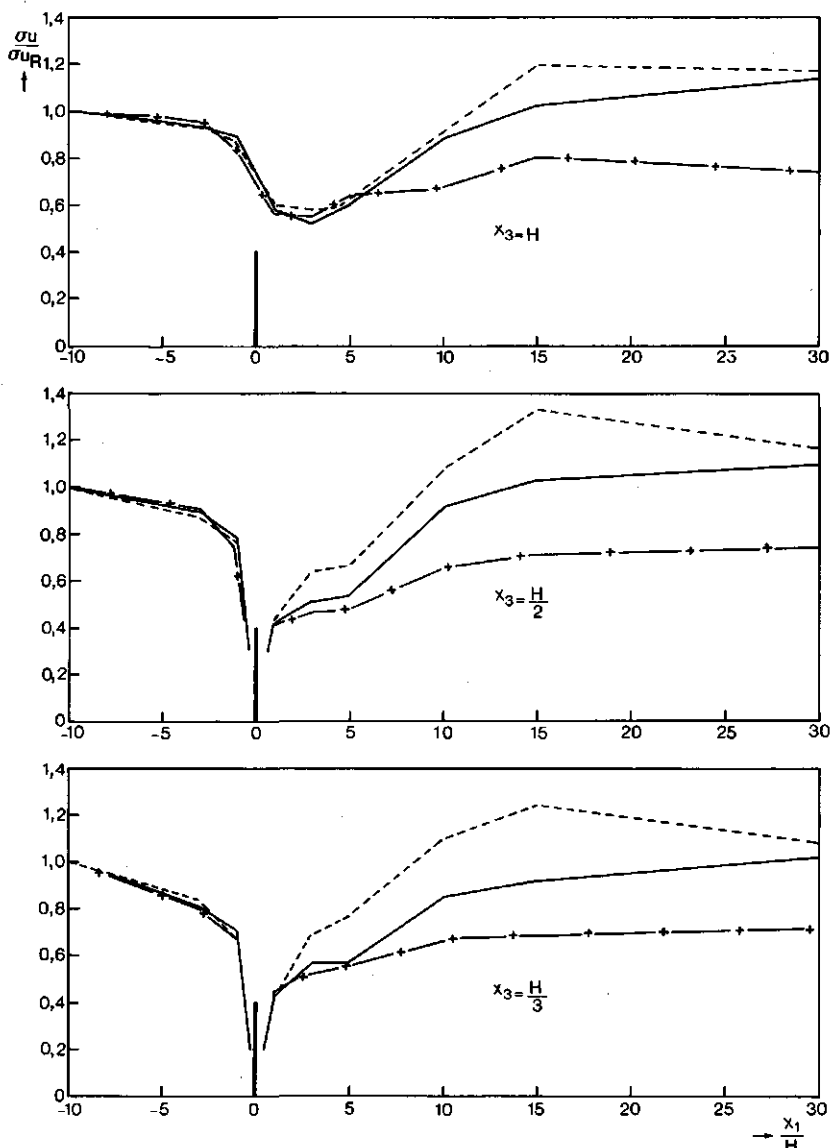


Fig. 3.22 The normalized speed fluctuations, $\frac{\sigma_u}{\sigma_{uR}} = \frac{\sigma_u(x_1, x_3)}{\sigma_u(-10H, x_3)}$, for levels below the obstacle height in 3 different thermal stratifications and nearby perpendicular incidence angle ($\phi < 2^\circ$). --- $\frac{H}{L} = -0,09$ and $(\frac{\sigma_{uR}}{u_H})_H = 0,31$. — $\frac{H}{L} = -0,002$ and $(\frac{\sigma_{uR}}{u_H})_H = 0,24$; —+— $\frac{H}{L} = +0,09$ and $(\frac{\sigma_{uR}}{u_H})_H = 0,27$.

From this result it is easy to see that the stratification effect on the turbulence is much greater than the effect on the speed deficits (see e.g. figure 3.12). In both the stable and the unstable case, the speed fluctuations just around the barrier are reduced, but the increase rate is much higher for all levels since the stratification is more unstable. Besides, in the stable case we see that the disturbed speed fluctuations remain below the undisturbed values for all levels and all measuring stations.

As one may see from figure 3.12, in the disturbed flow the greatest wind shear for all stability cases occur between the levels $x_3 = H$ and $x_3 = 2H$ and here mainly the new turbulence is generated. Below the level $x_3 = H$, the shear is quite small for all stability cases. That is why it is reasonable to assume that below $x_3 = H$ the increase of the turbulent kinetic energy with increasing distance from the barrier is caused mainly by a flux from above. Besides, the turbulence level in an unstable atmosphere is higher than in a stable atmosphere, in which the turbulence is strongly suppressed. Since a high turbulence level is coupled with better mixing, the increase in turbulence at the lower levels, to all probability, is faster with increasingly unstable stratification. The results of figure 3.22 do show these effects clearly indeed.

When the r.m.s. data of the speed fluctuations of the unstable case are also plotted in figure 3.21, we find that they are in much better agreement with the data of Hagen & Skidmore. Perhaps the data of Hagen & Skidmore were obtained in thermally unstable stratification. To estimate the thermal stratification, Hagen & Skidmore measured the bulk Richardson number, which is defined as:

$$Ri_B = \frac{g}{T} \cdot \frac{\left(\frac{dT}{dx_3}\right) H}{2 \bar{u}_H} \cdot H^2.$$

As Golder (1972) showed, this stability parameter is uniquely related to the Richardson gradient number for a given terrain roughness. Hence, the bulk Richardson number can be accepted as a correct parameter to indicate the thermal stratification. Hagen & Skidmore did their measurements during daylight hours only and do not report any numerical value for this parameter. However, there are more differences between our experiments and those of

Hagen & Skidmore that may be responsible for the discrepancy. First, Hagen & Skidmore performed their measurements over a smoother terrain, characterized by a roughness length $z_0 = 9,44$ mm. Second, the width-to-height ratio of their barrier was somewhat smaller (approximately $\frac{B}{H} = 25$).

3.3.3 Conclusions about the disturbed turbulence

The sheltered distance for the r.m.s. value of the speed fluctuations, σ_u , is much shorter than the sheltered distance for the mean wind speed in a near-neutral atmosphere. The increase in σ_u , below the level $x_3 = H$, is caused by a flux of turbulent kinetic energy from above. The effect of the thermal stratification on σ_u is greater than the effect on the speed deficits. In an unstable atmosphere, σ_u increases near the surface ($x_3 = \frac{H}{3}$) and exceeds the undisturbed value, σ_{uR} , significantly.

In a stable atmosphere, σ_u near the surface ($x_3 = \frac{H}{3}$) is strongly suppressed and recovers very slowly without exceeding the undisturbed value.

4 Results of the drag coefficient measurements

4.1 INTRODUCTION

If a body is placed in a flow field, a force will be exerted on this body by the fluid flow. Limiting ourselves to the force parallel to the flow direction, two kinds of forces can be recognized: the friction force and the pressure force. Due to the tangential stress along the body, caused by the internal friction in the fluid, a force termed the friction drag is generated. This kind of drag mainly occurs over "streamlined" or slender bodies that are aligned with the mean flow direction. In addition, at the surface of the body a pressure force normal to the surface is induced. The integral of the component of this pressure parallel to the flow is termed the form drag. This kind of drag predominates for slender bodies not aligned with the mean flow and for bluff bodies. The flow separates; in the wake downstream of the body the flow is severely distorted.

In our experiment, where a fence is placed more or less perpendicular to the flow, we have a typical bluff body flow, in which the friction drag is negligible.

The drag on a body depends on its shape, the orientation of the body in the flow field and the properties of the flow field itself. In general one hopes to be able to predict the drag of a given bluff body from the knowledge of the properties of the flow field in which it is erected. The complexity of turbulence is such that an analytical solution is not possible in the present state of knowledge and recourse must be made to experiments.

For a given bluff body, successful dependences on the drag can be obtained on the basis of dimensional analysis. If the undisturbed flow is characterized by the speed \bar{u}_H at height H , the thermal stratification by the Obukhov length L , the surface roughness by z_0 and the flow direction by the angle ϕ , then the drag coefficient for a two-dimensional barrier of infinite width, C_d , can be expressed as:

$$C_d = \frac{D}{\frac{1}{2} \rho \bar{u}_H^2 H} = f\left(\frac{\bar{u}_H \cdot H}{v}, \frac{H}{z_0}, \frac{H}{L}, \phi\right), \quad (4.1)$$

where D represents the force on the barrier per unit width.

Eq. (4.1) is valid only for barriers of infinite width. Our barrier, however, had a finite width $B = 32 H$. For a barrier of finite width, the drag coefficient is:

$$C_d = \frac{D'}{\frac{1}{2} \rho \bar{u}_H^2 H \cdot B} = f\left(\frac{\bar{u}_H \cdot H}{v}, \frac{H}{z_0}, \frac{H}{B}, \frac{H}{L}, \phi\right), \quad (4.2)$$

where D' represents the total force acting on the barrier and $\frac{H}{B}$ represents the aspect ratio i.e. the height-to-span ratio.

For a perpendicular flow direction, however, the former expressions for the drag coefficient are equivalent if the aspect ratio, $\frac{H}{B}$, is small enough. Hoerner (1965) showed that for a rectangular plate, placed in a uniform flow, both expressions are equivalent within 5% for an aspect ratio $\frac{H}{B} \leq 0,01$. In our experiment the aspect ratio $\frac{H}{B} = 0,03$, hence it is reasonable to assume that the drag coefficient depends on the aspect ratio.

During the measurement campaign, we measured the drag, D'_n , perpendicular to the barrier. This force, nondimensionized in the same way as in eq. (4.2), is called the normal-force coefficient C_n (Hoerner 1965):

$$C_n = \frac{D'_n}{\frac{1}{2} \rho \bar{u}_H^2 H \cdot B} = g\left(\frac{\bar{u}_H \cdot H}{v}, \frac{H}{z_0}, \frac{H}{B}, \frac{H}{L}, \phi\right). \quad (4.3)$$

In the next sections the normal-force coefficient, (4.3), will be determined for a roughness parameter $\frac{H}{z_0} = 60$ and an aspect ratio of $\frac{H}{B} = 0,03$.

4.2 RESULTS OBTAINED FROM DIRECT FORCE MEASUREMENTS

During the measurement campaign the perpendicular drag on the barrier was measured directly by means of a measuring plate, which was constructed more or less in the center of the barrier. A local perpendicular drag was measured and this local force, divided by the width of the measuring plate, was assum-

ed to be a correct estimation for the mean perpendicular force per unit width acting on the barrier. Measurements at this plate were carried out only at the end of the campaign, during the months September through December in 1982. During this period the atmospheric stratification was small under westerly wind conditions. Expressed in terms of the Obukhov length, $|\frac{H}{L}| < 0,02$. The force data obtained with this method therefore, could be used to determine the dependence of the Reynolds number and the incidence angle on the normal-force coefficient in thermally neutral stratification.

4.2.1 Dependence of the normal-force coefficient on the Reynolds number

The relationship between the normal-force coefficient and the Reynolds number is determined from perpendicular flow data. Here incidence angles with $|\phi| \leq 5^\circ$ were accepted as "perpendicular". The result is given in figure 4.1, which in the measured Reynolds number range shows a more or less constant value of $C_n = 1,07$ with a standard deviation of 0,04. Consequently, the normal-force on the barrier depends on the momentum flux perpendicular to the barrier ($D \sim \rho \overline{u_H^2}$).

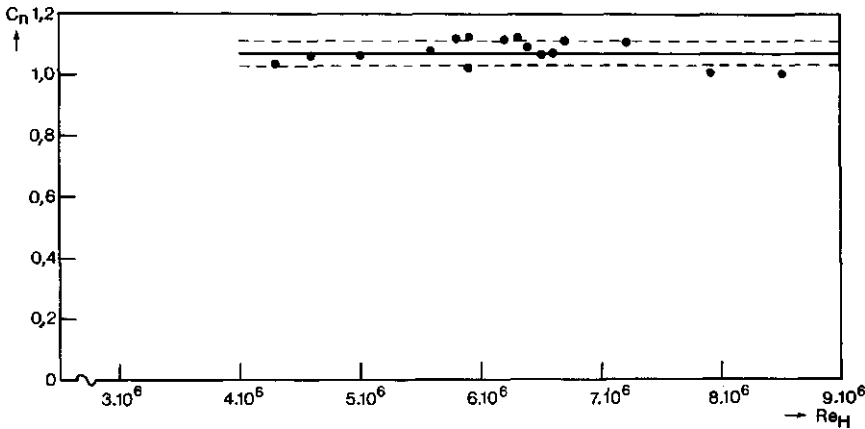


Fig. 4.1 The normal force-coefficient, C_n , as function of the Reynolds number $Re_H = \frac{\overline{u_H} \cdot H}{\nu}$ under near-neutral stratification $|\frac{H}{L}| < 0,02$ and perpendicular flow direction $|\phi| \leq 5^\circ$ ——— mean value; ----- standard error.

For a bluff body the drag coefficient is nearly independent of the Reynolds number if the Reynolds number is high enough. Since we are dealing with a sharp-edged body here, there is no critical Reynolds number, as in the cases of spheres and cylinders.

In wind tunnel studies, where a bluff plate is attached to a smooth wall and is immersed in its boundary layer, a constant drag coefficient is also reported by most authors. Plate (1964), for example, found $C_d = 1,05$ for an infinite barrier attached to a smooth wall and with an approach speed profile $\bar{u} = \bar{u}_\infty \cdot (\frac{x}{\delta})^{1/7}$. Here δ represents the boundary layer thickness and \bar{u}_∞ the undisturbed approach speed. In the same conditions, De Bray (1971) found $C_d = 1,05$ and, with an approach speed profile $\bar{u} = \bar{u}_\infty (\frac{x}{\delta})^{1/7}$, a drag coefficient $C_d = 0,8$.

The only outdoor measurements known to the author, in which the drag was correctly measured are those of Seginer (1975) with a porous line obstacle. Seginer found a normal-force coefficient $C_n = 0,77$ for a barrier with a roughness parameter $\frac{H}{z_0} = 80$ and an aspect ratio $\frac{H}{B} = 0,025$. Seginer did not report the Reynolds number dependence on the normal-force coefficient but he assured us (private communication) that he had found no dependence at all.

4.2.2 Normal-force coefficient in oblique flow

For all incidence angles within the range, $|\phi| \leq 40^\circ$, the normal-force coefficient is presented in figure 4.2. These data show that the normal-force coefficient decreases with increasing angle of incidence. In front of the barrier, a reverse pressure gradient is generated, causing an upward deflection of the flow. In case of an oblique flow, the pressure forces in front of a large solid barrier only correspond to the momentum flux perpendicular to the barrier (Hoerner 1965). Consequently, it must be expected that the normal-force on the barrier depends on $\rho \bar{u}_H^2 \cdot \cos^2 \phi$. With the data of figure 4.2 the relation $C_{no} \cdot \cos^n \phi$ was fitted, in which C_{no} stands for the normal-force coefficient in perpendicular flow direction. For the exponent we found $n = 2,1$, which is in good agreement with the foregoing. The obtained result, $C_{no} \cdot \cos^{2,1} \phi$, too has been plotted in figure 4.2.

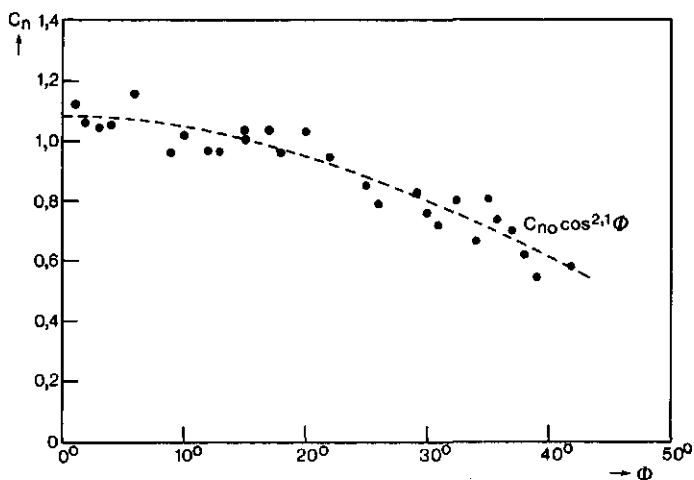


Figure 4.2 The normal-force coefficient measured with the direct force method in thermally neutral stratification ($|\frac{H}{L}| < 0,02$).

It is interesting to note that for porous barriers the normal-force coefficient does not show a $C_{no} \cdot \cos^2 \phi$ dependence. E.g. Seginer (1975), who also investigated the normal-force coefficient dependence in oblique flow, but for a porous fence (50% porosity), found a $C_{no} \cdot \cos \phi$ relation for the same range of angles. The reason for this difference is probably caused by the changes of the flow field in the close vicinity of the barrier. While our wind vane and smoke observations close to the barrier showed a considerable horizontal deflection of the flow, hardly any change of horizontal course was noticed near fences of medium porosity (Seginer, 1975). The barrier of Seginer consisted of vertical slats. For a single slat, Kirchhoff in 1869 and Rayleigh in 1876 with the "free-streamline theory" (see e.g. Batchelor, 1977) already obtained a theoretical expression for the normal-force coefficient:

$$C_n = \frac{\pi \cos \phi}{4 + \pi \cos \phi} \cdot$$

Fage and Johanssen (1927) checked this expression experimentally and found the result for incidence angles $|\phi| < 60^0$:

$$C_n = 2,45 \cdot \frac{\pi \cos \phi}{4 + \pi \cos \phi} \cdot$$

which, except for a proportionality constant, agree well with the theory. The barrier of Seginer consisted of a row of slats, which in a first order approximation for moderate incidence angles, can be considered as a row of independent slats.

4.3 NORMAL-FORCE COEFFICIENTS WITH A MOMENTUM INTEGRAL METHOD

The drag on an obstacle can be calculated also by application of momentum conservation to a control volume around the barrier. For a narrow control volume we found the expression (2.9) in Ch.2:

$$\begin{aligned}
 C_n = & \frac{1}{2} \frac{1}{\rho \bar{u}_H} \int_{z_0}^{x_{3R}} \{ \bar{v}_1(x_{1a}, x_3) - \bar{v}_1(x_{1b}, x_3) \} dx_3 + \frac{1}{2} \frac{1}{\rho \bar{u}_H} \int_{z_0}^{x_{1R}} \{ \bar{v}_1'(x_{1a}, x_3) - \\
 & \bar{v}_1'(x_{1b}, x_3) \} dx_3 \\
 & + \frac{1}{2} \frac{1}{\rho \bar{u}_H} \int_{z_0}^{x_{3R}} (\bar{p}(x_{1a}, x_3) - \bar{p}(x_{1b}, x_3)) dx_3 - \frac{1}{2} \frac{1}{\rho \bar{u}_H} \int_{x_{1a}}^{x_{1b}} \bar{v}_1(x_1, x_{3R}) \bar{v}_3(x_1, x_{3R}) dx_1 \\
 = & C_n(\bar{v}_1) + C_n(\sigma_v) + C_n(\bar{p}) + C_n(\bar{v}_3),
 \end{aligned}$$

where $C_n(\bar{v}_1)$ represents the contribution to the normal-force coefficient due to the mean horizontal momentum flux through the vertical planes of the control volume, $C_n(\sigma_v)$ the contribution due to the turbulent momentum flux, $C_n(\bar{v}_3)$ the contribution due to the mean horizontal momentum flux through the ceiling of the control volume and $C_n(\bar{p})$ the contribution due to the pressure difference. The vertical velocity component, \bar{v}_3 , was calculated by using the mean two-dimensional continuity equation:

$$\bar{v}_3 = - \int_{z_0}^{x_3} \frac{\partial \bar{v}_1}{\partial x_1} dx_3.$$

In the course of the campaign, however, a serious difficulty appeared: with the cup anemometers the speeds of the distorted wind profiles were measured, but the wind direction was not. Very close to the barrier, the local wind direction can deviate considerably from the mean undisturbed wind direction and

the momentum integral method proved to be very sensitive to this. That is why around the barrier observations were made with a large number of simple wind vanes and with smoke. From this visualization it appeared that in perpendicular flow direction at the front surface of the control volume the wind direction agreed well with the undisturbed direction. At the rear surface above the obstacle height, the same was observed, but below this height the flow was reversed most of the time (see figure 4.3a). That means that if the normal-force coefficient is calculated with the measured speed values, the

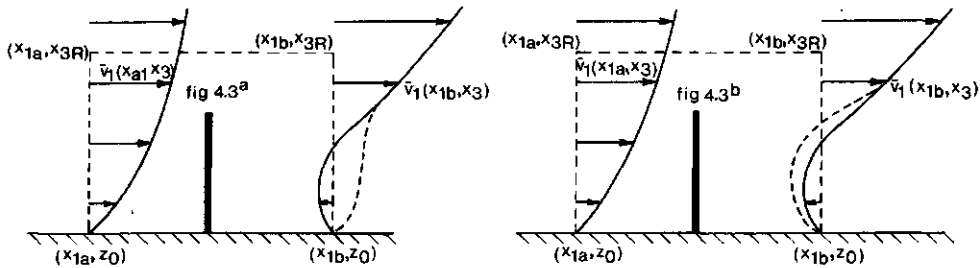


Fig. 4.3 The wind profiles around the barrier ——— real wind profile;
 ----- measured wind profile.

$C_n(\bar{v}_1)$ term will be underestimated according to:

$$C_n'(\bar{v}_1) = C_n(\bar{v}_1) + \Delta C_n(\bar{v}_1),$$

where $C_n'(\bar{v}_1)$ is the measured contribution to the normal-force coefficient and $C_n(\bar{v}_1)$ is the real contribution. Besides, if the normal-force coefficient is calculated with different ceiling levels, x_{3R} , of the control volume, the error $\Delta C_n(\bar{v}_1)$, is invariable with the choice of this level. On the other hand, due to mass conservation, the mean vertical velocity at the ceiling height is underestimated with a constant value. Hence, the $C_n(\bar{v}_3)$ term is overestimated according to:

$$C_n'(\bar{v}_3) = C_n(\bar{v}_3) + \Delta C_n(\bar{v}_3),$$

where $C_n'(\bar{v}_3)$ is the measured contribution to the normal-force coefficient and $C_n(\bar{v}_3)$ is the real contribution. Besides, for different ceiling heights, x_{3R} , the error $\Delta C_n(\bar{v}_3)$ is dependent on this height. The higher this level, the greater the error, $\Delta C_n(\bar{v}_3)$, due to the increase in the mean horizontal velocity $\bar{v}_1(x_1, x_{3R})$ at this level. Consequently, the calculated normal-force coefficient increases with the ceiling height of the control volume, which cannot be correct. On the other hand, if the lower part of the measured wind profile at the rear surface of the control volume is taken in reverse (see figure 4.3b), the opposite is found: the calculated normal-force coefficient shows a decrease with increasing ceiling height. A constant normal-force with increasing ceiling level, is only found for a wind profile that ensures mass conservation in the control volume.

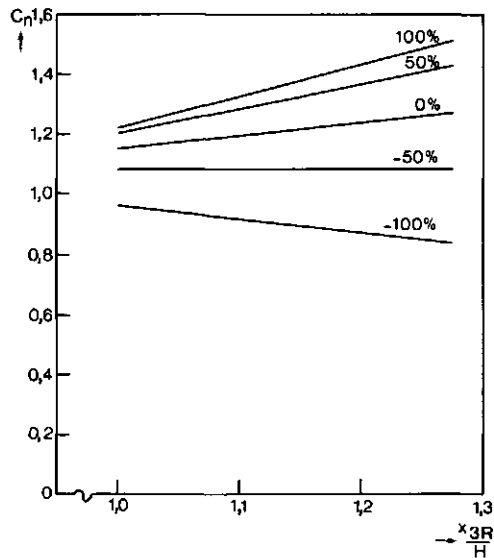


Fig. 4.4 The calculated normal-force coefficient for different ceiling heights of the control volume and for different flow conditions at the rear side of the control volume. E.g. 50% stands for 50% of the measured speed values at the lower rear side of the control volume.

In the calculation of the normal-force coefficient we adopted the following procedure. For different ceiling levels the normal-force coefficient was calculated with speed values between 100% to -100% of the measured values for the lower rear side of the control volume. As the correct normal-force coefficient we accepted the value that did not exhibit a ceiling level dependence, because that ensured that mass was conserved. An example of this procedure is given in figure 4.4 for a mean perpendicular flow direction in near-neutral atmospheric conditions ($\frac{H}{L} = -0,01$). Here a constant normal-force coefficient $C_n = 1,08$ was found for a reversed flow at the lower rear side of the control volume of 50% of the measured speed values. This result

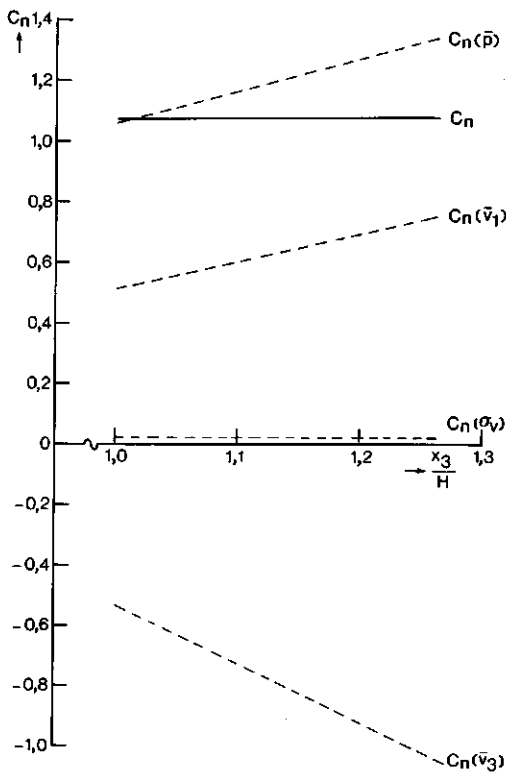


Fig. 4.5 The values of the contributing normal-force coefficient terms for different ceiling levels in a run with perpendicular flow direction $\phi = 0^0$ and $\frac{H}{L} = -0,01$.

was accepted as a correct value. Moreover, this result is in agreement with the direct force method.

For the accepted normal-force coefficient, the numerical values of the different contributing terms are plotted in figure 4.5 as a function of the ceiling level. As can be expected from the choice of the narrow control volume, the pressure term, $C_n(\bar{p})$, is the most important one, followed by the two mean momentum flux terms $C_n(\bar{v}_1)$ and $C_n(\bar{v}_3)$. Moreover it is clearly shown that the turbulence term, $C_n(\sigma_v)$, is of minor importance. For all runs with nearly perpendicular flow direction ($|\phi| \leq 5^\circ$), an almost similar picture was found. In addition, a constant normal-force coefficient was found if the flow at the lower rear side of the control volume was taken reversed with a numerical value of almost 50% of the measured wind speed. The last feature also agreed with the wind vanes and smoke visualization.

4.3.1 Normal-force coefficients in oblique flow direction

The static pressure measurements could only be carried out during the summer season under absolutely dry weather conditions. Rain drops block the ports of the pressure probes and moreover the micro barometer, based on an electric-capacity principle, produces fallacious values. This restriction limited the number of runs in which pressure profiles were measured, needed for the momentum budget calculations. For all runs in which the pressure profiles were measured, only two runs satisfied the near-neutral condition $|\frac{H}{L}| \leq 0,02$. As a consequence, the dependence on the angle of incidence could only be analyzed if we took $|\frac{H}{L}| \leq 0,07$ as the near-neutral condition. This was accepted and the calculated normal-force coefficients for oblique winds have been plotted in figure 4.6 as well as the relation $C_{n0} \cdot \cos^2 \phi$.

If we look only at small incidence angles, we find a mean normal-force coefficient:

$$C_n = 1,09 \quad \text{for } |\phi| \leq 5^\circ,$$

with a standard deviation of 0,05. This result is in good agreement with the direct force method. For the entire angle range, however, we find the relation:

$$C_n = 1,09 \cdot \cos^2 \phi \quad \text{for } |\phi| \leq 26^\circ,$$

with a much larger standard deviation of 0,12.

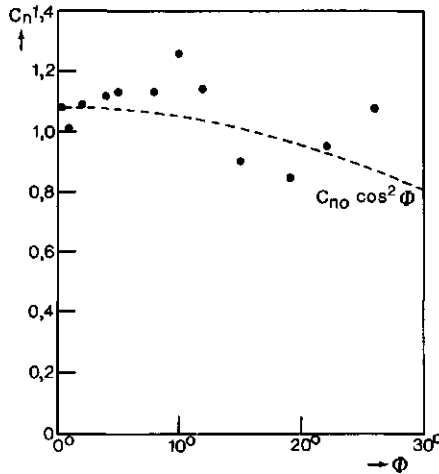


Fig. 4.6 The normal-force coefficient, calculated with a momentum budget method in oblique flow direction and near-neutral stratification ($|H^H| \leq 0,07$).

4.3.2 Normal-force coefficient in stratified atmospheric conditions

In an unstable atmosphere, the undisturbed atmospheric wind profile contains more horizontal momentum below the obstacle height than a wind profile in stable stratified condition. In front of the barrier, an adverse pressure gradient is generated, to deflect the flow upwards. This gradient depends on the amount of air mass below the obstacle height that has to pass the barrier. Therefore, it is reasonable to expect that the normal-force coefficient will increase with instability.

We selected all calculated normal-force coefficients in perpendicular flow direction and plotted them in figure 4.7. The calculation procedure as pointed out in the former sections was applied for all calculations. A linear regres-

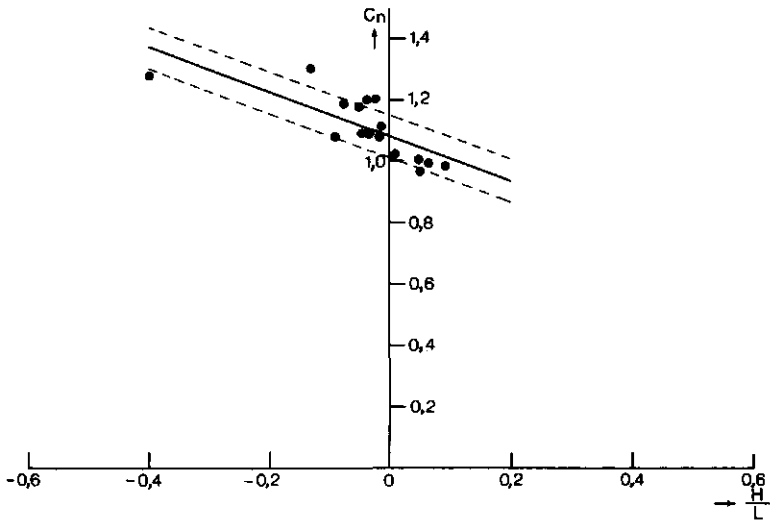


Fig. 4.7 The effect of atmospheric stratification on the normal-force coefficient under perpendicular flow direction $|\phi| \leq 5^\circ$.

sion fitted to the data results in:

$$C_n = 1,08 - 0,72 \frac{H}{L} \text{ for } -0,4 < \frac{H}{L} < 0,1 ,$$

with a standard deviation of 0,06.

In figure 4.8 the regressions of the contributing terms have been plotted as a function of the stability parameter $\frac{H}{L}$. From this picture we conclude that the horizontal momentum flux term, $C_n(\bar{v}_1)$, increases with instability, but that the momentum flux term, $C_n(\bar{v}_3)$, at the ceiling of the control volume decreases at almost the same rate. As a result, the net change of the normal-force coefficient due to the horizontal momentum only slightly increases with instability. The main change of the normal-force coefficient is obviously caused by pressure effects. Figure 4.8 also clearly shows that the turbulence term, $C_n(\sigma_v)$, for the whole stability range, remains constant and is of minor importance.

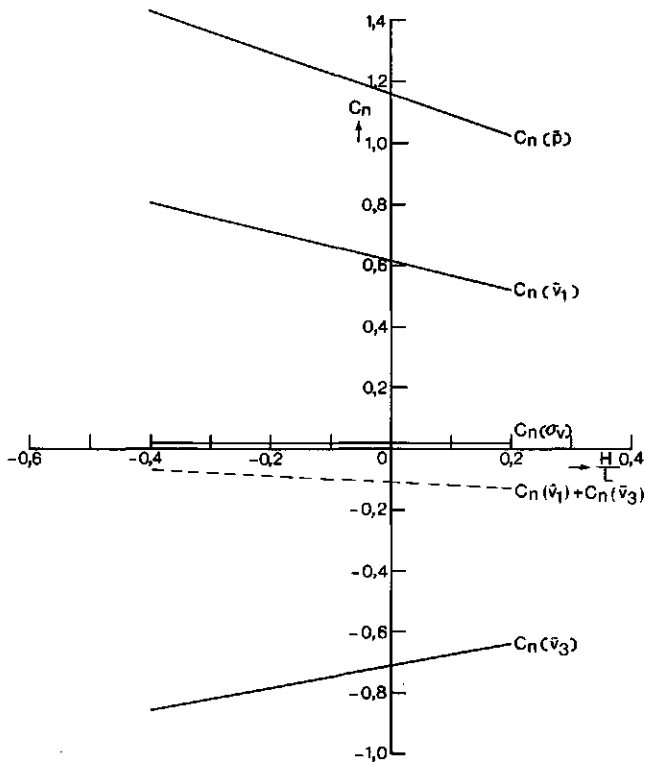


Fig. 4.8 The effect of atmospheric stratification on the discrete contributing terms of the normal-force coefficient in perpendicular flow direction $|\phi| \leq 5^\circ$.

4.4 CONCLUSIONS ABOUT THE NORMAL-FORCE COEFFICIENT

The normal-force coefficient of a closed barrier, which is attached to the surface, has a numerical value of $C_n = 1,07$ in a near-neutral atmosphere and in perpendicular flow direction. This coefficient is independent of the Reynolds number.

In oblique flow directions, the normal-force on a closed barrier depends on the momentum flux perpendicular to the barrier. Consequently, the normal-force coefficient follows a $\cos^2\phi$ dependence. A porous barrier consisting of slats, however, can be considered as a row of independent slats in a first

order approximation. For not too wide angles, the normal-force coefficient of these barriers follows a $\frac{\cos\phi}{4 + \pi\cos\phi}$ dependence.

The normal-force coefficient depends significantly on the thermal stratification. This coefficient increases with increasing instability and decreases with increasing stability.

The momentum budget method, as used in this study, proved to be a correct method to determine the normal-force coefficient. Besides, this method gives insight into the importance of the contributing terms to the normal-force coefficient. For a narrow control volume it proved that the pressure term is the most important term, followed by the horizontal momentum term. The turbulence term, however, is of minor importance.

5 Model calculations

One of the earliest attempts to describe the disturbed shear flow behind a two-dimensional barrier is the diffusive model by Kaiser (1959). In this model, Kaiser started from the assumption that the momentum loss behind an obstacle spreads according to the diffusion equation. The barrier itself is modelled by a sheet sink of momentum.

This model is unrealistic and oversimplified physically. First, Kaiser did not use the momentum equation, which rules the flow. Second, the barrier itself is correctly modelled, however, the rate of change of the momentum flux in the flow, due to the barrier, does not agree with the force on the barrier. Third, the conservation of the angular momentum of the flow does not hold.

We checked this model against our data and found that the model results and the data did not coincide at all. There are other model approaches (Tani, 1958; Sforza et al., 1970 and Garshore, 1972) which are based on similar concepts. However, these models give no significant improvement either.

Because of the weak physical foundation of these models and the bad agreement with experimental evidence, we decided not to analyze these models any further.

5.1 TOWNSEND'S MODEL

5.1.1 Description of the model

A physically more realistic model to describe the disturbed leeward wind field is that by Townsend (1965). Townsend started from a logarithmic wind profile in the undisturbed flow:

$$\bar{u}_0 = \frac{u_*}{\kappa} \ln \frac{x_3}{z_0} \quad (5.1)$$

Townsend introduced two kinds of disturbances: those caused by the wake effect and those caused by the decrease in the surface stress. To describe the disturbed wind profiles, Townsend made the similarity hypothesis:

$$\bar{u} = \bar{u}_0 - \frac{u_1}{\kappa} f_1\left(\frac{x_3}{l}\right) - \frac{u_2}{\kappa} f_2\left(\frac{x_3}{l}\right). \quad (5.2)$$

Here l represents a length scale, u_1 a velocity scale due to the wake effect of the barrier and u_2 a velocity scale determined by the change of the surface stress. These velocity scales only depend on the distance x_1 from the barrier. The functions f_1 and f_2 are universal dependent on the dimensionless height $\frac{x_3}{l}$.

Townsend made a similar hypothesis for the disturbed shear stress. For small velocity disturbances, $|\bar{u}_0 - \bar{u}| \ll \bar{u}_0$, he assumed:

$$\bar{\tau} = \bar{\tau}_0 - 2u_* u_1 F_1\left(\frac{x_3}{l}\right) - 2u_* u_2 F_2\left(\frac{x_3}{l}\right). \quad (5.3)$$

He substituted (5.2) and (5.3) in the streamwise two-dimensional momentum equation. He obtained, after using the continuity equation and after linearization, the result:

$$l \ln \frac{l}{z_0} \left\{ \frac{dv_1}{dx_1} \cdot f_1 - \frac{v_1}{l} \cdot \frac{dl}{dx_1} \cdot \eta \cdot f_1' \right\} = 2 \frac{v_1}{l} F_1', \quad (5.4)$$

where $\eta = \frac{x_3}{l}$, the dimensionless height, and a prime stands for differentiation with respect to η . The self-preservation can be obtained only if there is required:

$$\frac{dl}{dx_1} \ln \frac{l}{z_0} = C_1 \quad \text{and} \quad \frac{1}{v_1} \ln \frac{l}{z_0} \frac{dv_1}{dx_1} = C_2, \quad (5.5)$$

where C_1 and C_2 are constants. Townsend took as these constants:

$$C_1 = C_2 = 2\kappa^2. \quad (5.6)$$

Using the initial condition $l = H$ for $x_1 = 0$, he found for the length scale:

$$l \left(\ln \frac{l}{z_0} - 1 \right) - H \left(\ln \frac{H}{z_0} - 1 \right) = 2\kappa \cdot x_1 \quad (5.7)$$

Using the additional momentum flux due to the barrier:

$$\int_{z_0}^{\infty} (\bar{u}_0^2 - \bar{u}^2) dx_3 = \frac{1}{2} \bar{u}_H^2 \cdot H \cdot C_d, \quad (5.8)$$

where C_d is the drag coefficient, he found for the velocity scales:

$$u_1 = \frac{C_d \cdot H}{4 \cdot I} \cdot u_* \frac{(1n \frac{H}{z_0})^{2+\frac{1}{2I}}}{1(1n \frac{1}{z_0})^{1+\frac{1}{2I}}}, \quad (5.9)$$

$$u_2 = \frac{u_1}{1n \frac{1}{z_0}}, \text{ where } I = \int_0^{\infty} f_2(\eta) d\eta.$$

Substitution of (5.5) in the momentum equation gives:

$$\eta f_1 = F_1. \quad (5.10)$$

To find an explicit solution for the leeward velocity profiles, Townsend used the mixing length hypothesis:

$$F_1 = \eta f_1', \quad (5.11)$$

and he finally arrived at:

$$\eta < 1 : \bar{u} = \bar{u}_0 - \frac{u_1}{\kappa} (e^{-\eta} + \frac{1n \eta}{1n \frac{1}{z_0}}), \quad (5.12)$$

$$\eta \geq 1 : \bar{u} = \bar{u}_0 - \frac{u_1}{\kappa} \cdot e^{-\eta}.$$

Because of the linearization procedure which Townsend applied, this result is only valid sufficiently far downstream from the barrier.

The model of Townsend points out the decisive role of the drag coefficient of the barrier in the disturbed flow field. Here, both velocity scales are linearly dependent on this coefficient. The higher the drag coefficient, the greater these velocity scales and, consequently, the greater the flow reduction will be.

Townsend has checked his model against the data provided by Rider (1952). Rider's data were taken instead of Nægeli's data, probably because first, Rider's reference profile agreed better with the logarithmic form of (5.1) and, second, Rider's farthest station downstream the barrier was at $64 H$ while Nægeli's farthest station was at $30 H$. Rider's experiment was carried out over a rectangular sportsfield. The surface consisted of short grass with a length of about $0,03 \text{ m}$. A hawthorn hedge surrounding the sportsfield was used as a barrier; the grass was on the leeward side. The adjacent windward side was covered with wheat stubble with a mean height of about $0,25 \text{ m}$. In fact in this experiment the turbulent boundary layer was simultaneously subjected to a step change in the surface roughness and to a porous barrier.

Rider's data for $x_1 \geq 9 H$ and for the two levels $0,6 H$ and $1,2 H$ agreed well with the model results after the drag coefficient, C_d , and the obstacle height, H , were adjusted to give optimal agreement with his model calculations. The real C_d value was unknown and the mean obstacle height was $1,7 \text{ m}$. The best fit was obtained for a drag coefficient of $1,8$ and a height of $1,24 \text{ m}$. Townsend argued that for a closed barrier the effective height of the barrier equals the real height H . For a porous barrier, however, the effective height is unknown, but has the same order of magnitude as the real height of the barrier. That is why the optimal fit is found for a smaller porous obstacle height.

5.1.2 Model results

We performed calculations with Townsend's model and compared them with the data presented in section 3.2.1 for a near-neutral atmosphere ($\frac{H}{L} = -0,002$) and perpendicular flow direction ($\phi = -1^\circ$). The measured undisturbed wind profile was fitted with a logarithmic curve, which resulted in a dimensionless friction velocity $\frac{u_*}{u_H} = 0,084$ and a terrain roughness length $z_0 = 0,039 \text{ m}$.

As barrier height was taken 2 m , which corresponds to the real obstacle height. As drag coefficient was taken $1,07$; the numerical value which was obtained by the direct-force method. The model calculations and the data are presented in figure 5.1. Besides, in this figure the back flow in the near wake region ($x_1 < 5 H$) is constructed as observed by the wind vane and smoke vizualizations.

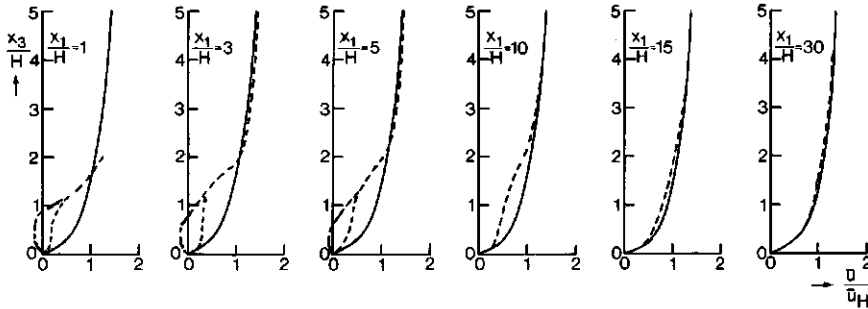


Fig. 5.1 The mean wind speed profiles behind the barrier after Townsend's model in comparison with the measured profiles ——— model calculations; --- measured values by the cup anemometers; —.— values by vane and smoke visualizations.

In the near wake region, the model results do not indicate a back flow near the surface. Here, the velocity disturbances are great, hence, a great discrepancy between the model calculations and the data should be expected. The results of figure 5.1 show this discrepancy clearly indeed.

In the far wake region ($x_1 > 5H$), the velocity disturbances become gradually smaller with increasing distance from the barrier. Hence, a better agreement between the model calculations and the data should be expected with increasing distance from the barrier. At the station $x_1 = 10H$, the model calculations show an overestimation to a height of approximately $3H$. The maximum wind speed difference occurs at about the obstacle height and is circa 40% with respect to the reference speed \bar{u}_H . At greater distances the differences become gradually smaller, with a maximum of about 20% and 10% at the stations $x_1 = 15H$ and $x_1 = 30H$ respectively. The heights at which this maximum occurs has shifted to approximately $2H$ at the latter station. From figure 5.1 we conclude that the model calculations do not coincide with the data of the far wake region except at great height. Here, the differences between the model calculations and the data become gradually smaller with increasing distance from the barrier. If a maximum difference of 10% from the reference speed \bar{u}_H is accepted as reasonable, it means that the model of Townsend is

only correct for distances greater than 30 H downstream a closed barrier.

In the model of Townsend the disturbed flow near the rough surface is assumed to be in "local equilibrium" in the sense that the turbulent energy production locally balances the dissipation and consequently the perturbed shear stress is in equilibrium with the disturbed wind profile (Townsend, 1961). This means that the speed profiles must exhibit a logarithmic part near the surface. If the model calculations of the far wake region are put in a semi-logarithmic plot, this surface layer can easily be recognized (see figure 5.2). From this result it can be seen that this surface layer starts very close to the surface and becomes gradually thicker. It has often been assumed (Bradshaw & Wong, 1972) that the growth rate of the surface layer is nearly the same as that downstream of a small step change in the surface roughness. In the case of a small step change in the surface roughness, the thickness of the logarithmic surface layer is roughly 1% of the downstream distance

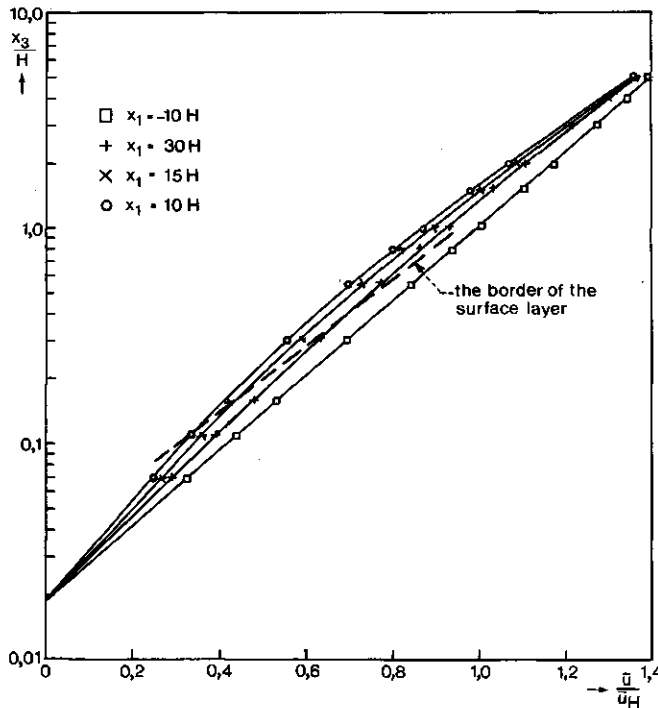


Fig. 5.2 The calculated wind profiles for the far wake region after Townsend's model.

from the surface perturbation (Peterson, 1969). In figure 5.3, the thickness of the logarithmic surface layer according to Townsend's model have been plotted against the downstream distance from the barrier. From this result we see that the thickness of the surface layer according to Townsend's model is roughly 1% of the downstream distance too. Besides, in figure 5.3 the data have been plotted which will be discussed later on in this section.

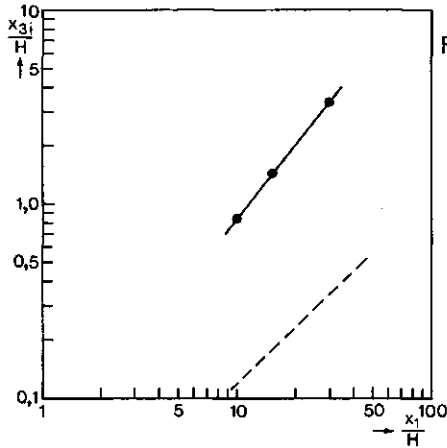


Fig. 5.3 The height of the surface layer
 ——— measured;
 - - - - - Townsend's model.

It is of interest to investigate whether the data do indicate a local equilibrium layer near the surface. That is why in figure 5.4 the data are also given in a semi-logarithmic plot. From this result the logarithmic surface layer can easily be deduced. At the station $x_1 = 10 H$ the local equilibrium layer extends to a level of about $0,8 H$, which is much higher than the model of Townsend predicts. At the station $x_1 = 15 H$, the surface layer gradually extends to a height of $1,4 H$. At the farthest station, $x_1 = 30 H$, the extrapolated logarithmic surface layer extends to a height of approximately $3,5 H$. Here, however, the data exhibit a significant undershoot below the logarithmic extrapolation line; the departures from the logarithmic line are 3%, 6% and 3% for the levels H , $2 H$ and $3 H$ respectively. In figure 5.3 the growth of the measured logarithmic surface layer has been plotted too. From these results it may be concluded that the measured rate of growth is almost the same as the predicted one according to Townsend's model. The thickness of these layers, however, differs almost one order of magnitude.

The occurrence of a logarithmic layer near the surface is of special interest because Bradshaw & Wong (1972) have discussed in detail the nature of this

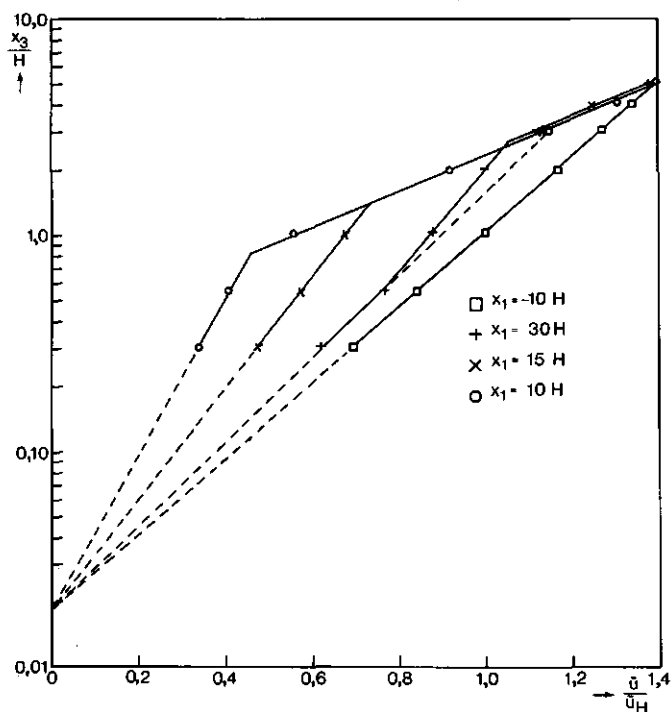


Fig. 5.4 The measures wind profiles for the far wake region in perpendicular flow direction ($\phi = 0^\circ$) and near-neutral stratification ($\frac{H}{L} = 0,001$). ---- logarithmic profile extrapolation.

layer just downstream the reattachment point of a backward-facing step in a wind tunnel experiment along a smooth surface. In their experiments they found a pronounced dip below the line corresponding to the logarithmic "law". At the station 16 step heights downstream the backward-facing step, the undershoot had a maximal departure from the logarithmic line of approximately 5%. The undershoot gradually became smaller and shifted to a higher level with increasing distance.

Bradshaw & Wong proposed two possibilities to explain the undershoot in the logarithmic surface layer: first that there does not exist a local equilibrium; second that the length scales of turbulence near the surface increase more rapidly with the height than in a normal equilibrium layer. On the other hand, Etheridge & Kemp (1978), who studied the flow just around the separa-

tion region due to a backward-facing step in a water channel along a smooth surface, did not find evidence for an undershoot in the logarithmic velocity profile of the surface layer. Their measuring stations were located at the reattachment point, $x_1 = 4,9 H$, and at $x_1 = 6 H$ and $x_1 = 8,29 H$. That they did not find an undershoot in the logarithmic part of the profiles they ascribed to the fact that they measured much closer to the reattachment point than Bradshaw & Wong did. However, from the measured momentum profiles, they found positive evidence that near the reattachment point the length scales of turbulence near the surface increase more rapidly with height than in a normal equilibrium layer. That means that the disturbed flow near a smooth surface is more complex, hence, it is more difficult to be modelled.

The wind profiles for the far wake region presented here (figure 5.4) exhibit an undershoot in the logarithmic part near the surface only at the farthest station. A possible reason for not finding a velocity undershoot at the locations $x_1 = 10 H$ and $x_1 = 15 H$ may be the difference in terrain conditions. The laboratory measurements by Bradshaw & Wong as well as those by Etheridge & Kemp were carried out along a smooth surface, whereas our measurements were performed over rough terrain. A second possible reason may be that the undershoot in the logarithmic part occurs below the lowest measuring level at the stations $x_1 = 10 H$ and $x_1 = 15 H$. Only additional measurements may clarify this.

5.1.3 Conclusions about Townsend's model

In order to describe the disturbed shear flow behind a line obstacle, Townsend has used the streamwise momentum equation. Behind the obstacle, Townsend assumed that the flow in the wake is self-preserving. Near the surface, however, Townsend assumed that the flow is in local equilibrium. Townsend linearized the momentum equation, which means that the solution is only valid sufficiently far downstream the barrier. By using the rate of change of the momentum flux, due to the barrier, Townsend introduced the drag coefficient into the solution. The drag coefficient is a parameter which, in thermally neutral stratification and perpendicular flow direction, is determined by the geometry of the barrier and the terrain roughness only.

In the near wake region ($x_1 \leq 5 H$), the model calculations and the data do not coincide at all. Here, the disturbances are not small and a great discrepancy between the calculations and the data should be expected. Besides, in this region the model does not indicate a back flow near the surface.

In the far wake region ($x_1 > 5 H$), the speed disturbances become smaller and an increasing agreement between the calculations and the data should be expected with increasing distance downstream the barrier. The comparison between the model results and our data shows that the differences become smaller with increasing distance. At the station $x_1 = 10 H$, the maximum wind speed difference occurs at about the obstacle height and is about 40% with respect to the reference wind speed \bar{u}_H . At the farthest location, the maximum speed difference occurs at a level of approximately $2 H$ and is about 10%.

The disturbed wind profiles of the far wake region show a logarithmic part near the surface. The thickness of this logarithmic surface layer is almost one order of magnitude greater than Townsend's model predicts. The rate of growth of this layer, however, corresponds to Townsend's predicted rate of growth.

The logarithmic surface layer, exhibits a significant undershoot at the farthest station only. This can be an indication that the disturbed flow near the surface is more complex than it was expected. Additional measurements are needed to clarify this feature over rough terrain in more detail.

5.2 COUNIHAN, HUNT AND JACKSON'S MODEL

5.2.1 Description of the model

The most sophisticated model that describes the profiles in the far wake region is that by Counihan, Hunt and Jackson (1974). The far wake region is defined as the region beyond the reattachment point. In the following, this model will be referred to as the C.H.J. model. C.H.J. assumed that the undisturbed upstream boundary layer can be described by the power law:

$$\bar{u}_0 = \bar{u}_H \cdot \left(\frac{x_3}{H}\right)^n, \text{ where the exponent, } n, \text{ has to be chosen to obtain the best}$$

fit. Very close to the surface, however, they used the logarithmic profile

$$\bar{u}_0 = \frac{u_*}{\kappa} \ln \frac{x_3}{z_0}$$

In the C.H.J. model, the far wake region is divided into 3 layers: the surface layer W, the mixing layer M and the external layer E. The surface layer W is adjacent to the rough surface, where the flow is assumed to be in local equilibrium. Here the turbulent energy production balances the dissipation and the disturbed wind speed is assumed to obey the law of the wall:

$$\bar{u} = \frac{u_*1}{\kappa} \ln \frac{x_3}{z_0}, \quad (5.13)$$

where u_{*1} is the local friction velocity defined as $\sqrt{\frac{\tau_w1}{\rho}}$.

C.H.J. postulated the existence of a mixing layer, M, in which the velocity perturbation, defined as $u = \bar{u} - \bar{u}_0$ (\bar{u} is the real wind speed and \bar{u}_0 the undisturbed upstream speed), is self-preserving. Here, the motions at different sections differ only in velocity and length scales. For the mixing layer, C.H.J. proposed the following solution for the perturbation term u:

$$u = \bar{u}_H \cdot \left(\frac{H}{x_1}\right)^m \hat{u} \cdot \frac{df}{d\eta}, \quad (5.14)$$

where $\eta = \frac{x_3}{l}$.

Here, m is an arbitrary power. l represents a length scale, which depends on the distance x_1 only. \hat{u} is a constant dimensionless velocity scale, referred to as the "wake strength", which is determined by the characteristics of the barrier and the roughness of the surface. Or, $\hat{u} \cdot \left(\frac{H}{x_1}\right)^m$ is a local velocity scale. The function f is universal, dependent only on the dimensionless height $\eta = \frac{x_3}{l}$.

In the mixing layer, C.H.J. assumed that in a first order approximation the perturbation of the shear stress, $\tau = \bar{\tau} - \bar{\tau}_0$ ($\bar{\tau}$ is the real shear stress and $\bar{\tau}_0$ is the undisturbed upstream shear stress), behaves like that in a turbulent wake and can be expressed by:

$$\tau = 2\rho K_H \frac{\partial u}{\partial x_3}, \quad (5.15)$$

where K_H represents the undisturbed upstream exchange coefficient for momentum at the obstacle height H .

By substitution of the proposed wind speed, $\bar{u} = \bar{u}_0 + u$, and shear stress, $\bar{\tau} = \bar{\tau}_0 + \tau$

in the streamwise two-dimensional momentum equation, C.H.J. obtained, after using the continuity equation, for the momentum equation:

$$-m \cdot \eta^n \cdot f' - \frac{H}{T \cdot H} \cdot \frac{x_1}{dx_1} \cdot \eta^{n+1} f'' + n \cdot \eta^{n-1} \left\{ m \cdot f - \frac{x_1}{H} \cdot \frac{H}{T} \cdot \frac{d}{dx_1} (f - \eta f') \right\} = \frac{2K_H}{\bar{u}_H} \cdot \frac{x_1}{H^2} \cdot \left(\frac{H}{T} \right)^{n+2} f'''' \quad (5.16)$$

The self-preservation can be obtained only if there is required:

$$\frac{2K_H}{\bar{u}_H} \cdot \frac{x_1}{H^2} \cdot \left(\frac{H}{T} \right)^{n+2} = C_3, \quad (5.17)$$

where C_3 is a constant for which C.H.J. took $C_3 = 1$. Hence, for the length scale they found:

$$l = H \cdot \left(\frac{x_1}{R_t \cdot H} \right)^{\frac{1}{n+2}}, \quad (5.18)$$

where R_t is a turbulent Reynolds number, which is defined as:

$$R_t = \frac{\bar{u}_H \cdot H}{2K_H}. \quad (5.19)$$

Substitution of (5.18) in the momentum equation (5.16) gives:

$$(n+2)f'''' + \eta^{n+1} f'' + (m(n+2) - n) \cdot \eta^n f' + n(1-m(n+2)) \eta^{n-1} f = 0 \quad (5.20)$$

The appropriate solution for this differential equation cannot be determined

until m is found. An additional conservation condition for some physical quantity in the wake is needed. Mostly for this condition is used the relation between the change of the momentum flux due to the barrier and the drag on the barrier (see for example (5.8) in Townsend's model). In C.H.J.'s model, however, this condition did not lead to a suitable solution. Instead of this condition they used the conservation of angular momentum. The self-preserving solution of (5.16) can only satisfy this conservation condition if:

$$m = 1, \tag{5.21}$$

$$\text{and } \hat{u} = \frac{-\tilde{C}}{R_t \cdot H^2 \cdot \bar{u}_H \cdot I},$$

$$\text{where } I = (1+n)(2+n) \frac{4+n}{2+n} \frac{\Gamma(4+n) \cdot \Gamma(\frac{1-n}{2+n})}{\Gamma(\frac{2-n}{2+n})},$$

$$-\tilde{C} = \int_0^\infty x_3 \cdot \bar{u}_0 \cdot (u - u_E) dx_3.$$

Here, u_E stands for the solution of the wind speed perturbation in the external layer E.

Finally for the wind speed perturbation, u , in the mixing layer they found

$$u = \bar{u}_H \frac{H}{x_1} \cdot \hat{u} \cdot \frac{d}{d\eta} \left\{ \eta^2 \cdot {}_1F_1 \left(\frac{2-n}{2+n}, \frac{4+n}{2+n}, \frac{-\eta^{n+2}}{(n+2)^2} \right) \right\} \tag{5.22}$$

where ${}_1F_1$ is the confluent hypergeometric function as defined by Abramowitz & Stegun (1964, p 504). In this solution, the "wake strength", \hat{u} , is a constant which is determined by the geometry of the barrier and the roughness of the surface. C.H.J., however, did not find a relation between the "wake strength" and the barrier and surface characteristics. They suggest that the "wake strength", \hat{u} , must be experimentally fitted in such a way that \hat{u} agrees with the maximum value of

$$\left| \frac{\bar{u} - \bar{u}_0}{\bar{u}_H} \cdot \frac{x_1}{H} \cdot \frac{1}{\eta} \right| \text{ in the disturbed flow field of the far wake region.}$$

In the surface layer C.H.J. assumed that the flow is in local equilibrium. Here, the flow obeys the law of the wall (5.13). In this layer C.H.J. intro-

duced a perturbation friction velocity, v_* , defined as:

$$u_{*1} = u_* + v_* , \quad (5.23)$$

where u_{*1} is the real local friction velocity and u_* is the undisturbed friction velocity. Hence, a perturbation velocity, u , can be introduced in this layer which is defined as:

$$u = \frac{v_*}{\kappa} \ln \frac{x_3}{z_0} . \quad (5.24)$$

By matching the perturbation velocity and perturbation shear stress in the surface layer with those of the mixing layer, C.H.J. got the matching conditions:

$$\frac{v_*}{\kappa} \ln \frac{x_{3W}}{z_0} = \bar{u}_H \cdot \frac{H}{x_1} \cdot \bar{u} \cdot f' \left(\frac{x_{3W}}{T} \right), \quad (5.25)$$

$$2 u_* v_* = \frac{2 \cdot \bar{u} \cdot K_H}{T} \cdot \bar{u}_H \cdot \frac{H}{x_1} \cdot f'' \left(\frac{x_{3W}}{T} \right),$$

where x_{3W} stands for the thickness of the surface layer. The solutions of v_* and x_{3W} from (5.25) lead to complicated expressions unless $\frac{x_{3W}}{T}$ is close to the value at which f'' vanishes. C.H.J. did show this and they finally arrived at:

$$u = \bar{u} \cdot \frac{H}{x_1} \cdot \bar{u}_H \cdot f' \left(\frac{x_{3W}}{T} \right) \cdot \frac{\ln \frac{x_3}{z_0}}{\ln \frac{x_{3W}}{z_0}}, \quad (5.26)$$

for the surface layer. It is of interest to note that the shape of this solution is similar to Townsend's surface layer solution (5.12). This is not surprising, since both models in the surface layer are based on the same concepts.

C.H.J. checked their model with wind tunnel data and found an excellent agreement for the far wake region. In addition, they checked their model with the outdoor data of Nægeli (1953). For Nægeli's data, they found a good agreement too, except for Nægeli's farthest station $x_1 = 30 H$. At this station

a systematic underestimation of the wind speed was found. C.H.J. ascribed this underestimation to the finite width of Nägeli's barrier.

5.2.2 Results of the C.H.J. model

We performed calculations with C.H.J.'s model and compared them with our field data for a near-neutral atmosphere ($\frac{H}{L} = 0,002$) and perpendicular flow direction ($\phi = -1^0$). The measured undisturbed wind profile was fitted with the power curve $\bar{u} = \bar{u}_H \cdot (\frac{x_3}{H})^n$, which resulted in $n = 0,24$. In addition, the logarithmic curve (5.1) was fitted, which resulted in a normalized friction velocity $\frac{u_*^*}{\bar{u}_H} = 0,084$ and a terrain roughness length $z_0 = 0,039$ m. For the "wake

strength", \hat{u} , we took the maximum value of $|\frac{\bar{u} - \bar{u}_0}{\bar{u}_H} \cdot \frac{x_1}{H} \cdot \frac{1}{\Gamma}|$ for the far wake

region ($x_1 > 5 H$), which resulted in $\hat{u} = 2,72$. The model calculations and the data have been plotted in figure 5.5 for the far wake region.

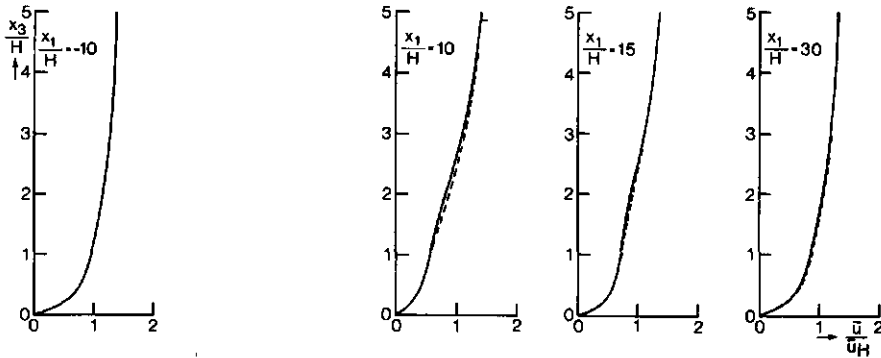


Fig.5.5 The mean wind profiles behind the barrier after the model by Counihan Hunt and Jackson in comparison with the measured profiles. ——— model calculations; --- measured values by the cup anemometers.

From figure 5.5, we conclude that the C.H.J.-model results agree well with our data. At the station $x_1 = 10 H$, the maximum speed difference occurs at a height of about $3 H$ and with a difference of less than 5% from the reference wind speed \bar{u}_H . At greater distances, the differences decrease and are smaller than 3% and 2% at the stations $x_1 = 15 H$ and $x_1 = 30 H$, respectively. Besides,

the maximum difference shifts to a slightly higher level; at the farthest station it occurs at a height of about 2 H.

In the mixing layer, C.H.J.'s model is self-preserving. In order to check the self-preservation, the data of this layer can be plotted on a single curve. Therefore, in figure 5.6, the data,

$\frac{\bar{u}_0 - \bar{u}}{\bar{u}_H} \cdot \frac{x_1}{H}$, have been plotted against $n = \frac{x_3}{H}$ for all runs with an incidence

angle of $|\phi| \leq 1^\circ$ and a thermal stratification of $|\frac{H}{L}| \leq 0,002$.

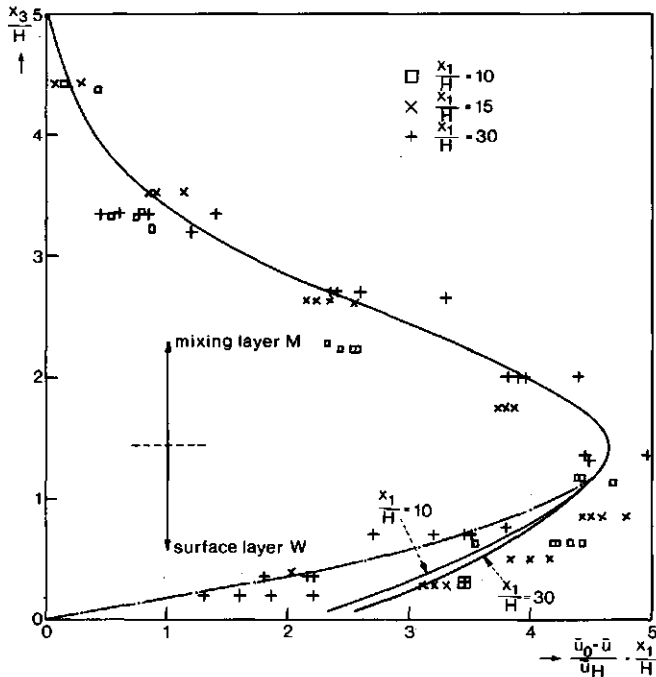


Fig. 5.6 The velocity deficit measurements for all runs with an incidence angle of $|\phi| \leq 1^\circ$ and a thermal stratification of $|\frac{H}{L}| \leq 0,002$, plotted as a self-preserving profile for the far wake region.

— theoretical curve; - - - extrapolated mixing layer curve.

Here all the results are presented in groups for the three different stations. Moreover in this figure, theoretical curves based on C.H.J.'s model are given,

both for the mixing layer M and for the surface layer W. In the mixing layer, our data show a scatter around the theoretical curve without a systematic deviation. The scatter, however, is larger than that found in wind tunnel experiments (e.g. Counihan et al., 1974 and Perera, 1981) but smaller than the scatter in the full-scale experiments of Nägeli (1953) (see e.g. Counihan et al., 1974).

It is interesting to note that in figure 5.6 the results of our last station, $x_1 = 30 H$, do not show a systematic deviation from the theoretical curve either. C.H.J. analyzed the data of Nägeli and found for the farthest station of Nägeli a clear systematic underestimation of the wind speed deficits. The width of Nägeli's barrier was about 11 H and C.H.J. concluded that at this station, the wake ceased to be two-dimensional. In our experiment, the barrier had a width of 30 H. No systematic underestimation in the wind speed deficits being found, it is reasonable to suppose that side influences due to the finite width of the barrier are of minor importance in our experimental results.

In the surface layer W, the normalized wind speed deficits, $\frac{\bar{u}_0 - \bar{u} x_1}{\bar{u}_H \cdot H}$, are not

self-preserving. In figure 5.6 the theoretical solutions have been plotted for the stations $x_1 = 10 H$ and $x_1 = 30 H$. Here we see that the two stations closest to the reattachment point, $x_1 = 10 H$ and $x_1 = 15 H$, show a scatter around the theoretical curves. The farthest station deviates from the theoretical curve systematically. If the theoretical curve from the mixing layer is extrapolated into the surface layer, however, we see that our data of the farthest station are in much better agreement with this curve. In a wind tunnel experiment, performed by Perera (1981) the same was found for the stations beyond the distance 20 H.

In order to compare the surface layer of C.H.J.'s model with the data of this layer in more detail, both results have been given in a semi-logarithmic plot in figure 5.7. Besides, in this figure we have constructed the upper border of this layer for both results. The border of the C.H.J.-model has been taken as the height at which $f''\left(\frac{x_3}{1}\right)$ vanishes and the border of the data has been constructed from figure 5.4. From this result it can be concluded that C.H.J.'s model

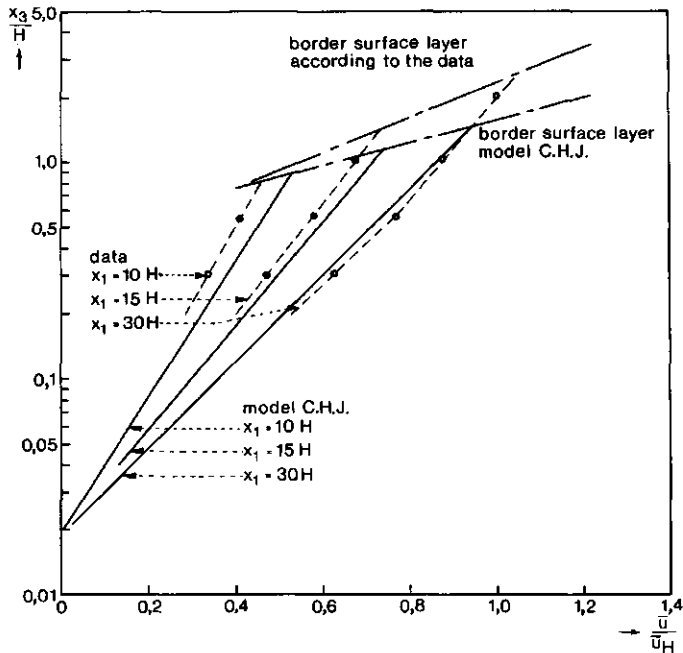


Fig. 5.7 The C.H.J.-model results in comparison with the near-neutral data for the surface layer of the far wake region.

gives a much better description of the surface layer than Townsend's model (see figure 5.2). Moreover, it can be seen that C.H.J.'s model underestimates the thickness of this layer systematically.

In C.H.J.'s model, it is assumed that the normalized local velocity scale decreases with the distance according to (see (5.14)) $\hat{u} \cdot \left(\frac{H}{x_1}\right)^m$. C.H.J. showed that self-preservation requires $m = 1$. That is why C.H.J. supposed that the maximum value of

$\frac{\bar{u}_0 - \bar{u}}{\bar{u}_H}$ in the far wake region has to decrease according to:

$$\left(\frac{\bar{u}_0 - \bar{u}}{\bar{u}_H}\right)_{\max} = C_4 \cdot \left(\frac{H}{x_1}\right)^{m'} \quad (5.27)$$

where C_4 is a constant and m' is close to 1. C.H.J. checked this hypothesis with a large number of available wind tunnel data and with the full-scale experiments of Nägeli (1953) and Rider (1952). As result they found (see Counihan et al., 1974) that these data support the $m' = 1$ hypothesis. Moreover, they found that C_4 lies between 3 and 10, depending on the geometry of the barrier and the surface roughness; C_4 increases with decreasing porosity and decreasing terrain roughness.

For all our near-neutral data ($|\frac{H}{L}| \leq 0,002$, the normalized wind speed deficits have been plotted against $\frac{x_1}{H}$ (figure 5.8). A regression analysis

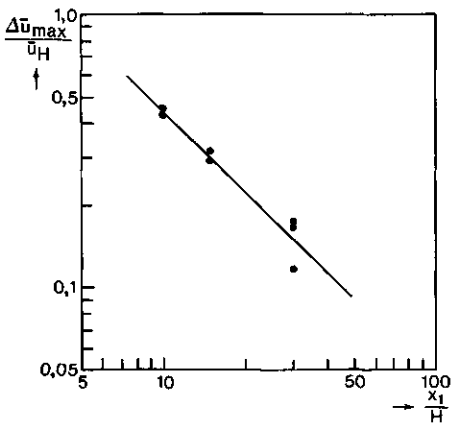


Fig. 5.8 The maximum wind speed deficit for all runs with an incidence angle of $|\phi| < 1^\circ$ and a thermal stratification $|\frac{H}{L}| \leq 0,002$.

was applied to these data and resulted in an exponent $m' = 0,91$ and a constant $C_4 = 4,3$. This is in good agreement with C.H.J.'s hypothesis.

From the results of fig. 5.6, it appears that the maximum wind speed deficits occur at a fixed dimensionless height, about at $\eta_{max} = 1,4$. With the expression for the length scale l (5.18), this means that the vertical displacement of the position of this maximum increases according to:

$$\frac{x_3 \max}{H} = 1,4 \cdot \left(\frac{1}{R_t} \cdot \frac{x_1}{H} \right)^{\frac{1}{n+2}} \tag{5.28}$$

With the exponent $n = 0,24$ and turbulent Reynolds number $R_t = 12$, the theoretical vertical displacement will be:

$$\frac{x_3 \max}{H} = 0,45 \cdot \left(\frac{x_1}{H} \right)^{0,45}$$

From all our near-neutral data ($|\frac{H}{L}| \leq 0,002$), the dimensionless vertical displacement was estimated and plotted (figure 5.9) against the normalized distance $\frac{x_1}{H}$. A regression analysis was applied to these data and resulted in the

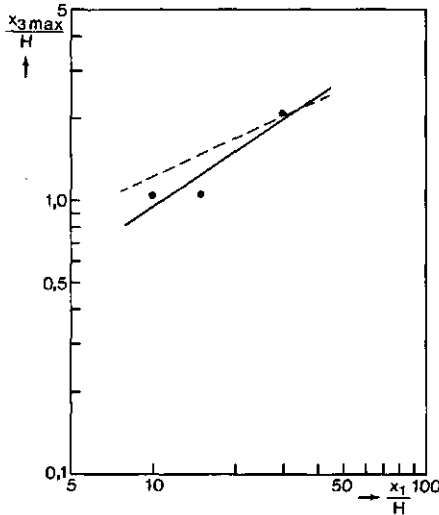


Fig. 5.9 The height at which the maximum speed deficit occurs — experimental curve; --- theoretical curve.

experimental vertical displacement:

$$\frac{x_{3 \max}}{H} = 0,22 \cdot \left(\frac{x_1}{H}\right)^{0,64},$$

which approximately agrees with the theoretical one. Due to the very limited number of measuring levels, the experimental displacement height $x_{3 \max}$, is quite uncertain. The differences between the two displacement results can be ascribed primarily to this uncertainty.

5.2.3 Conclusions about C.H.J.'s model

In order to describe the disturbed shear flow behind a line obstacle, C.H.J. used the streamwise momentum equation. Near the surface, beyond the re-attachment point, C.H.J. assumed the existence of a layer in which the flow is in local equilibrium. Above the surface layer, C.H.J. assumed a mixing layer in which the flow is self-preserving. C.H.J. did not linearize the momentum equation. Consequently, their solution must be valid for a distance much closer to the barrier than Townsend's solution. Our data confirm this. As an additional conservation condition, C.H.J. did not use the relation between the change of the momentum flux, due to the barrier, and the drag on the

barrier, but the conservation of angular momentum. To use C.H.J.'s model in practice, additional measurements are required in order to determine the wake strength \hat{u} . C.H.J. did not find a relation between the drag coefficient, C_d , and the wake strength \hat{u} . The wake strength, \hat{u} , is a parameter which is mainly determined by the geometry of the barrier and the surface roughness.

In the far wake region, ($x_1 > 5 H$), our data agree excellently with the model results. With increasing distance from the barrier, the wind speed differences with respect to the reference wind speed, \bar{u}_H , are less than 5%, 3% and 2% at the stations 10 H, 15 H and 30 H respectively. The maximum speed difference at the station $x_1 = 10 H$ occurs at a height of about H. With increasing distance, the maximum speed difference shifts to a higher level and occurs at a height of about 2 H at the farthest station.

C.H.J. postulated a mixing layer beyond the reattachment point which is self-preserving. Our data do support this hypothesis.

Our data of the farthest station downstream do not deviate systematically from the theoretical single curve in the mixing layer. That is why it is reasonable to suppose that at this station the side influences due to the finite width of the barrier are of minor importance in our experimental results.

In the surface layer, C.H.J.'s model is based on the same concepts as Townsend's model. That is why both models have the same shape in this layer. The data in this layer, however, agree much better with C.H.J.'s model than with Townsend's model. The thickness of this layer is somewhat underestimated by the C.H.J.-model.

C.H.J. postulated that the normalized maximum wind speed deficit,

$$\left(\frac{\bar{u}_0 - \bar{u}}{\bar{u}_H}\right)_{\max}, \text{ decreases according to } \frac{H}{x_1}. \text{ Our data do support this hypothesis.}$$

6 Conclusions and suggestions

The disturbance of the flow field around a closed barrier is asymmetrical. Ahead of the obstacle, a wind speed difference of less than 15% from the reference profile occurs at a distance $-4 H$. Behind the obstacle, a speed difference of less than 15% from the reference profile occurs at the station $30 H$. At a height of $5 H$, the speed disturbances due to the barrier are still perceptible. The greatest speed deviation from the undisturbed speed at this level occurs at a distance of about $4 H$ downstream and is somewhat greater than 5%. The sheltered distance around the barrier, defined as the area near the surface ($x_3 = \frac{H}{3}$) at which the reduction is at least 0,2, extends from $-3 H$ upstream to $24 H$ downstream. In thermally unstable conditions, the mean speed disturbances are greater as the instability increases. The downstream sheltered distance, however, decreases to about $17,5 H$ for $\frac{H}{L} = -0,1$. In stable conditions, the mean speed disturbances are smaller and the recovery of the speed profiles takes place somewhat faster than in the neutral case. The downstream sheltered distance decreases to about $23 H$ and is independent of the stability for $\frac{H}{L} > 0,02$.

A closed barrier causes sheltering for the speed fluctuations too. The downstream sheltered distance for the r.m.s. value of the speed fluctuations, σ_u , is much shorter than the sheltered distance for the mean wind speed. In thermally neutral condition, this distance is about $9 H$. Further downstream, the σ_u values below the barrier height increase gradually and exceed the r.m.s. value of the speed fluctuations at the reference height. The increase is mainly caused by a flux of turbulent kinetic energy from above.

The effect of the atmospheric stratification on the speed fluctuations is much greater than its effect on the mean wind speed. In the unstable case, the downstream sheltered distance for σ_u decreases to $5 H$ for $\frac{H}{L} = -0,09$. Beyond this distance, σ_u below the obstacle height increases rapidly. At a distance $15 H$ downstream the barrier a maximum value of σ_u occurs. At this location, in the $\frac{H}{L} = -0,09$ case, the r.m.s. values of the speed fluctuations at all levels are at least 20% higher than the undisturbed values. In thermally stable conditions, however, the speed fluctuations below the obstacle height are strongly suppressed.

The sheltered distance for the r.m.s. value of the speed fluctuations lies far beyond the station $30 H$ in the thermally stable condition $\frac{H}{L} = 0,09$.

To study the turbulence above the level $x_3 = H$, additional measurements are required. The co-spectra or the auto-correlation functions of the velocity components have to be determined in order to correct the data obtained by the cup anemometers.

In oblique flow directions, the downstream sheltered distance for the mean wind speed follows the cosine dependence for barriers of infinite width:

$$x_{1s} = x_{1s0} \cdot \cos\phi,$$

for incidence angles up to:

$$\phi = \tan^{-1}\left(\frac{2x_{1s0}}{B}\right) - 25^\circ.$$

For wider incidence angles, the apparent sheltered distance, x_{1s}^* , is determined by the width of the barrier and in a first order approximation equals:

$$x_{1s}^* = \frac{B}{2} \tan(\phi + 25^\circ) \cdot \cos\phi.$$

Just in front of a closed barrier, there is a recirculation region starting at a distance of about $-0,5H$ and ending on the barrier at a height of about $0,6 H$. Behind the barrier, there is a second recirculation region starting on the barrier and ending at a distance of about $6 H$. Within these recirculation regions, the speed values, as measured by the cup anemometers, deviate much from the mean velocity. Here, the velocity profiles can only be correctly measured by anemometers that indicate the speed and the direction simultaneously.

The normal-force coefficient, defined as $C_n = \frac{D}{\frac{1}{2}\rho\bar{u}_H^2 H}$, has a numerical value of

$C_n = 1,07$ for a closed obstacle in perpendicular flow direction and in thermally neutral condition. This coefficient is independent of the Reynolds number $Re = \frac{\bar{u}_H \cdot H}{\nu}$. In oblique flow directions, the drag on a closed barrier de-

depends on the momentum flux perpendicular to the barrier. Consequently, the normal-force coefficient must follow a $\cos^2\phi$ dependence. Our data do support this.

The normal-force coefficient is dependent on the thermal stratification. In unstable conditions, this coefficient increases significantly; $C_n = 1,37$ for $\frac{H}{L} = -0,1$. In stable conditions, this coefficient decreases significantly; $C_n = 1,00$ for $\frac{H}{L} = 0,1$.

The momentum budget method, as used in this study to determine the normal-force coefficient in an indirect way, proved to be a correct method. In near-neutral conditions and perpendicular flow direction, this method resulted in a normal-force coefficient of $C_n = 1,09$, which is in good agreement with the direct-force method. In oblique flow directions, however, the standard deviation was 0,12 which is three times the standard deviation of 0,04 obtained by the direct-force method.

We compared the wind profile data with the model by Townsend (1965). Townsend linearized the streamwise momentum equation in his model. In the near wake region ($x_1 \leq 5 H$), the wind speed disturbances are great. Hence, we expected and found a great discrepancy here between the calculations and the data. Besides, in this region Townsend's model does not indicate a back flow near the surface.

In the far wake region ($x_1 > 5 H$), Townsend's model overestimates our data at all stations. The maximum differences with respect to the reference wind speed, \bar{u}_H , are 40%, 20% and 10% at the downstream stations 10 H, 15 H and 30 H respectively. The height at which the maximum difference occurs is about 1 H at the 10 H station and about 2 H at the farthest downstream station 30 H.

Near the surface, Townsend assumed a layer in which the flow is in local equilibrium. Here, the velocity profiles are logarithmic. Our wind speed data show a logarithmic surface layer. The rate of growth of this layer, however, is almost one order of magnitude higher than Townsend's model predicts.

Laboratory experiments, performed by Bradshaw & Wong (1972) in which the dis-

turbed shear flow due to a backward-facing step along a smooth surface was studied, exhibit a significant undershoot in the logarithmic part of all velocity profiles beyond the reattachment point. Bradshaw & Wong proposed two main possible explanations of this feature: first that there does not exist a local equilibrium; second that the length scales of turbulence near the surface increase more rapidly with the height than in a normal equilibrium layer. The latter possibility was confirmed by Etheridge and Kemp (1971), who studied the flow just around the separation region due to a backward-facing step in a water channel. That means that the disturbed flow near a smooth surface is more complex, hence it is more difficult to be modelled. Our data exhibit a velocity undershoot in the logarithmic surface layer at the far station only. Possible causes of our failure to find a velocity undershoot at the stations 10 H and 15 H may be first that we performed our experiment over a natural terrain; second that a velocity undershoot occurred below our lowest measuring level. In future full-scale experiment, more attention must be paid to clarifying this feature for a natural terrain in more detail.

We compared our wind speed data of the far wake region ($x_1 > 5 H$) with the model results of Counihan, Hunt and Jackson (1974) (referred to as the C.H.J. model). C.H.J.'s model results for the self-preserving mixing layer agree excellently with our data. In this layer, the maximum speed differences with respect to the reference wind speed, \bar{u}_H , are less than 5%, 3% and 2% at the stations 10 H, 15 H and 30 H, respectively. The maximum speed difference occur at a level of approximately 1 H at the 10 H station. With increasing distance, the maximum speed difference shifts to a higher level. At our farthest station, 30 H, it has a height of about 2 H.

According to C.H.J.'s model, the mixing layer is self-preserving. That means that the data of this layer can be represented by a single curve. Our data do support this hypothesis.

Our wind speed data for the last station, $x_1 = 30 H$, do not deviate systematically from the single curve in the mixing layer in perpendicular flow direction. Hence, we conclude that the wake remained two-dimensional at our last station in perpendicular flow direction. Besides, this indicates that in our experiment the recovery of the wind profiles by side effects is of

minor importance up to our farthest station.

In the surface layer, C.H.J.'s model results agree well with our data for the stations 10 H and 15 H. The model results for the farthest station, however, deviate systematically from our data in the surface layer. Here it appears that the model results for the mixing layer, extrapolated into the surface layer, are in much better agreement with our data. The same was found by Perera (1981) in a wind tunnel experiment.

The thickness of C.H.J.'s surface layer is somewhat underestimated. It is in much better agreement with our data, however, than the thickness of Townsend's surface layer.

C.H.J. postulated that the normalized maximum wind speed deficit, $\frac{\bar{u}_0 - \bar{u}}{\bar{u}_H}$, decreases according to $\frac{H}{x_1}$. Our data do support this hypothesis.

Appendix A

CORRECTION PROCEDURE FOR THE SPEED FLUCTUATIONS

A cup anemometer placed in a turbulent wind field responds to the absolute wind speed. If the mean horizontal velocity equals \bar{v}_1 and the fluctuating horizontal velocity components are v_1' and v_2' with $|v_1'| < \bar{v}_1$, a good estimate of the mean speed \bar{u} is (Bernstein, 1967):

$$\bar{u} = \sqrt{\bar{v}_1^2 + \overline{|v_2'|^2}} \quad (\text{A.1})$$

The velocity distribution of the v_2' component is Gaussian, hence (A.1) can also be written as:

$$\bar{u} = \bar{v}_1 \sqrt{1 + \frac{2}{\pi} \frac{\overline{v_2'^2}}{\bar{v}_1^2}} \quad (\text{A.2})$$

where $\overline{v_2'^2}$ is the variance of the v_2' distribution.

If the variance of the speed fluctuations is estimated with a cup anemometer, the following relation holds:

$$\overline{(\bar{u} + u')^2} = (\bar{v}_1 + v_1')^2 + \overline{v_2'^2}. \quad (\text{A.3})$$

No correlation exists between v_1' and v_2' , consequently the speed variance, $\overline{u'^2}$, will be:

$$\begin{aligned} \overline{u'^2} &= \overline{v_1'^2} + \left(1 - \frac{2}{\pi}\right) \overline{v_2'^2} \\ &\approx \overline{v_1'^2} + 0,36 \overline{v_2'^2} \end{aligned} \quad (\text{A.4})$$

$\overline{v_2'^2}$ and $\overline{v_1'^2}$ are of the same order, hence a good approximation for (A.4) is:

$$\overline{u'^2} \approx 1,36 \overline{v_1'^2}. \quad (\text{A.5})$$

By the pulse counting system, the pulses were averaged over the 10 s counter gate time intervals. This means that the measured speed variance,

$\overline{u_m'^2}$, will be (Pasquill, 1974; Tennekes, 1981):

$$\begin{aligned} \overline{u_m'^2} &= \frac{2 \overline{u'^2} \Delta t}{\Delta t} \int_0^{\Delta t} \left(1 - \frac{\tau}{\Delta t}\right) \rho_u(\tau) d\tau \\ &\approx \frac{2 \overline{u'^2} \Delta t}{\Delta t} \int_0^{\Delta t} \left(1 - \frac{\tau}{\Delta t}\right) \rho_{v_1}(\tau) d\tau, \end{aligned} \quad (\text{A.6})$$

where $\rho_x(\tau)$ is the correlation function of quantity x .

A simple analytical approximation for a correlation function in a homogeneous atmospheric surface layer is (Bessem, 1976; Tennekes, 1979):

$$\rho_{v_1}(\tau) = \exp(-|\tau| \cdot I_{v_1}^{-1}), \quad (\text{A.7})$$

where I_{v_1} is the integral time scale. This time scale is related to the peak frequency of the normal stress spectrum by (Bessem, 1976):

$$I_{v_1} = \frac{1}{2\pi n_m}, \quad (\text{A.8})$$

where n_m is the peak frequency.

Appendix B

PHASE SHIFT ERROR, CAUSED BY SPATIAL SENSOR SEPARATION

If a cross-correlation is estimated between the two velocity components $v_1'(\bar{x}_0, t)$ and $v_3'(\bar{x}_0 + \vec{r}, t)$, measured at two different locations \bar{x}_0 and $\bar{x}_0 + \vec{r}$, a correlation reduction is introduced dependent on this spatial separation (Kaimal et al., 1968). For an estimation of this reduction, one of these quantities must be translated over this separation distance \vec{r} . If we assume that in a first approximation the turbulence of the flow is frozen, Taylor's hypothesis, $t = \frac{|\vec{r}|}{v_1}$, can be applied and the translated v_3' component can be written as:

$$v_3'(\bar{x}_0 + \vec{r}, t) = v_3'(\bar{x}_0, t - \frac{|\vec{r}|}{v_1}). \quad (B.1)$$

The Fourier transforms V_1 of the v_1' component and V_3^t of the translated v_3' component equal (Bendat and Piersol, 1971):

$$V_1(\bar{x}_0, n) = \int_{-\infty}^{\infty} v_1'(\bar{x}_0, t) e^{-i2\pi n t} dt,$$

$$\begin{aligned} \text{and } V_3^t(\bar{x}_0, n) &= \int_{-\infty}^{\infty} v_3'(\bar{x}_0, t - \frac{|\vec{r}|}{v_1}) e^{-i2\pi n t} dt \\ &= \int_{-\infty}^{\infty} v_3'(\bar{x}_0, t') e^{-i2\pi n (t' - \frac{|\vec{r}|}{v_1})} dt', \\ &= e^{i2\pi n \frac{|\vec{r}|}{v_1}} \cdot V_3(\bar{x}_0, n), \end{aligned} \quad (B.2)$$

$$\text{where } t' = t - \frac{|\vec{r}|}{v_1}$$

Hence the measured one-sided spectrum, expressed in the one-sided spectrum for coinciding sensors, will be:

$$G_{v_1 v_3}^t(\vec{x}_0, n) = v_1^* \cdot v_3^t$$

$$= G_{v_1 v_3}(\vec{x}_0, n) \cdot e^{-i2\pi n \frac{|\vec{r}|}{v_1}}$$

And the measured co-spectrum will be:

$$Co_{v_1 v_3}^t(\vec{x}_0, n) = \text{Re}\{G_{v_1 v_3}^t(\vec{x}_0, n)\}$$

$$= Co_{v_1 v_3} \cdot \cos(2\pi n \frac{|\vec{r}|}{v_1}) + Q_{v_1 v_3} \sin(2\pi n \frac{|\vec{r}|}{v_1}), \quad (B.3)$$

where $Q_{v_1 v_3}$ is the quad-spectrum.

From this result we may infer that the real co-spectrum will be reduced and that a part of the imaginary quad-spectrum will be transformed to the real measured co-spectrum.

The relative error E in the measured momentum flux, caused by spatial separation, will be:

$$E = \frac{v_1^t v_3^t - v_1^t v_3^t}{v_1^t v_3^t}$$

$$= \frac{\int_0^\infty (1-H_c(n)) Co_{v_1 v_3}(n) dn - \int_0^\infty H_s(n) \cdot Q_{v_1 v_3}(n) dn}{\int_0^\infty Co_{v_1 v_3}(n) dn}, \quad (B.4)$$

where $H_c(n) = \cos(2\pi n \frac{|\vec{r}|}{v_1})$ and $H_s(n) = \sin(2\pi n \frac{|\vec{r}|}{v_1})$.

In order to quantify this error, we used the empirical co-spectra relations from the Kansas experiments (Kaimal et al., 1972):

$$-n Co_{v_1 v_3} = \frac{14f}{(1 + 9,6f)^{2,4}} \quad \text{for } f < 1,0, \quad (B.5)$$

$$- \frac{nCo v_1 v_3}{u_*^2} = \frac{11f}{(1 + 13,3f)^{1,75}} \text{ for } f > 1,0 ,$$

and the measured values from Smith (1974) for the quad-spectrum. This error is dependent on the observation height by the nondimensionalized frequency $f = \frac{n \cdot x_3}{v_1}$. The calculated results as a function of this height are depicted in figure B.1.

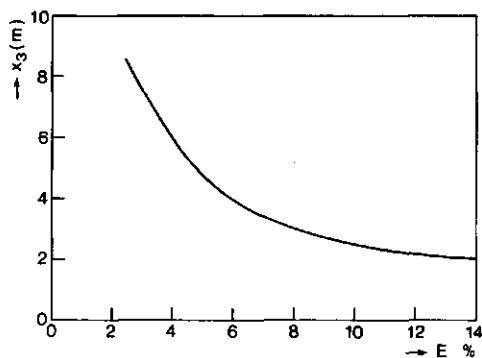


Fig. B.1 The relative error E in the flux of momentum due to spatial separation.

Summary

Shear layer flows which are strongly disturbed, often occur in nature as well as in engineering practice. Up to now little is known about this class of flows. This is partly explained by the complexity of these flows and partly by a lack of experimental data.

The objective of this study is: first, to carry out a full-scale experiment around a two-dimensional barrier which is attached to the earth surface; second, to compare the obtained data with existing models which describe such strongly disturbed shear layer flows.

In Chapter 1, the goal of this study is described in more detail. A review is given of the most important outdoor experiments that were carried out in the past. Besides, in Chapter 1 a qualitative description of these flows is given.

In Chapter 2, more details are given about the measurement program and the terrain conditions.

To ensure that the measured flow disturbances are caused by the erected barrier and are not caused by other terrain disturbances, special attention must be paid to the terrain conditions of the measuring site. The surface condition must be homogeneous and free of other obstacles to an upstream distance of about 100 times the highest measuring level from the most windward location. Such a terrain was found along an aircraft runway, located in the south east of the Netherlands.

In Chapter 3 the data will be discussed. The data of the undisturbed reference location were analyzed and compared with those in the literature. Furthermore, with these data the homogeneity of the windward terrain was analyzed. From these results it appeared that the windward terrain had an overall roughness length of $z_0 = 35$ mm.

The disturbed mean wind field was analyzed in: first, thermally neutral condition and perpendicular flow direction; second, non-neutral conditions and perpendicular flow direction; third, neutral condition and oblique flow di-

rections. From the data obtained in oblique flow directions it appeared that the width of the barrier has an important influence on the sheltering effect near the surface.

The disturbed r.m.s. values of the speed fluctuations are analyzed in order to gain more insight into the turbulence of the distorted flow field. From these results it appeared that the turbulence near the surface is strongly dependent on thermal stratification.

In Chapter 4, special attention is given to the aerodynamic characterization of the barrier. A physically attractive way to characterize an obstacle is to express the effect of an obstacle in terms of its resistance to the fluid flow, or, in dimensionless form, in terms of a drag coefficient. This coefficient was estimated in two different ways. First, by direct force measurements. More or less in the center of the barrier a section was removed and replaced by a measuring plate. The drag on this plate, exerted by the fluid flow was measured with force sensors. Second, by application of momentum conservation to a control volume around the barrier. To use this indirect method, just around the barrier the velocity profiles and the static pressure profiles were measured. Moreover, in Chapter 4 we give an analysis of the influence of thermal stratification and flow direction upon the drag coefficient.

In Chapter 5, the data in near-neutral conditions and perpendicular flow direction are compared with existing models. One of the earliest attempts to describe the disturbed shear flow behind a barrier, is the diffusive model of Kaiser (1959). Because of the weak physical foundation of Kaiser's model and the bad agreement with experimental evidence, we decided not to analyze this model any further in our study.

A physically more realistic model describing the disturbed flow behind a barrier is the self-preserving model of Townsend (1965). The results of this model for the near wake region, i.e. the region between the barrier and the leeward reattachment point, do not coincide at all with our data. Beyond the reattachment point, Townsend's model overestimates the data considerably but with increasing distance from the barrier the differences become gradually smaller.

The most sophisticated model up to now which describes the disturbed flow behind a barrier in the far wake region, is that by Counihan, Hunt and

Jackson (1974). The far wake region is the region beyond the reattachment point. This model (referred to as the C.H.J. model) consists of three layers: first, the surface layer in which the flow is in local equilibrium; second, the mixing layer in which the flow is self-preserving; third, the external layer.

We checked the C.H.J. model against our data and found an excellent agreement.

In Chapter 6, the final conclusions are presented and suggestions are made for future research.

Samenvatting

Grenslaag stromingen die sterk verstoord worden, komen zowel vaak in de natuur voor als in technische toepassingen. Tot nu toe is slechts weinig omtrent deze klasse van stromingen bekend. Gedeeltelijk komt dit omdat deze stromingen erg ingewikkeld zijn maar ook omdat over deze stromingen nog weinig experimentele gegevens bestaan.

Het doel van deze studie is: ten eerste, om een experiment op ware schaal uit te voeren rondom een twee dimensionale schutting op het aardoppervlak; ten tweede, om de verkregen meetresultaten te vergelijken met bestaande modellen die deze sterk verstoorde grenslaagstromingen beschrijven.

In hoofdstuk 1, wordt het doel van deze studie nader uiteengezet. Een overzicht wordt gegeven van de belangrijkste buitenexperimenten die in het verleden zijn uitgevoerd. Ook wordt in hoofdstuk 1 een kwalitatieve beschrijving van deze stromingen gegeven.

In hoofdstuk 2, worden meer bijzonderheden gegeven omtrent het meetprogramma en de terreingesteldheid.

Om er zeker van te zijn dat de verstoringen ten gevolge van de opgestelde schutting worden gemeten en niet die van andere terreinverstoringen, moeten er bijzondere eisen aan het terrein, waarboven deze metingen worden uitgevoerd, worden gesteld. Het oppervlak van dit terrein moet homogeen zijn en moet tot op een afstand van circa 100 maal het hoogste meetniveau stroomopwaarts, vrij zijn van andere obstakels. Zo'n terrein werd aangetroffen langs de startbaan van een vliegveld in het zuid oosten van Nederland.

In hoofdstuk 3 worden de meetresultaten besproken. De metingen van de ongestoorde referentielokatie werden geanalyseerd en vergeleken met die uit de literatuur. Bovendien, werd met deze gegevens de homogeniteit van het bovenwindse terrein geanalyseerd. Uit deze resultaten bleek dat het voorterrein een gemiddelde ruwheidslengte had van $z_0 = 35$ mm.

Het verstoorde windveld werd geanalyseerd onder: ten eerste, thermisch neutrale toestand en loodrechte aanstroomrichting; ten tweede, niet neutrale toestand en loodrechte aanstroomrichting; ten derde, neutrale toestand en bij schuine aanstroomrichting. Uit de meetresultaten die onder schuine aan-

stroomrichting werden verkregen bleek dat de breedte van de schutting een belangrijke invloed heeft op het beschuttingseffect nabij het aardoppervlak. De verstoorde deviaties van de snelheidsfluctuaties werden geanalyseerd om meer inzicht te verkrijgen in de turbulentie van het verstoorde stromingsveld. Uit deze resultaten bleek dat de turbulentie nabij het aardoppervlak sterk afhankelijk is van de thermische gelaagdheid.

In hoofdstuk 4 wordt speciale aandacht besteed aan de aerodynamische karakterisering van de schutting. Een fysische aantrekkelijke manier om een obstakel te karakteriseren is deze uit te drukken in de mate van weerstand die de stroming hiervan ondervindt, of, in dimensieloze vorm, in zijn weerstandscoëfficiënt. Deze coëfficiënt werd op twee verschillende manieren bepaald. Ten eerste, door directe krachtmetingen. Min of meer in het midden van de schutting werd een sectie verwijderd en vervangen door een meetplaat. Aan deze plaat werd de kracht, die het windveld hierop uitoefende, gemeten met behulp van krachtopnemers. Ten tweede, door toepassing van impulsbehoud op een controle volume rondom het obstakel. Om deze indirecte methode te kunnen gebruiken, moeten vlak rondom de schutting de snelheidsprofielen en statische drukprofielen worden bepaald. Bovendien wordt in hoofdstuk 4 het effect van de thermische stabiliteit en de aanstroomrichting op de weerstandscoëfficiënt geanalyseerd.

In hoofdstuk 5 worden de meetgegevens onder neutrale omstandigheid en loodrechte aanstroming vergeleken met bestaande modellen. Een van de eerste modellen die een verstoorde grenslaag achter een schutting beschrijft is het diffusiemodel van Kaiser (1959). Omdat de grondslag van dit model fysisch zwak is en de overeenkomst met experimentele gegevens slecht, besloten we het model van Kaiser niet verder te analyseren.

Een fysisch realistischer model dat de stroming achter een schutting beschrijft is het conformistische model van Townsend (1965). De resultaten van dit model voor het nabije zoggebied, dit is het gebied tussen obstakel en wederaanrakingspunt aan lijzijde, vielen in het geheel niet samen met onze metingen. Voorbij het wederaanrakingspunt overschat het model van Townsend de metingen aanzienlijk, maar met toenemende afstand vanaf het obstakel worden de verschillen geleidelijk aan kleiner.

Het tot nu toe meest geavanceerde model dat de verstoorde stroming achter een schutting beschrijft voor het verre zoggebied is dat van Counihan, Hunt

en Jackson (1974). Het verre zogebied is het gebied voorbij het wederaanrakingspunt. Dit model (aangeduid met het C.H.J.-model) bestaat uit drie lagen: ten eerste, de oppervlakte laag waarin de stroming lokaal in evenwicht is; ten tweede, de menglaag waarin de stroming conformistisch is; ten derde, de externe laag.

Wij hebben het C.H.J.-model getest tegen de meetresultaten en hebben een uitstekende overeenkomst gevonden.

In hoofdstuk 6 worden de uiteindelijke conclusies gegeven en worden aanbevelingen voor toekomstig onderzoek gedaan.

References

- Abramowitz, M., Stegun, I., 1964: Handbook of Mathematical Functions. Washington, Nat. Bur. Stand., 1045 pp.
- Arie, M., Rouse, H., 1956: Experiments on two-dimensional flow over a normal wall. *J. Fluid Mech.* 1.
- Baltaxe, R., 1967: Air flow patterns in the lee of model windbreaks. *Arch. Meteor. Geoph. Biokl. Serie B* 15, (287-312).
- Batchelor, G.K., 1977: An introduction to fluid dynamics. Cambridge University Press, 615 pp.
- Benndorf, D., Grunert, F., Klingbeil, K., 1980: Aero-Dynamische Grundlagen für Windschutzpflanzungen. *Zeitschrift für Meteor.* 30, 6, (369-378).
- Berger, S.A., 1971: Laminar Wakes. Am. Elsevier Publ. Co. Inc. New York 295 pp.
- Bessem, J.M., 1976: Averaging times for turbulent quantities in the stationary and horizontal homogeneous atmospheric boundary layer. Heat transfer and turbulent buoyant convection. E.D. Spalding, D.B., Afgan, N., Hemisphere Publ. Co. Series in Thermal and Fluids Engineering. Vol. 1.
- Bendat, S.B., Piersol, A.G., 1971: Random Data: Analysis and measurement procedures. Wiley-Interscience, New-York 407 pp.
- Bernstein, A.B., 1967: A note on the use of cup anemometers in wind profile experiments. *J. Appl. Meteor.* 6, (280-286).
- Bradshaw, P., Wong, F.Y.F., 1972: The reattachment and relaxation of a turbulent shear flow. *J. Fluid Mech.* 52, (113-135).
- Burnham, J., 1967: A note on the turbulence problem with take-off and landing. R.A.E. Techn. Report No 67240.
- Businger, J.A., Wyngaard, J.C., Izumi, Y., Bradley, E.F., 1971: Flux-profile relationship in the atmospheric surface layer. *J. Atmos. Sci.* 28 (181-189).
- Chang, P.K., 1970: Separation of flow. Pergamon Press 777 pp.
- Counihan, J., Hunt, J.R.C., Jackson, P.S., 1974: Wakes behind two-dimensional surface obstacles in turbulent boundary layers. *J. Fluid Mech.* 52, (529-563).
- Covey, W., 1963: A method for the computation of logarithmic wind profile parameters and their standard errors. The Energy Budget at the Earth Surface. Part 2, U.S. Dep. Agr. Prep. (28-33).

- De Bray, D.B., 1971: Protection by fences, wind effects on buildings and structures. Seminar 25-27 May, University of Auckland N.Z.
- Dyer, A.L., 1974: A review of Flux-profile relationships. *Bound.-Layer Meteor.* 7, (363-372).
- Elliott, J.A., 1972: Instrumentation for measuring static pressure fluctuations within the atmospheric boundary layer. *Bound.-Layer Meteor.* 2, (476-495).
- Etheridge, D.W., Kemp, P.H., 1978: Measurements of turbulent flow downstream of a rearward-facing step. *J.Fluid Mech.* 88, (545-566).
- Fage, A., Johansen, F.C., 1927: On the flow of air behind an inclined flat plate of infinite span. *Proc.Roy.Soc.of London*, 116, (170-197).
- Frost, W., Fichtl, G., Connel, J.R., Hutto, M.L., 1977: Mean horizontal wind profiles measured in the atmospheric boundary layer about a simulated block building. *Bound.-Layer Meteor.* 11 (135-145).
- Gandemer, J., 1981: The aerodynamic characteristics of windbreaks, resulting in empirical design rules. *J.Indust.Aerodynamics* 7, (15-36).
- Gartshore, I.S., 1972: The interaction between turbulent wakes and boundary layer flows. *Can.Aero.Space Inst.Trans.* 5, 49.
- Golder, D., 1972: Relations among stability parameters in the surface layer. *Boundary-Layer Met.* 3, (47-58).
- Good, M.C., Joubert, P.N., 1968: The form drag of two-dimensional bluff-plates immersed in turbulent boundary layers. *J.Fluid Mech.* 31 (547-582).
- Gorshenin, N.M., 1946: Principles on planting forest shelterbelts on arable slopes. *Naucnyi Otcet Uniaime*.
- Grace, J., 1977: *Plant response to wind*. Academic Press, London 204 pp.
- Hagen, L.J., Skidmore, E.L., 1971: Turbulent velocity fluctuations and vertical flow as affected by wind break porosity. *Trans.Asae* (634-637).
- Halitsky, J., 1961: Wind turbulence in the lee of a line of trees. *Verbank Experiments, H.Dickson Farm*.
- Hoerner, S.F., 1956: *Resistance a l'avancement dans les fluides*. Gauthiers-Villars, Paris, 472 pp.
- Hunt, J.C.R., 1971: A theory for the laminar wake of a two-dimensional body in a boundary layer. *J.Fluid Mech.* 49, (159-178).
- Jacobs, A.F.G., 1983A: *Statische drukopener*. Intern Rapport Vakgroep Natuur- en Weerkunde, Agricultural University Wageningen.
- Jacobs, A.F.G., 1983B: *A mechanical low pass filter*. Intern Report Vakgroep Natuur- en Weerkunde, Agricultural University Wageningen.

- Jensen, M.J., 1958: The model-law for Phenomena in natural wind, Ingeniøren-International Edition 2, Denmark.
- Kaimal, J.C., Businger, J.A., 1963: A continuous wave sonic anemometer-thermometer. *J.Appl.Meteor.* 2, (156-164).
- Kaimal, J.C., Wyngaard, J.C., Haugen, D.A., 1968: Deriving power spectra from a three-component sonic anemometer. *J.Appl.Meteor.* 7, (827-837).
- Kaimal, J.C., Wyngaard, J.C., Izumi, Y., Cote, O.R., 1972: Spectral characteristics of surface-layer turbulence. *Quart.J.Roy.Met.Soc.* 98, (563-589).
- Kaiser, H., 1959: Die Strömung an Windschutzstreifen. *Berichte Deutscher Wetterd.* 7, No. 53.
- Kansas 1968 Field Program Data Report, Air Force System Command, United States Air Force. Ed. Izumi, Y.
- Kempen, G.T., 1982: Weerstandcoefficient van een lijnvormig obstakel in de atmosferische grenslaag. M.Sc.Thesis, Agr.University Wageningen.
- Kirchhoff, G., 1869: *J.Reine Angew.Math.* 70, (289-299).
- Konstantinov, A.R., 1966: Evaporation in nature. Israel Program Sci. Translations Jerusalem, 523 pp.
- Lawrence, E.N., 1955: Effects of a windbreak on the speed and direction of wind. *Meteor.Magaz.* 89, (287-292).
- McBean, G.A., 1972: Instrumental requirements for eddy correlation measurements. *J.Appl.Meteor.* 11, (1078-1084).
- Monin, A.S., Obukhov, A.M., 1954: Basic turbulent mixing laws in the atmospheric surface layer. *Trudy Geofiz.Inst. An SSSR* 24, (163-187).
- Monin, A.S., Yaglom, A.M., 1973: *Statistical fluid mechanics.* M.I.T. Press Cambridge Mass. 769 pp.
- Naegeli, I.W., 1941: Untersuchungen über die Windverhältnisse im Bereich von Windschutzstreifen. *Mitt.Schweiz.Anst.Forstl.Versuchsw.* 23, (221-276).
- Naegeli, W., 1953: Untersuchungen über die Windverhältnisse in Bereich von Schilfrohrwänden. *Mitteil.Schweiz.Anst.Forstl.Versuchsw.* 29, No.2.
- Obukhov, A.M., 1941: Energy distribution in the spectrum of a turbulent flow. *Izvestija an SSSR* 4-5, (453-466).
- Obukhov, A.M., 1946: Turbulence in thermally inhomogeneous atmosphere, *An-SSSR* 1, (95-115).
- Obukhov, A.M., 1971: Turbulence in an atmosphere with a non-uniform temperature. *Bound.-Layer Meteor.* 2, (7-29).
- Ogawa, Y., Diosy, P.G., 1980: Surface roughness and thermal stratification

- effects on the flow behind a two-dimensional fence. *Atmospheric Environment* 14, (1301-1320).
- Panofski, P.A., Tennekes, H., Lenschow, D.H., Wyngaard, J.C., 1977: The characteristics of turbulent velocity components in the surface layer under convective conditions. *Bound.-Layer Meteor.* 11, (355-361).
- Pasquill, F., 1974: *Atmospheric diffusion*. Ellis Horwood, Chichester 400 pp.
- Perera, M.D.A.E.S., 1981: Shelter behind two-dimensional solid and porous fences. *J. Indust. Aerodynamics*, 8, (93-104).
- Peterson, E.W., 1969: Modification of mean flow and turbulent energy by a change of surface roughness under conditions of neutral stability. *Quart. J. Roy. Met. Soc.* 95, (561-575).
- Plate, E.J., 1964: The drag on a smooth flat plate with a fence immersed in its turbulent boundary layer, ASME Paper no. 64-FE-17.
- Plate, E.J., 1971: The aerodynamics of shelterbelts. *Agr. Meteor.* 8, (203-222).
- Raine, J.K., Stevenson, D.C., 1977: Wind protection on a simulated atmospheric boundary layer. *J. Industrial Aerodyn.* 2, (159-180).
- Rayleigh, 1876: On the resistance of fluids, *Phil. Mag.* (5), 2, (430-447).
- Raymont, R., Readings, C.J., 1971: The importance of instrumental tilt on measurements of atmospheric turbulence. *Quart. J. Roy. Met. Soc.* 97, (124-130).
- Rider, N.E., 1952: The effect of a hedge on the flow of air. *Quart. J. Roy. Met. Soc.* 78, (97-101).
- Robinson, S.M., 1962: Computing wind profile parameters. *J. Atmos. Sci.* 19, (189-190).
- Seginer, I., Sagi, R., 1971: Drag on windbreak in two-dimensional flow. *Agr. Meteor.* 9, (323-333).
- Seginer, I., 1972: Windbreak drag calculated from the horizontal velocity field. *Bound.-Layer Meteor.* 2, (87-97).
- Seginer, I., 1975: Atmospheric stability effect on wind break shelter and drag. *Bound.-Layer Meteor.* 8, (383-400).
- Sforza, P.M., Mons, R.F., 1970: Wall Wake; Flow behind a leading edge obstacle. *A.I.A.A.I.*, 8, (2162-2167).
- Shaw, S.R.H.S., 1962: Studies on wind protection. Institute for Biological Field Research. *Mededelingen* No. 60/1962.
- Silverman, B., 1968: The effect of spatial averaging on spectrum estimation. *J. Appl. Meteor.* 7, (168-172).

- Smedman, A., Högström, U., 1972: The mastra micro-meteorological field project. Bound.-Layer Meteor. 5, (529-273).
- Smith, S.D., 1974: Eddy flux measurements over lake Ontario. Bound.-Layer Meteor. 6, (235-255).
- Tani, N., 1958: On the wind tunnel test of the model of shelter hedge (in Japanese with English summary), Bull.Nat.Inst.Agric.Sct. A No. 6, 146 pp.
- Tennekes, H., 1979: The exponential langrangian correlation function and turbulent diffusion in the inertial subrange. Atmos.Envir. 13, (1565-1567).
- Tennekes, H., Lumley, J.L., 1972: A first course in turbulence. M.I.T. Press, Cambridge Mass. 300 pp.
- Tennekes, H., 1982: Atmospheric turbulence and air pollution modelling. Ed. Nieuwstadt, F.T.M. and Van Dop, H., D.Reidel Publ.Co. 358 pp.
- Townsend, A.A., 1961: The behaviour of a turbulent boundary layer near separation. J. Fluid Mech. 11, (536-554).
- Townsend, A.A., 1965: Self-preserving flow inside a turbulent boundary Layer. J.Fluid Mech. 22, (773-797).
- Wieringa, J., 1980: A revaluation of the Kansas mast influences on measurements of stress and cup anemometers overspeeding. Bound.-Layer Meteor. 18, (411-430).
- Windbreak and Shelterbelts. W.M.O. Technical Note No. 59, 188 pp.
- Woodruff, N.P., Zings, A.W., 1955: A comparative analysis of wind tunnel and atmospheric air-flow patterns about single and successive barriers. Trans.Am.Geoph.Union 36, (203-208).
- Wyngaard, J.C., Tennekes, H., Lumley, J.L., Margolis, D.P., 1968: Structure of turbulence in a curved mixing layer. Physics of Fluids 11, no. 6 (1251-1253).
- Wyngaard, J.C., Cote, O.R., Izumy, Y., 1971: Local free convection, similarity and budgets of shear stress and heat flux. J.Atmos.Sci. 28, (1171-1182).

Curriculum vitae

Adrianus Franciscus Gerardus werd op 20 januari 1943 geboren te Roermond. Doorliep achtereenvolgens ULO en UTS, waarna het HTS-diploma, richting Elektrotechniek, te Eindhoven werd behaald in 1965. Hierna volgde de militaire dienst bij de verbindingstroepen van de Koninklijke Landmacht te Naarden. Tijdens militaire dienst, in 1967, werd begonnen met een studie aan de Technische Hogeschool, afdeling Technische Natuurkunde, te Eindhoven. Deze werd afgesloten in 1971 bij de groep Stromingsleer (prof.dr.ir. G.Vossers) met het afstudeeronderwerp "Ionisatieverschijnselen achter een gereflecteerde schokgolf" (mentoren ir. L.C.B. Hutten Mansfeld en ir. M.E.J. van Dongen). Tevens werd de onderwijsbevoegdheid in de wis- en natuurkunde behaald. Hierna trad hij in dienst van de N.V. Heidemij Beheer, afdeling Speurwerk, met als taak onderzoek aan transporten van impuls, warmte en materie in lucht en bodem. In 1979 volgde een aanstelling als wetenschappelijk medewerker bij de Landbouwhogeschool te Wageningen, vakgroep Natuur- en Weerkunde. Binnen het taakgebied van de sectie Meteorologie wordt bijgedragen aan onderwijs en onderzoek.